

---


Electronic Theses and Dissertations, 2004-2019

---

2014

## Characterization of Dynamic Structures Using Parametric and Non-parametric System Identification Methods

Ayad Al Rumaithi  
*University of Central Florida*

 Part of the [Civil Engineering Commons](#), [Geotechnical Engineering Commons](#), and the [Structural Engineering Commons](#)

Find similar works at: <https://stars.library.ucf.edu/etd>

University of Central Florida Libraries <http://library.ucf.edu>

This Masters Thesis (Open Access) is brought to you for free and open access by STARS. It has been accepted for inclusion in Electronic Theses and Dissertations, 2004-2019 by an authorized administrator of STARS. For more information, please contact [STARS@ucf.edu](mailto:STARS@ucf.edu).

---

### STARS Citation

Al Rumaithi, Ayad, "Characterization of Dynamic Structures Using Parametric and Non-parametric System Identification Methods" (2014). *Electronic Theses and Dissertations, 2004-2019*. 1325.

<https://stars.library.ucf.edu/etd/1325>

CHARACTERIZATION OF DYNAMICS STRUCTURES USING  
PARAMETRIC AND NON-PARAMETRIC SYSTEM IDENTIFICATION METHODS

by

AYAD AL-RUMAITHI  
B.S. University of Baghdad, 2010

A thesis submitted in partial fulfillment of the requirements  
for the degree of Master of Science  
in the Department of Civil and Environmental Engineering  
in the College of Engineering and Computer Science  
at the University of Central Florida  
Orlando, Florida

Summer Term  
2014

Major Professor: Hae-Bum Yun

©2014 Ayad Al-Rumaithi

## ABSTRACT

The effects of soil-foundation-structure (SFS) interaction and extreme loading on structural behaviors are important issues in structural dynamics. System identification is an important technique to characterize linear and nonlinear dynamic structures. The identification methods are usually classified into the parametric and non-parametric approaches based on how to model dynamic systems. The objective of this study is to characterize the dynamic behaviors of two realistic civil engineering structures in SFS configuration and subjected to impact loading by comparing different parametric and non-parametric identification results.

First, SFS building models were studied to investigate the effects of the foundation types on the structural behaviors under seismic excitation. Three foundation types were tested including the fixed, pile and box foundations on a hydraulic shake table, and the dynamic responses of the SFS systems were measured with the instrumented sensing devices.

Parametric modal analysis methods, including NExT-ERA, DSSI, and SSI, were studied as linear identification methods whose governing equations were modeled based on linear equations of motion. NExT-ERA, DSSI, and SSI were used to analyze earthquake-induced damage effects on the global behavior of the superstructures for different foundation types. MRFM was also studied to characterize the nonlinear behavior of the superstructure during the seismic events. MRFM is a nonlinear non-parametric identification method which has advantages to characterized local nonlinear behaviors using the interstory stiffness and damping phase diagrams.

The major findings from the SFS study are:

- The investigated modal analysis methods identified the linearized version of the model behavior. The change of global structural behavior induced by the seismic damage could be quantified through the modal parameter identification. The foundation types also affected the identification results due to different SFS interactions. The identification accuracy was reduced as the nonlinear effects due to damage increased.
- MRFM could characterize the nonlinear behavior of the interstory restoring forces. The localized damage could be quantified by measuring dissipated energy of each floor. The most severe damage in the superstructure was observed with the fixed foundation.

Second, the responses of a full-scale suspension bridge in a ship-bridge collision accident were analyzed to characterize the dynamic properties of the bridge. Three parametric and non-parametric identification methods, NExT-ERA, PCA and ICA were used to process the bridge response data to evaluate the performance of mode decomposition of these methods for traffic, no-traffic, and collision loading conditions. The PCA and ICA identification results were compared with those of NExT-ERA method for different excitation, response types, system damping and sensor spatial resolution.

The major findings from the ship-bridge collision study include

- PCA was able to characterize the mode shapes and modal coordinates for velocity and displacement responses. The results using the acceleration were less accurate. The inter-channel correlation and sensor spatial resolution had significant effects on the mode decomposition accuracy.

- ICA showed the lowest performance in this mode decomposition study. It was observed that the excitation type and system characteristics significantly affected the ICA accuracy.

Dedicated to  
Family and friends

## ACKNOWLEDGMENTS

I would like to thank my advisor Dr. Hae-Bum Yun for his support and advices in the preparation of this thesis. Without him, this thesis could never been done. He assisted me in every part in my thesis and I am grateful for allowing me to work in his research group.

I would also like to thank Dr. Necati Catbas and Dr. Kevin Mackie for being my thesis committee members. I would like to thank all the coauthors of the journal articles in chapters 2, 3 and 4. The journal article: “System Identification of 12-Story Building Models on Different Foundations: Global Damage Quantification Using Linear Methods” is pending for submission and authored by: Ayad Al-Rumaithi, Dr. Yoonhwak Kim, Dr. Peizhen Li, Dr. Ki Tae Park, Dr. Sami F. Masri, and Dr. Hae-Bum Yun. The journal article: “Quantification of Localized Earthquake Damage Effects on Large-Scale Soil-Foundation Superstructure Systems Using Nonlinear Identification Methods” was accepted for publication in the Journal of Earthquake Engineering and authored by: Bryan Paul, Ayad Al-Rumaithi, Dr. Peizhen Li, Dr. Ki Tae Park, Dr. Sami F. Masri, and Dr. Hae-Bum Yun. The journal article: “A comparative Study of Mode Decomposition Using NExT-ERA, PCA and ICA for Different Excitations” was submitted Journal of Engineering Mechanics. The authors are Ayad Al-Rumaithi, Dr. Hae-Bum Yun, and Dr. Sami Masri. I would also like to thank HCED program for sponsoring me and Dr. Alaa Alwan and Prof. Saad Sarsam for their sponsorship.



## TABLE OF CONTENTS

LIST OF FIGURES .....	xiii
LIST OF TABLES.....	xix
CHAPTER 1: INTRODUCTION.....	1
1.1 Motivation.....	1
1.2 Objectives of the Study.....	3
1.3 Approaches .....	3
1.4 Contribution of the Study.....	5
1.5 Scope.....	6
CHAPTER 2: SYSTEM IDENTIFICATION OF 12-STORY BUILDING MODELS ON DIFFERENT FOUNDATIONS: GLOBAL DAMAGE QUANTIFICATION USING LINEAR METHODS .....	7
2.1 Abstract.....	7
2.2 Introduction.....	7
2.3 Large-Scale Shake Table Tests.....	10
2.4 Time-Domain Modal Analysis Methods .....	14
2.4.1 Deterministic Stochastic Subspace Identification (DSSI) .....	14
2.4.2 Stochastic Subspace Identification (SSI).....	17

2.4.3 Eigen Realization Algorithm with Natural Excitation Technique (NExT-ERA) .....	18
2.5 Modal Analysis Results .....	22
2.6 Discussion .....	30
2.6.1 Quantification of Identification Errors.....	31
2.6.2 Effects of System Nonlinearity .....	34
2.6.3 Effects of Foundation Type .....	38
2.6.4 Effects of Modal Analysis Methods .....	41
2.7 Conclusion .....	43
2.8 Acknowledgement .....	45
2.9 References.....	46
CHAPTER 3: QUANTIFICATION OF LOCALIZED EARTHQUAKE DAMAGE EFFECTS ON LARGE-SCALE SOIL-FOUNDATION-SUPERSTRUCTURE SYSTEMS USING NONLINEAR IDENTIFICATION METHOD.....	50
3.1 Abstract.....	50
3.2 Introduction.....	50
3.3 Large-Scale Shake Table Tests.....	52
3.3.1 Test Setup.....	52
3.3.2 Test Protocol .....	56

3.4 Nonlinear Identification for Chain-like Systems .....	58
3.4.1 MDOF Restoring Force Method.....	58
3.4.2 Determination of Nonlinear Interstory Restoring Forces .....	62
3.4.3 Surface Fitting for Scattered Data in 3-D Restoring Force Phase Domain .....	66
3.4.4 Term-wise Identification Using MRFM .....	69
3.5 Quantification of Localized Interstory Damage .....	73
3.5.1 Visual Inspection of Damage in the Soil-Foundation-Superstructure Systems .....	74
3.5.2 Local Damage Quantification Using Nonlinear MRFM Identification	78
3.5.3 Nonlinear Effects on Mode Shape Identification.....	82
3.6 Conclusions.....	86
3.7 Acknowledgement .....	89
3.8 References.....	89
 CHAPTER 4: A COMPARATIVE STUDY OF MODE DECOMPOSITION USING NEXT-ERA, PCA AND ICA FOR DIFFERENT EXCITATIONS .....	
4.1 Abstract.....	93
4.2 Nomenclatures: .....	93
4.3 Introduction.....	94

4.4 Mode Decomposition Techniques .....	100
4.4.1 Eigen Realization Algorithm with Natural Excitation Technique (NExT-ERA) .....	100
4.4.2 Principal Component Analysis (PCA) .....	102
4.4.3 Independent Component Analysis (ICA).....	103
4.4.4 Mode Shapes and Modal Coordinates for Mode Decomposition Performance .....	105
4.5 Simulation Study.....	106
4.5.1 Model Description .....	106
4.5.2 Analysis Results of the Simulation Data .....	111
4.5.3 Discussion on the Simulation Analysis Results.....	113
4.6 Field Study Using a Full-Scale Suspension Bridge .....	125
4.6.1 Measurements of Bridge Responses in Ship-Bridge Collision Accident .....	125
4.6.2 Analysis Results of the Experimental Data .....	128
4.6.3 Discussion on the Experiment Analysis Results.....	131
4.7 Conclusions.....	134
4.8 Acknowledgements.....	135
4.9 References.....	136

CHAPTER 5: CONCLUSIONS ..... 142

## LIST OF FIGURES

Figure 2.1: Large-scale reinforced cast-in-place concrete frame models placed on three different foundation types tested on a shake table, and the accelerometer locations installed on the shake table and the superstructures (A0 to A7). The measurement direction for all accelerometers used in this study is in x-direction.....	11
Figure 2.2: Comparison of the mode shapes of the superstructures with the fixed, pile and box foundations, identified using DSSI, SSI and NExT-ERA.....	30
Figure 2.3: A comparison between the measured and identified system output for different excitation levels. The system output is for the acceleration on the 12-th floor (A7) of the superstructure with the fixed foundation. ....	32
Figure 2.4: DSSI errors for the superstructure with the fixed foundation at different excitation levels. ....	34
Figure 2.5: Comparison of the identified and measured restoring-force phase diagrams for the superstructure with the fixed foundation subject to different excitation levels. The identified phase diagram was calculated using DSSI.....	36
Figure 2.6: Measured restoring-force phase diagrams for the superstructure with the fixed foundation (solid line). The linear stiffness was estimated using the least square regression of the identified restoring-force phase diagrams with the first-order polynomial (dashed line).....	37
Figure 2.7: Change of the linear interstory stiffness for different excitation levels. ....	38

Figure 2.8: Change of the modal parameters using DSSI for different foundation types.....	39
Figure 2.9: The energies of the acceleration at the shaker (A0) and the superstructure base (A1) for different foundation types. The energy was calculated by measuring the area of the power spectral density of acceleration at the sensors A0 and A1. ....	40
Figure 2.10: Change of identified modal parameters for the superstructure with the fixed foundation for DSSI, SSI and NExT-ERA.....	42
Figure 2.11: Stabilization diagrams of NExT-ERA for the superstructure with the fixed foundation.....	43
Figure 3.1: Large-scale reinforced cast-in-place concrete frame models placed on three different foundation types tested on a shake table, and the accelerometer locations installed on the shake table and the superstructures (A0 to A7). The measurement direction for all accelerometers is in x-direction.....	53
Figure 3.2: A photo of the large-scale soil-foundation-superstructure test setup (note that the size of the experimental setup is compared with the size of a test operator). [6-8].....	55
Figure 3.3: Shake table motions of the acceleration, velocity and displacement time histories for the Shanghai artificial wave at Level 6.....	58
Figure 3.4: A schematic of a multi-degree-of-freedom chain-like system with nonlinear restoring forces. ....	61

Figure 3.5: Measured and identified *time histories of the interstory mass-normalized restoring force ( $Gkm$ )* for the fixed foundation subjected to the Shanghai artificial earthquake excitation at Level 6. The restoring forces are shown from the top story..... 63

Figure 3.6: Measured and identified *interstory phase plots of the displacement ( $xk$ ) and the mass-normalized restoring force ( $Gkm$ )* for the fixed foundation subjected to the Shanghai artificial wave excitation at Level 6. The measured data are shown in the solid line, and the identified data are shown in the dashed line. The phase plots are shown from the top story..... 65

Figure 3.7: Measured and identified *interstory phase plots of the velocity ( $xk$ ) and the mass-normalized restoring force ( $Gkm$ )* for the fixed foundation subjected to the Shanghai artificial earthquake excitation at Level 6. The measured data are shown in the solid line, and the identified data are shown in the dashed line. The phase plots are shown from the top floor..... 66

Figure 3.8: Three-dimensional interstory restoring phase surfaces fitted using the Radial Bases Functions for the superstructure with the fixed foundation subjected to the Shanghai artificial earthquake excitation at Level 6. The normalized displacement and velocity with the range over  $[-1\ 1]$  are shown in x- and y-axis, respectively, and the mass-normalized restoring force is shown in z-axis. .... 69

Figure 3.9: Identified Chebyshev coefficients for the superstructure with the fixed foundation subjected to the Shanghai artificial excitation at Level 6..... 70



Figure 3.10: Power-series coefficients converted from the Chebyshev coefficients in Figure 9 for the superstructure with the fixed foundation subjected to the Shanghai artificial excitation at Level 6. ....	71
Figure 3.11: Term-wise identification results for the mass-normalized interstory restoring force, $G3m$ (Floors 5 and 6), of the superstructure with the fixed foundation subjected to the Shanghai artificial excitation at Level 6: (a)-(c) for the Chebyshev power-series coefficients; (d)-(f) for the power-series coefficients. The measured data are shown in the solid line, and the term-wise identified data are shown in the dashed line.....	73
Figure 3.12: Layout of the pile foundation and cracks on the piles visually inspected after the shaker tests.....	77
Figure 3.13: Dissipated energies associated with structural damage in the superstructure with fixed, pile and box foundations at different excitation levels of the Shanghai artificial waves. ....	79
Figure 3.14: The energies of the acceleration at the shaker (A0) and the ground (A1) for different foundation types. The accelerometer locations are shown in Figure 3.1. ...	81
Figure 3.15: Identified power-series coefficients of (a) the linear stiffness, $a10m$ , (b) cubic stiffness, $a30m$ , and (c) linear damping, $a01m$ , at different excitation levels of the Shanghai artificial waves. ....	82
Figure 3.16: Comparison of (a)-(f) the mode shapes determined with the localized stiffness and damping constants using the MRFM; and (g)-(l) the mode shapes determined with the global stiffness and damping matrices using the Deterministic Stochastic Subspace Identification (DSSI).....	86

Figure 4.1: Study overview for the performance evaluation of the mode decomposition using NExT-ERA, PCA and ICA.....	96
Figure 4.2: Comparison between PCA and ICA components for the bivariate uniform random variables.....	105
Figure 4.3: Procedures of NExT-ERA, PCA and ICA.....	106
Figure 4.4: Mode shapes of the simulation model.....	108
Figure 4.5: The dynamic response of the simulation model at the 10th floor. ...	110
Figure 4.6: Mode shapes and modal coordinates of mode 2 for ACC5-TRU and ACC5-ERA.....	112
Figure 4.7: Comparison of MAC and COR between the identified and true mode shapes and modal coordinates of the first three modes.....	116
Figure 4.8: The mode components of the true, NExT-ERA, PCA and ICA. The angles are shown in radian.....	118
Figure 4.9: The joint probability density functions of the two acceleration sequences of the damped and undamped 2-DOF oscillator.....	122
Figure 4.10: A comparison of true and ICA mode components for different excitation types using the acceleration data. The angles of the true modal components are $\theta_{1TRU} = 1.02$ , and $\theta_{2TRU} = 2.59$ . .....	123
Figure 4.11: The ship-bridge collision by the onboard crane of the cargo ship [26]. .....	126
Figure 4.12: The sensor locations and directions on the bridge [26].....	127

Figure 4.13: The preprocessing procedures to obtain the acceleration, velocity and displacement data of the bridge responses.....	128
Figure 4.14: Bridge responses during the ship-bridge collision after the preprocessing. ....	128
Figure 4.15: Mode shapes identified using NExT-ERA, PCA and ICA methods for the velocity data. The natural frequencies identified by NExT-ERA are 0.170 Hz for mode 1, 0.233 Hz for mode 2, and 0.539 for mode 3. ....	130
Figure 4.16: Modal coordinates identified using NExT-ERA, PCA and ICA methods for the velocity data. The natural frequencies identified by NExT-ERA are 0.170 Hz for mode 1, 0.233 Hz for mode 2, and 0.539 for mode 3.....	131
Figure 4.17: Comparison of MAC and COR between PCA and NExT-ERA, and between ICA and NExT-ERA for different response types.....	133

## LIST OF TABLES

Table 2.1: Properties and dimensions of the superstructure, foundation and soil of the tested building models. ....	12
Table 2.2: Seismic test protocols for fixed, box, and pile foundation models.....	13
Table 2.3: Comparison of different modal analysis methods. ....	23
Table 2.4: Comparison of identified modal frequencies of the superstructure models with fixed, box, and pile foundations. Modal frequency is shown in Hertz (Hz).....	26
Table 2.5: Comparison of identified damping ratios of the superstructure models with fixed, box, and pile foundations. Damping ratio is in percentage (%). ....	28
Table 3.1: Properties and dimensions of the superstructure, foundation and soil of the tested building models. ....	54
Table 3.2: Test protocols with different earthquake excitation waves for the building models with the fixed, pile and box foundations. EL: El Centro wave, SH: Shanghai artificial wave, KB: Kobe wave, and GW: Gaussian white wave. ....	57
Table 4.1: The modal frequencies and damping ratios of the simulation models. ....	108
Table 4.2: Control parameters evaluated in the simulation study.....	111
Table 4.3: Averaged MAC and COR for the first three modes of the acceleration data.....	124
Table 4.4: Identified modal frequencies (Hz) using NExT-ERA. ....	129
Table 4.5: Identified damping ratio (%) using NExT-ERA.....	129

Table 4.6: The averaged distances of the PCA and ICA methods and their ranking in Figure 4.14 for the first five modes. ....	134
---	-----

# CHAPTER 1: INTRODUCTION

## 1.1 Motivation

System identification is an important engineering topic to characterize and assess structural conditions of a vibrating system. For civil engineering structures, building foundation has significant effects on the dynamic behaviors of the superstructure since it governs the boundary conditions of the soil-foundation-structure (SFS) system. In addition, the development of effective identification methods for building or bridge structures in extreme loading events, such as seismic or impact forces, is necessary for structural condition assessment to improve operation safety and structural resiliency against the structurally hazardous events.

Mode decomposition techniques are commonly employed to identify a multi-degree-of-freedom (MDOF) system. Parametric and non-parametric methods are two identification approaches to decompose the structural modes of dynamic structures under different excitation conditions.

The experimental modal analysis is classified into the parametric mode decomposition technique. The modal analysis can be further categorized into input-output modal identification and output-only modal identification, depending on the availability of the excitation measurement in forced vibration applications. Since measuring the forces of MDOF systems is technically difficult and often expensive, the output-only modal identification method is commonly used when the force measurement is not available, but usually with an assumption that the excitation input is a zero-mean Gaussian white noise. There are two main groups of the output-only modal identification method: frequency-

domain and time-domain methods. The time-domain methods include the Eigensystem Realization Algorithm (ERA), Stochastic Subspace Identification (SSI), Ibrahim Time Domain (ITD) method, and the frequency-domain methods include Frequency Domain Decomposition (FDD). These parametric methods identify physically meaningful parameters of the system, which consequently have the interpretation of the identification results be straightforward. However, they require prior information on the system characteristics, and the identification accuracy reduces when the assumption becomes invalid due to unpredictable structural damages.

On the other hand, the Blind Source Separation (BSS) is often used as the non-parametric mode decomposition method. The Principal Component Analysis (PCA) and Independent Component Analysis (ICA) may be two most studied methods among the non-parametric BSS approaches. The MDOF Restoring Force Method (MRFM) is another type of the non-parametric approach for the identification of nonlinear structural behavior. The mathematical models of these techniques are not based on certain physical assumptions (e.g., the equation of motion) but data-driven. Therefore, the non-parametric methods do not require a priori knowledge of the system. The identification process is relatively simple and straightforward since the vibration modes can be determined from the columns of the transformation matrix that can be determined based on underlying statistics of the response data. However, the relationship of decomposed modes to true modes is rather indirect; consequently the interpretation of the non-parametric identification results is not straightforward.

## **1.2 Objectives of the Study**

The objective of this study is to relate the parametric and non-parametric modes using response-only data collected from building and bridge structures subjected to extreme loads. Ten-floor concrete building models placed on different foundation types will be used to investigate the effects of structural damage on seismic behavior of the SFS systems. A full-scale suspension bridge will be used to understand the effects of different load types in a ship-bridge collision accident. Detailed goals to achieve the above research objective include

- To identify the dynamic behavior of the building and bridge structures by applying different parametric and non-parametric identification methods.
- To investigate the effect of different SFS conditions and damage severity on linear and non-linear identification results of the building models.
- To compare the mode decomposition results of the suspension bridge response using the parametric modal analysis and the non-parametric BSS methods.

## **1.3 Approaches**

Two types of structures are involved in this study. First, three identical building frame models with fixed, pile and box foundations were subjected to a series of shake table seismic excitations. The loading amplitudes were increased until severe damage occurs. The soil-foundation-structure interaction affected the amount of seismic energy fed to the



superstructure, which led to different damage patterns for different foundation types. The response was recorded using accelerometers. The superstructures were identified using modal analysis methods. These methods are the deterministic stochastic subspace identification (DSSI), stochastic subspace identification (SSI), and Eigen realization algorithm with natural excitation technique (NExT-ERA). The change in modal parameters with the excitation amplitude and foundation type was examined. The non-linear damage effect on identification error was investigated.

Multi-degree of freedom restoring force method (MRFM), a non-linear localized identification method was used to give better understanding of the structures. The non-linear behavior was characterized from the interstory restoring forces. The measurement of the dissipated energy from the hysteresis loops used to quantify and localize the structural damage.

Second, The Vincent Thomas Bridge (VTB), a bridge located in San Pedro, California in U.S.A. is an 1850-m long cable suspension bridge. The main span length is 457 m. The bridge was collided by a cargo ship in august 2006. This led to a horizontal vibration in the bridge. For damage inspection purposes, the traffic was stopped after 30 minutes from the accident. Since a web-based monitoring system was installed in the bridge in 2005. The ship collision incident was monitored. The bridge response was measured using 26 accelerometers. In this study, the bridge dynamic behavior was studied before, during and after the collision accident. The blind source separation methods, Principal Component Analysis (PCA) and Independent Component Analysis (ICA) methods were used for the modal decomposition of the response. NExT-ERA, The modal

analysis method was also used. The analysis results from acceleration, velocity and displacement responses using different methods were compared.

#### **1.4 Contribution of the Study**

This thesis presents a comprehensive comparative study to relate the parametric and non-parametric mode decomposition techniques for the building and bridge structures. The relationship of the parametric and non-parametric modes validated with the realistic physical systems has been rarely studied.

For the building models, first the complicated SFS systems are identified using different parametric and non-parametric identification methods for different foundation types as the structures are structurally damaged in shake table tests. The modal parameters identified different modal analysis methods, including DSSI, SSI and NEXt-ERA were compared for different levels of damage severity. Then the results are compared with MRFM to relate the non-parametric identification results to the parametric ones. The comparative study shows the advantages and limitations of those identification methods, which are important in the applications of structural condition assessment in earthquakes for different foundation types.

For the bridge models, the parametric and non-parametric modes are identified using NEXt-ERA, PCA and ICA. Previous studies related to this topic were conducted for a limited number of parameters that affect the performance of mode decomposition. This paper presents a comprehensive parametric study for response types, excitation types, system damping, and sensor spatial resolution. Most of the studies were conducted only

using simulation models or small-scale models in laboratory, and the response data obtained from full-scale field structures were relatively rarely studied. The experimental study includes analysis results for the impulse vibration, ambient vibration with traffic, and ambient vibration without traffic, which are unique datasets to investigate the performance of the mode decomposition for different excitation types.

### **1.5 Scope**

The thesis is outlined as follows: The analysis of building models using modal analysis methods in Chapter 2; Analysis of building models using MRFM method in Chapter 3; Mode decomposition of suspension bridge using NExT-ERA, PCA and ICA in Chapter 4; and finally the conclusions in Chapter 5.

## **CHAPTER 2: SYSTEM IDENTIFICATION OF 12-STORY BUILDING MODELS ON DIFFERENT FOUNDATIONS: GLOBAL DAMAGE QUANTIFICATION USING LINEAR METHODS**

### **2.1 Abstract**

This paper presents the effects of nonlinear damage and soil-structure interaction on the modal parameter realization using linear system identification methods. Large-scale 12-story reinforced concrete frames with fixed, pile and box foundations embedded in soil were tested on a high-capacity hydraulic shaker driven with the increasing peak accelerations of seismic ground motions until the structures failed. Three modal analysis methods, including NExT-ERA, SSI and DSSI, were employed to identify the superstructure's dynamic characteristics with the readings of the accelerometers installed on the superstructure. It was observed discrepancy between the measured and estimated dynamic response with (linear assumptions) increased when the superstructure damage was severe. The effects of nonlinearity, damage, and foundation types on modal parameter realization were compared for the different modal analysis techniques.

### **2.2 Introduction**

Experimental modal analysis techniques have been widely used in structural health monitoring to characterize structural damage in dynamic structures. The damage can be quantified by determining a change in the modal parameters of identified structures. A numerous studies have been conducted to investigate the effects of structural damage on identified modal frequencies. One of the earliest works can be found in Cawley and Adams

[1]. They found that modal frequencies decreased as damage increased due to the reduction of structural stiffness. Farrar et al. showed that modal frequency could be used as a damage indicator with less identification error than the other modal parameters, such as damping ratios and mode shapes [2]. However, the modal frequency can be affected by different environmental factors. Studies have been conducted to investigate the effects of environmental conditions on modal frequencies. Wahab and De Roeck studied the effects of temperature on the modal parameters of a highway bridge [3]. They found that identified modal frequencies were highly affected with temperature change. Due to the uncertainty induced by environmental change, Salawu suggested the change of modal frequencies by 5 % or higher could be considered to be confident with the existence of structural damage [4]. Many studies, including Salane and Baldwin [5], and Farrar [6], showed that the damping ratio is a less reliable indicator than natural frequency for damage detection. Mode shapes can be used to localize damage. West suggested a systematic way to localize the damage using the mode shape using modal assurance criterion (MAC) [7]. Damage localization, however, could be difficult due to the insensitivity of mode shapes, particularly in a lower mode.

Experimental modal analysis techniques are usually based on *linear assumption* of underlying dynamic systems. Therefore, when nonlinear system behaviors increase, the identification results could be inaccurate. Although structural damage usually involves nonlinear system behaviors, the effects of structural damage on identification errors have been rarely studied.

The effects of foundation on the dynamic behavior of superstructures have been studied by many researchers. In the 1970s, important analytical and numerical studies were conducted on soil-structure interactions. For example, Bielak [8] and Veletsos et al. [9] studied the dynamic behaviors of structures with embedded foundations. Bielak [10] investigated the nonlinear dynamic behaviors of building-foundations systems. Numerous large-scale shake table tests have been conducted to understand foundation-superstructure interactions under seismic loading, including pile foundations [11] and shallow foundations [12]. A survey paper on structure-soil interaction can be found in Lou et al. [13]. Experimental system identification methods have been used to identify soil-foundation-superstructure (SFS) systems. Shang et al. [14] used modal analysis methods to determine the dynamic characteristics of the SFS system with a box foundation.

Although many precedent studies have unveiled important knowledge of SFS systems, very few large-scale experimental studies have been done to compare the effects of different foundations on the dynamic characteristics of the identical superstructures subject to increasing seismic loadings until the system failure. In this paper, a study was conducted using acceleration datasets obtained from shake table tests conducted at Tongji University, Shanghai, China. Three 1:10-scale, 12-story reinforced concrete frames with fixed, pile and box foundations embedded in soil were tested on a high-capacity hydraulic shaker driven by seismic ground motions with increasing peak accelerations until the systems failed. The objective of this study is to understand foundation effects on identified modal parameters of the superstructure by comparing the three different foundation types as the SFS systems were gradually damaged. Three widely used modal analysis techniques

are employed in this study, including the Eigensystem Realization Algorithm with the Natural Excitation Technique (NExT-ERA), the Stochastic Subsystem Identification (SSI), and the Deterministic Stochastic Subspace Identification (DSSI). Since these modal analysis techniques are global identification techniques based on the assumption of linear dynamic characteristics of superstructures, identification error may increase as nonlinear effects of structural damage in the SFS system increase during the tests.

The paper is outlined as follows: the large-scale experimental studies of the SFS systems are described in Section 2.3; mathematical background of the three modal analysis techniques used in this study is presented in Section 2.4; the results of experimental modal analysis results are shown in Section 2.5; effects of system nonlinearity, foundation types and identification methods are discussed in Section 2.6; and finally the conclusion is followed in Section 2.7.

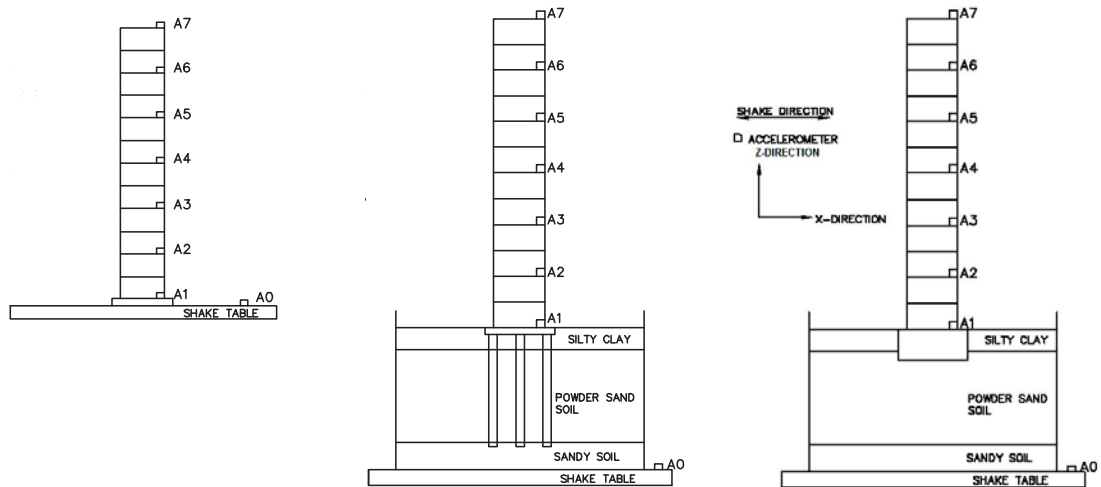
### **2.3 Large-Scale Shake Table Tests**

To experimentally study the effects of soil-foundation interaction on identification results of superstructure's dynamic characteristics, three identical 1:10 scale 12-story cast-in-place concrete frames were fabricated in the State Key Laboratory at Tongji University, Shanghai, China [15], [16], [17].

These frame models were placed on three different types of foundation: fixed, pile and box foundations (see Figure 2.1). The building models with the pile and box foundations were placed on three layers of soil with silty clay, powder sand soil and sandy soil. The layered soil was contained in a flexible cylindrical container to reduce the “box-

effect” of the soil container. The diameter of the container was 3000 mm, and the rubber membrane thickness was 5mm. The rubber membrane was reinforced with steel rings around the rubber membrane to allow the soil’s shear deformation in x-direction.

Then, the soil-foundation-superstructure (SFS) models with the pile and box foundations were placed on a large-scale shake table (see Figures 2.1b and 2.1c). The 4.0 m × 4.0 m shake table has the maximum capacity of 25 tons and can be operated at the maximum acceleration of 1.2g in x-direction. The base plate of the soil container was rigidly bolted to the shake table. The fixed foundation model was not placed on the soil container and was directly bolted to the shake table (see Figure 2.1a). Dimensions and material properties of the superstructures, foundations and soil of the SFS systems are summarized in Table 2.1.



(a) Fixed

(b) Pile

(c) Box

Figure 2.1: Large-scale reinforced cast-in-place concrete frame models placed on three different foundation types tested on a shake table, and the accelerometer locations installed on the shake table and the superstructures (A0 to A7). The measurement direction for all accelerometers used in this study is in x-direction.



Table 2.1: Properties and dimensions of the superstructure, foundation and soil of the tested building models.

Superstructures	Pile foundation	Box foundation	Soil
<ul style="list-style-type: none"> <li>• Model scale: 1:10</li> <li>• Floor number: 12</li> <li>• Floor height: 300 mm</li> <li>• Total height: 3600 mm</li> <li>• Column net spacing: 600 mm × 600 mm</li> <li>• Beam cross-section: 30 mm × 60 mm</li> <li>• Column cross-section: 50 mm × 60 mm</li> <li>• Floor slab thickness: 12 mm</li> </ul>	<ul style="list-style-type: none"> <li>• Pile number: 9</li> <li>• Pile length: 1200 mm</li> <li>• Pile cross-section: 45 mm × 45 mm</li> </ul>	<ul style="list-style-type: none"> <li>• Box size: 650 mm × 650 mm</li> </ul>	<ul style="list-style-type: none"> <li>• Soil layer type: silty clay, powder sand soil, sandy soil</li> <li>• Total soil height: 1600 mm</li> </ul>

A series of shake table tests was conducted for three different earthquake types with seven different excitation magnitude levels for the building models with three foundation types. Four types of excitation were tested including El Centro earthquake (EL), Kobe earthquake (KB), Shanghai artificial wave (SH), and Gaussian white wave (GW). Seven levels of excitation were used in x-direction or xz-directions with the shaker's peak acceleration from 0.093 G to 0.532 G (or Levels 1 to 7) for EL, KB and SH. The control tests were conducted using GW for the shaker's peak acceleration of 0.07 G for all cases (i.e., 1GW, 10GW, 16GW, 22GW, 28GW, 34GW and 40GW) before and after tests at each excitation level of EL, KB and SH. The above test protocols are summarized in Table 2.2.

As shown in the table, the level of excitation increased from low peak acceleration to high peak acceleration gradually for each foundation type. Therefore, damage in the superstructure, foundation and soil were accumulated as the experiments for each foundation type were being conducted. It should be noted that Tests 35–40 could not be

conducted for the fixed foundation due to the superstructure failure during the tests, while all 40 tests were conducted for the pile and box foundations. The effects of the accumulated damage in the SFS systems will be quantified and discussed in Section 2.5.

Table 2.2: Seismic test protocols for fixed, box, and pile foundation models.

Test No.	Excitation Type	Peak Acc. (G)		Test No.	Excitation Type	Peak Acc. (G)	
		X	Z			X	Z
1	1GW	0.07	-	22	22GW	0.07	-
2, 3, 4	EL1, SH1, KB1	0.093	-	23, 24, 25	EL5, SH5, KB5	0.665	-
5, 6, 7	EL2, SH2, KB2	0.266	-	26, 27	ELZ5, KBZ5	0.665	0.53
8, 9	ELZ2, KBZ2	0.266	0.266	28	28GW	0.07	-
10	10GW	0.07	-	29, 30, 31	EL6, SH6, KB6	0.798	-
11, 12, 13	EL3, SH3, KB3	0.399	-	32, 33	ELZ6, KBZ6	0.798	0.53
14, 15	ELZ3, KBZ3	0.399	0.399	34	34GW	0.07	-
16	16GW	0.07	-	35, 36, 37	EL7, SH7, KB7	0.931	-

During the seismic tests, the superstructures were instrumented with seven accelerometers at every two floors from A1 at the frame basement to A7 at the top (see Figure 2.1). A0 was installed on the shake table. Thus, A0 measures the motions of seismic sources, and A1 measures the ground motion. The sampling frequency was chosen to be 250 Hz for all the accelerometer channels.

Once the acceleration datasets were measured at the shake table and the superstructure, they were preprocessed to obtain the corresponding velocity and displacement. First, the acceleration was detrended using polynomials with the decreasing orders of six to zero, and then lowpass filtered using a zero-phase distortion filter with the passband of 110 Hz, the stopband of 120 Hz, the passband ripple of 1 dB, and stopband attenuation of 60 dB.

## **2.4 Time-Domain Modal Analysis Methods**

Three modal analysis methods were used to identify the dynamic characteristics of the superstructures: the Deterministic Stochastic Subspace Identification (DSSI), Stochastic Subspace Identification (SSI), and Eigensystem Realization Algorithm with Natural Excitation Technique (NExT-ERA). Mathematical background of these methods is described in the subsequent subsections.

### **2.4.1 Deterministic Stochastic Subspace Identification (DSSI)**

DSSI was developed by Overschee and De Moor [18] for modal parameter identification of linear multi-input multi-output (MIMO) dynamic systems with known system *input* and *output* data. DSSI is based on the oblique projection of the future input and output measurements onto the past input and output measurements. A MIMO linear dynamic system with measurement uncertainty can be expressed using the following state space formulation:

$$\begin{aligned}z_{k+1} &= \mathbf{A}z_k + \mathbf{B}u_k + w_k \\ y_k &= \mathbf{C}z_k + \mathbf{D}u_k + v_k\end{aligned}\tag{2.1}$$

where  $\mathbf{A}$  ( $N \times N$ ),  $\mathbf{B}$  ( $N \times m$ ),  $\mathbf{C}$  ( $n \times N$ ) and  $\mathbf{D}$  ( $n \times m$ ) are the system matrices;  $y$  ( $n \times 1$ ),  $z$  ( $N \times 1$ ) and  $u$  ( $m \times 1$ ) are the output, state and input vectors, respectively;  $m$ ,  $n$  and  $N$  are the numbers of system input, output and state, respectively; and  $w$  ( $N \times 1$ ) and  $v$  ( $n \times 1$ ) are the white noise terms.

The output block Hankel matrix  $\mathbf{Y}_{(1|2i)}$  is constructed using measured output data:

$$\mathbf{Y}_{1|2i} = \begin{pmatrix} y_1 & y_2 & y_3 & \cdots & y_j \\ y_2 & y_3 & y_4 & \cdots & y_{j+1} \\ \vdots & \vdots & \vdots & \ddots & \vdots \\ y_i & y_{i+1} & y_{i+2} & \cdots & y_{i+j-1} \\ \hline y_{i+1} & y_{i+2} & y_{i+3} & \cdots & y_{i+j} \\ y_{i+2} & y_{i+3} & y_{i+4} & \cdots & y_{i+j+1} \\ \vdots & \vdots & \vdots & \cdots & \vdots \\ y_{2i} & y_{2i+1} & y_{2i+2} & \cdots & y_{2i+j-1} \end{pmatrix} = \begin{bmatrix} \mathbf{Y}_p \\ \mathbf{Y}_f \end{bmatrix} = \quad (2.2)$$

$$\begin{bmatrix} \mathbf{Y}_p^+ \\ \mathbf{Y}_f^- \end{bmatrix}$$

where  $i$  is the number of block rows with the total number of rows in the Hankel matrix of  $2i \times m$ .  $j$  is the number of columns that should be greater than  $2i$ ; and ideally close to infinity for statistical unbiasedness.  $\mathbf{Y}_p$  is the upper part of the Hankel matrix with  $i$  block rows.  $\mathbf{Y}_f$  is the bottom part with  $i$  block rows.  $\mathbf{Y}_p^+$  is the part with the top  $(i + 1)$  block rows; and  $\mathbf{Y}_f^-$  is the part with the bottom  $(i - 1)$  block rows. The input Hankel matrices,  $\mathbf{U}_p$ ,  $\mathbf{U}_f$ ,  $\mathbf{U}_p^+$  and  $\mathbf{U}_f^-$ , are defined in the same way defined to the above output Hankel matrices. The combination matrices  $\mathbf{W}_p$  and  $\mathbf{W}_p^+$  are defined using the input and output Hankel matrices as follows:

$$\mathbf{W}_p = \begin{pmatrix} \mathbf{U}_p \\ \mathbf{Y}_p \end{pmatrix}, \quad \mathbf{W}_p^+ = \begin{pmatrix} \mathbf{U}_p^+ \\ \mathbf{Y}_p^+ \end{pmatrix} \quad (2.3)$$

Then, the oblique projection matrix is used to express the effect of the future input on the future output through this projection process as

$$\mathbf{O}b_i = \mathbf{Y}_f / \mathbf{U}_f \mathbf{W}_p \quad (2.4)$$

The oblique projection matrix for  $i$  equals to the product of observability matrix and the state matrix [19] as

$$\mathbf{Ob}_i = \mathbf{\Gamma}_i \mathbf{Z}_i \quad (2.5)$$

where the observability matrix,  $\mathbf{\Gamma}_i$ ; and the state matrix,  $\mathbf{Z}_i$ , in which

$$\mathbf{\Gamma}_i = \begin{bmatrix} \mathbf{C} \\ \mathbf{CA} \\ \mathbf{CA}^2 \\ \vdots \\ \mathbf{CA}^{i-1} \end{bmatrix}, \quad \mathbf{Z}_i = [z_i z_{i+1} \cdots z_{i+j-2} z_{i+j-1}] \quad (2.6)$$

The singular value decomposition can be used to reduce the system order and to extract the observability matrix and the state matrix as

$$\mathbf{Ob}_i = (\mathbf{U}_1 \quad \mathbf{U}_2) \begin{pmatrix} \mathbf{S}_1 & \mathbf{0} \\ \mathbf{0} & \mathbf{0} \end{pmatrix} \begin{pmatrix} \mathbf{V}_1^T \\ \mathbf{V}_2^T \end{pmatrix} \quad (2.7)$$

The corresponding observability and state matrices are

$$\mathbf{\Gamma}_i = \mathbf{U}_1 \mathbf{S}_1^{\frac{1}{2}}, \quad \mathbf{Z}_i = \mathbf{S}_1^{\frac{1}{2}} \mathbf{V}_1 \quad (2.8)$$

The projection matrix for  $i + 1$  is defined as

$$\mathbf{Ob}_{i+1} = \mathbf{Y}_f^- / \mathbf{U}_f^- \mathbf{W}_p^+ = \mathbf{\Gamma}_{i-1} \mathbf{Z}_{i+1}, \quad \mathbf{Z}_{i+1} = \mathbf{\Gamma}_{i-1}^+ \mathbf{Ob}_{i+1} \quad (2.9)$$

where  $\mathbf{\Gamma}_{i-1}$  is easily determined by removing the last row block from  $\mathbf{\Gamma}_i$ ; and  $+$  indicates the pseudo-inverse. The system matrices can be estimated using the least square method for

$$\begin{pmatrix} \mathbf{Z}_{i+1} \\ \mathbf{Y}_i \end{pmatrix} = \begin{pmatrix} \hat{\mathbf{A}} & \hat{\mathbf{B}} \\ \hat{\mathbf{C}} & \hat{\mathbf{D}} \end{pmatrix} \begin{pmatrix} \mathbf{Z}_i \\ \mathbf{U}_i \end{pmatrix} + \begin{pmatrix} \rho_w \\ \rho_v \end{pmatrix} \quad (2.10)$$

Modal parameters can be calculated from the real transformation of  $\hat{\mathbf{A}}$  matrix and  $\hat{\mathbf{C}}$  matrix.

Eigenvalue decomposition can be employed to obtain discrete state eigenvalues.

$$\hat{\mathbf{A}} = \mathbf{\Psi} \hat{\mathbf{\Lambda}} \mathbf{\Psi} \quad (2.11)$$

where  $\Psi$  is the eigenvector; and  $\hat{\Lambda}$  is the discrete state eigenvalue. The corresponding continuous state eigenvalue can be obtained as

$$\Lambda = \frac{\ln(\hat{\Lambda})}{\Delta t} \quad (2.12)$$

where  $\Lambda$  is the continuous state eigenvalues; and  $\Delta t$  is the sampling interval. Finally, the natural frequencies and damping ratios of the system can be determined as

$$\omega_i = \sqrt{\sigma_i^2 + \Omega_i^2} \quad (2.13)$$

$$\zeta_i = -\cos[\tan(\Omega_i/\sigma_i)] \quad (2.14)$$

where  $\sigma_i = \text{Re}(\Lambda_i)$  and  $\Omega_i = \text{Im}(\Lambda_i)$ ;  $\text{Re}(\ )$  and  $\text{Im}(\ )$  are the real and imaginary parts of the complex number, respectively. The mode shape can be determined from the product of  $\hat{\mathbf{C}}$  and the eigenvector of  $\hat{\mathbf{A}}$  matrix as

$$\Upsilon = \hat{\mathbf{C}}\Psi \quad (2.15)$$

where  $\Upsilon$  is the mode shape matrix.

#### 2.4.2 Stochastic Subspace Identification (SSI)

SSI was also developed by Overschee and De Moor [18] for modal parameter identification of a linear system with *output-only* data. For such multi-output (MO) systems, the input is assumed to be “*white-noise*” excitation. The system can be expressed as the following state space equation:

$$\begin{aligned} z_{k+1} &= \mathbf{A}z_k + w_k \\ y_k &= \mathbf{C}z_k + v_k \end{aligned} \quad (2.16)$$

The orthogonal projection matrix is defined as

$$\mathbf{O}_i = \mathbf{E}(\mathbf{Y}_f | \mathbf{Y}_p) = \mathbf{Y}_f \mathbf{Y}_p^T (\mathbf{Y}_p \mathbf{Y}_p^T)^{-1} \mathbf{Y}_p \quad (2.17)$$

The orthogonal projection matrix can be expressed as the product of the observability matrix and the state matrix as

$$\mathbf{O}_i = \mathbf{\Gamma}_i \mathbf{Z}_i \quad (2.18)$$

The observability matrix and the state matrix can be extracted by using singular value decomposition as derived in Equations 2.7, 2.8 and 2.9:

$$\mathbf{O}_i = \mathbf{E}(\mathbf{Y}_f^- | \mathbf{Y}_p^+), \mathbf{O}_{i+1} = \mathbf{\Gamma}_{i-1} \mathbf{Z}_{i+1}, \mathbf{Z}_{i+1} = \mathbf{\Gamma}_{i-1}^+ \mathbf{O}_{i+1} \quad (2.19)$$

Modal parameters can be identified using the least squares methods for

$$\begin{pmatrix} \mathbf{Z}_{i+1} \\ \mathbf{Y}_i \end{pmatrix} = \begin{pmatrix} \hat{\mathbf{A}} \\ \hat{\mathbf{C}} \end{pmatrix} \mathbf{Z}_i + \begin{pmatrix} \rho_w \\ \rho_v \end{pmatrix} \quad (2.20)$$

### 2.4.3 Eigen Realization Algorithm with Natural Excitation Technique (NExT-ERA)

ERA was developed by Juang and Pappa [20] for modal parameter identification of a linear with *output-only* data. Unlike SSI, the system input of ERA is assumed to be *impulse* excitation. The equation of motion for a multi-degree-of-freedom (MDOF) system subject to impulse excitation can be expressed as

$$\mathbf{M}\ddot{\mathbf{X}}(t) + \mathbf{C}\dot{\mathbf{X}}(t) + \mathbf{K}\mathbf{X}(t) = 0 \quad (2.21)$$

where  $n_d$  is the number of the degrees of freedom of the system;  $N_t$  is the number of data points over time;  $\mathbf{M}$ ,  $\mathbf{C}$  and  $\mathbf{K}$  are the  $(n_d \times n_d)$  mass, damping and stiffness matrices, respectively;  $\mathbf{X}(t)$ ,  $\dot{\mathbf{X}}(t)$  and  $\ddot{\mathbf{X}}(t)$  are the  $(n_d \times N_t)$  displacement, velocity and

acceleration vectors, respectively. The Hankel matrix of the MDOF system can be defined as

$$\mathbf{H}(\mathbf{k} - \mathbf{1}) = \begin{bmatrix} \mathbf{Y}(k) & \mathbf{Y}(k + 1) & \cdots & \mathbf{Y}(k + p - 1 + s) \\ \mathbf{Y}(k + 1) & \mathbf{Y}(k + 2) & \cdots & \mathbf{Y}(k + p + s) \\ \vdots & \vdots & \ddots & \vdots \\ \mathbf{Y}(k + r - 1 + s) & \mathbf{Y}(k + r + s) & \cdots & \mathbf{Y}(k + p + r - 2 + 2 \times s) \end{bmatrix} \quad (2.22)$$

where  $(r + 1)$  is the number of row blocks in hankel matrix;  $(p + 1)$  is the number of the column blocks;  $s$  is the step shift in the final row block and column block with a default value of 10; and  $\mathbf{Y}$  is the  $(n \times m)$  Markov parameter matrix that can be expressed as

$$\mathbf{Y}(k) = \begin{bmatrix} Y_{11}(k) & Y_{12}(k) & \cdots & Y_{1m}(k) \\ Y_{21}(k) & Y_{22}(k) & \cdots & Y_{2m}(k) \\ \vdots & \vdots & \ddots & \vdots \\ Y_{n1}(k) & Y_{n2}(k) & \cdots & Y_{nm}(k) \end{bmatrix} \quad (2.23)$$

where  $Y_{ij}(i)$  is the impulse response of the  $i$ -th output due to the  $j$ -th input at time step  $k$ ;  $m$  is the number of the system output; and  $n$  is the number of system input. Then, the singular value decomposition is applied to  $\mathbf{H}(\mathbf{0})$ , the Hankel matrix at  $k = 1$ :

$$\mathbf{H}(\mathbf{0}) = \mathbf{RDS}^T \quad (2.24)$$

By eliminating low singular values in the diagonal matrix, the rows and columns corresponding to the low singular values are also eliminated from the matrices  $\mathbf{R}$ ,  $\mathbf{D}$  and  $\mathbf{S}$ .

Let the new *reduced-order* matrices be  $\mathbf{R}_N$ ,  $\mathbf{D}_N$  and  $\mathbf{S}_N$ . Finally, the discrete state space matrices are found as



$$\hat{\mathbf{A}} = \mathbf{D}_N^{-\frac{1}{2}} \mathbf{R}_N^T \mathbf{H}(1) \mathbf{S}_N \mathbf{D}_N^{-\frac{1}{2}}, \hat{\mathbf{B}} = \mathbf{D}_N^{\frac{1}{2}} \mathbf{S}_N^T \mathbf{E}_m, \hat{\mathbf{C}} = \mathbf{E}_n^T \mathbf{R}_N \mathbf{D}_N^{\frac{1}{2}} \quad (2.25)$$

where  $\mathbf{E}_m^T = [\mathbf{I}_m \mathbf{0}]$  and  $\mathbf{E}_n^T = [\mathbf{I}_n \mathbf{0}]$ ;  $\mathbf{I}_m$  and  $\mathbf{I}_n$  are identity matrices with dimensions of  $m$  and  $n$ , respectively.

Since *impulse* excitation is assumed in ERA (see RHS in Equation 2.21), the original technique should be modified to be applicable to a system subject to *forced* excitation, such as ambient vibration. NExT is used to convert forced vibration with *unknown* ambient excitation into impulse (or free) vibration [21]. This conversion is possible using the cross-correlation of the system displacement at a reference location and the other locations based on the assumption that the ambient excitation is a *white-noise* excitation. The dynamic system subject to white-noise excitation can be expressed as

$$\mathbf{M}\ddot{\mathbf{X}}(t) + \mathbf{C}\dot{\mathbf{X}}(t) + \mathbf{K}\mathbf{X}(t) = \mathbf{F}(t) \quad (2.26)$$

where  $\mathbf{F}(t)$  is the  $(n_d \times 1)$  unknown ambient force. Assuming that  $\mathbf{F}(t)$  is a weak stationary stochastic process, Equation 2.26 can be modified by multiplying a time-lagged displacement at a reference location on the both sides:

$$\mathbf{M}\ddot{\mathbf{X}}(t)X_{\text{ref}}(t - \tau) + \mathbf{C}\dot{\mathbf{X}}(t)X_{\text{ref}}(t - \tau) + \mathbf{K}\mathbf{X}(t)X_{\text{ref}}(t - \tau) = \mathbf{F}(t)X_{\text{ref}}(t - \tau) \quad (2.27)$$

where  $X_{\text{ref}}(t - \tau)$  is the reference displacement with a time lag,  $\tau$ . Taking an expectation operator  $E[ \ ]$ ,

$$\mathbf{M}E[\ddot{X}(t)X_{\text{ref}}(t - \tau)] + \mathbf{C}E[\dot{X}(t)X_{\text{ref}}(t - \tau)] + \mathbf{K}X(t)X_{\text{ref}}(t - \tau) = E[F(t)X_{\text{ref}}(t - \tau)] \quad (2.28)$$

$$\mathbf{M}R_{X_{\text{ref}}\ddot{X}}(\tau) + \mathbf{C}R_{X_{\text{ref}}\dot{X}}(\tau) + \mathbf{K}R_{X_{\text{ref}}X}(\tau) = R_{X_{\text{ref}}F}(\tau) \quad (2.29)$$

where  $R(\cdot)$  is the cross-correlation function. If the reference channel displacement and input force are statistically uncorrelated, the RHS of Equation 2.29 vanishes. Using the following relationships:

$$R_{X_{\text{ref}}\dot{X}}(\tau) = \dot{R}_{X_{\text{ref}}X}(\tau), \quad R_{X_{\text{ref}}\ddot{X}}(\tau) = \ddot{R}_{X_{\text{ref}}X}(\tau) \quad (2.30)$$

Equation 2.29 becomes

$$\mathbf{M}\ddot{R}_{X_{\text{ref}}X}(\tau) + \mathbf{C}\dot{R}_{X_{\text{ref}}X}(\tau) + \mathbf{K}R_{X_{\text{ref}}X}(\tau) = 0 \quad (2.31)$$

Therefore, the above derivation shows that a *particular* equation of motion for a dynamic system subject to forced vibration (see Equation 2.26) can be expressed with a *homogeneous* equation of motion using cross-correlation functions of displacements with respect to the displacement at a reference location. Finally, by applying the fourth-order time derivative to Equation 2.31.

$$\mathbf{M}\ddot{\ddot{R}}_{X_{\text{ref}}\ddot{X}}(\tau) + \mathbf{C}\dot{\ddot{R}}_{X_{\text{ref}}\ddot{X}}(\tau) + \mathbf{K}\ddot{R}_{X_{\text{ref}}\ddot{X}}(\tau) = 0 \quad (2.32)$$

Then, the original ERA technique can be applied to Equation 2.32 to obtain modal parameters (i.e., NExT-ERA).

For ERA, Due to the noise in the data, the system order should be chosen to be more than the real system order. Many studies, including Pappa et al. [22], discussed the

system order role on the realization. The mode condensation algorithm gives practical solution to distinguish between physical and noisy modes and perform the modal realization without the need to predefine the system order [22],[23].

Juang and Pappa [20] and Pappa et al. [24] suggested different mode indicators to measure the accuracy of mode identification. These mode indicators are incorporated in the mode condensation algorithm in order to separate physical modes from the noisy modes. The Consistent Mode Indicator (CMI) [24] used in this study is expressed as

$$CMI_i = EMAC_i \cdot MPC_i \quad (2.33)$$

where  $EMAC_i$  is the extend mode amplitude coherence of mode  $i$ , which quantifies the temporal consistency of the identified mode, and  $MPC_i$ , the modal phase collinearity, quantifies the spatial consistency of the corresponding mode. Therefore  $CMI_i$  quantify both of the temporal and spatial consistency.  $CMI_i, EMAC_i$ , and  $MPC_i$  have values from 0% to 100%.

## **2.5 Modal Analysis Results**

The objective of this study was to understand foundation effects on identified modal parameters of the superstructure by comparing the SFS systems with fixed, pile and box foundations at different damage stages. The modal parameters were identified using three different modal analysis methods including the NExT-ERA, SSI and DSSI. Thus, the identification results of those three modal analysis methods were also compared to investigate the effects of modal analysis methods using the same acceleration datasets collected from the SFS systems.

The all three modal analysis methods used in this study are time-domain modal analysis methods for linear dynamic systems. For DSSI, both the system input and output data (i.e., MIMO), or force and acceleration data respectively, are required in its system identification procedures. In field-monitoring applications for MDOF systems, the system input data are not always available due to technical challenges in obtaining force data and/or limitation due to sensing cost. For SSI and NExT-ERA, associated with the assumptions on the system input, only the system output data (i.e., MO) are required. Consequently, the accuracy of SSI and NExT-ERA is influenced by the validity of the assumptions. The required data, underlying assumptions and uncertainty terms of DSSI, SSI, ERA and NExT-ERA are summarized in Table 2.3.

Table 2.3: Comparison of different modal analysis methods.

Methods	Required data	Assumptions	Existence of uncertainty
DSSI	Input and output	The system is linear.	Input and output
SSI	Output	The system is linear; the system input is “white-noise” excitation.	Input and output
ERA	Output	The system is linear; the system input is impulse excitation.	None (deterministic)
NExT-ERA	Output	System is linear; the system input is “white-noise” excitation.	Input

The equation of motion for the superstructure can be expressed using the following MDOF *linear* equation:

$$\mathbf{M}\ddot{\mathbf{Y}}(t) + \mathbf{C}\dot{\mathbf{Y}}(t) + \mathbf{K}\mathbf{Y}(t) = -\mathbf{M}\ddot{\mathbf{u}}\ddot{s}(t) \quad (2.34)$$

where  $\mathbf{M}$ ,  $\mathbf{C}$  and  $\mathbf{K}$  are the  $(n_d \times n_d)$  mass, damping and stiffness matrices, respectively;  $\mathbf{Y}(t)$ ,  $\dot{\mathbf{Y}}(t)$  and  $\ddot{\mathbf{Y}}(t)$  are the  $(n_d \times N_t)$  relative displacement, velocity and acceleration vectors, respectively;  $\ddot{s}(t)$  is the base acceleration at A1 (see Figure 2.1); and  $\dot{\mathbf{Y}}(t) =$

$\ddot{X}(t) - \bar{u}\ddot{s}(t)$  in which  $\ddot{X}(t)$  is the absolute acceleration and  $\bar{u}(n_d \times N_t)$  is the unit column vector. The mass-normalized version of Equation 2.34 can be written as follows:

$$\ddot{Y}(t) + \mathbf{M}^{-1}\mathbf{C}\dot{Y}(t) + \mathbf{M}^{-1}\mathbf{K}Y(t) = -\bar{u}\ddot{s}(t) \quad (2.35)$$

where  $-\bar{u}\ddot{s}(t)$  is the system input; and  $\ddot{Y}(t)$ ,  $\dot{Y}(t)$  and  $Y(t)$  are the system output.

The acceleration datasets of the 40 tests in Table 2.1 were processed using the three modal analysis algorithms, DSSI, SSI and NExT-ERA. In this study, the modal analysis results of the SH datasets (see Tests 3, 6, 12, 18, 24 and 30 in Table 2.1) were used since the excitation has broader frequency bandwidths than the other two earthquake excitations, EL and KB, which is advantageous in reliable mode realization. The duration of SH was 15.73 seconds. Test 36 at Level-7 excitation was excluded from this study since the superstructure model with the fixed foundation completely failed after level-6 excitation test.

For DSSI, both the system input and output were used in the identification with the maximum number of modes set to be six for the fixed foundation cases, and 10 for the other foundation cases and six valid modes were manually selected. For SSI, only the system output,  $\dot{Y}(t)$ , was used in the identification. The maximum number of modes was consistently set to be 10 for all foundation cases, and six valid modes were manually selected. For NExT-ERA, the mode condensation algorithm [22] was used to evaluate the stabilization of mode realization for different system orders from 2 to 60 that is equivalent to the maximum number of modes from 1 to 30. For NExT, all channels were used as reference positions, but not simultaneously. Six valid modes were selected based on the

modes with six highest CMI values. All modes with CMI values less than 80% were excluded.

The identification results of modal parameters identified using DSSI, SSI and NExT-ERA are summarized in Tables 2.4 and 2.5. A total of 96 modes were identified using DSSI, 75 modes using SSI, and 64 modes using NExT-ERA. Figure 2.2 shows sample mode shapes of the superstructure with different foundation types. The 5th and 6th mode shapes for the fixed foundation were not realized using NExT-ERA, and the 6th mode shape for the pile foundations was not realized using NExT-ERA.

Table 2.4: Comparison of identified modal frequencies of the superstructure models with fixed, box, and pile foundations. Modal frequency is shown in Hertz (Hz).

Deterministic Stochastic Subspace Identification (DSSI)

Excit. Lv.	Fixed						Pile						Box					
	M1	M2	M3	M4	M5	M6	M1	M2	M3	M4	M5	M6	M1	M2	M3	M4	M5	M6
L1	3.19	12.48	22.59	33.58	45.87	62.11	3.06	14.65	26.31	39.17	53.99	71.13	1.32	14.79	25.75	38.90	52.74	81.09
L2	3.12	11.74	21.66	30.53	41.24	56.35	2.05	14.19	25.64	38.24	54.51	69.32	5.64	14.76	25.72	38.87	52.94	71.65
L3	2.88	10.66	19.51	28.74	39.97	52.47	1.61	12.99	22.77	36.04	46.35	60.52	4.35	14.49	25.31	38.32	52.88	71.10
L4	2.46	9.45	17.58	25.25	34.59	44.62	1.30	11.73	19.72	31.81	40.27	59.55	3.42	14.29	25.26	38.17	52.73	72.58
L5	2.13	8.48	15.66	22.04	30.38	40.42	1.21	10.52	19.54	31.41	38.05	56.58	3.37	14.06	25.19	38.59	51.52	69.09
L6	1.79	6.97	13.13	19.69	26.45	35.94	1.34	10.61	20.63	30.02	35.71	54.40	2.76	13.84	24.31	37.80	50.27	67.42

Stochastic Subspace Identification (SSI)

Excit. Lv.	Fixed						Pile						Box					
	M1	M2	M3	M4	M5	M6	M1	M2	M3	M4	M5	M6	M1	M2	M3	M4	M5	M6
L1	3.36	12.38	22.72	33.55	45.73	61.94	3.47	14.82	27.07	39.40	54.17	70.97	0.93	14.94	25.01	39.59	52.24	85.74
L2	2.85	11.51	22.25	30.44	44.29	58.79	2.12	14.74	26.44	38.54	54.24	70.46	2.68	14.96	26.10	39.10	55.82	73.48
L3	3.58	10.44	19.72	28.92	40.28	53.55	1.97	14.72	23.12	37.40	-	-	4.45	14.75	25.23	38.63	53.79	71.42
L4	2.73	9.34	18.22	26.60	35.53	46.43	-	12.19	-	-	-	-	4.27	14.36	24.87	38.19	51.49	73.99
L5	2.41	8.70	-	22.99	31.32	40.71	-	12.42	-	-	-	-	3.72	13.98	25.00	38.99	-	71.68
L6	-	6.54	-	20.38	26.03	36.08	1.83	10.93	-	33.06	-	56.57	1.55	13.87	24.45	-	-	-

### Eigensystem Realization Algorithm with Natural Excitation Technique (NExT-ERA)

Excit. Lv.	Fixed						Pile						Box					
	M1	M2	M3	M4	M5	M6	M1	M2	M3	M4	M5	M6	M1	M2	M3	M4	M5	M6
L1	3.37	12.73	22.09	33.39	46.57	61.71	3.45	14.21	26.59	39.45	-	-	4.62	14.51	25.50	-	-	-
L2	2.97	10.74	22.90	29.64	46.48	-	2.80	15.42	26.43	38.84	-	-	6.08	15.02	25.29	38.72	51.92	69.63
L3	2.80	10.50	18.82	26.55	40.07	-	5.73	13.25	22.34	39.77	-	-	3.53	14.34	24.35	39.25	-	69.91
L4	2.03	13.31	18.89	-	-	-	6.13	10.54	19.25	-	-	-	3.73	14.26	24.94	38.82	50.94	-
L5	1.59	9.35	-	-	35.43	-	-	12.05	-	36.34	-	-	4.44	13.57	25.69	39.76	51.50	-
L6	1.47	5.94	14.57	21.85	-	-	5.72	-	19.84	34.29	-	-	2.11	13.60	24.76	39.30	-	67.70



Table 2.5: Comparison of identified damping ratios of the superstructure models with fixed, box, and pile foundations. Damping ratio is in percentage (%).

Deterministic Stochastic Subspace Identification (DSSI)

Excit. Lv.	Fixed						Pile						Box					
	M1	M2	M3	M4	M5	M6	M1	M2	M3	M4	M5	M6	M1	M2	M3	M4	M5	M6
L1	9.73	4.72	4.55	4.22	4.39	4.29	7.88	2.50	2.66	2.13	4.63	5.12	58.36	3.21	10.39	3.81	9.06	9.17
L2	18.13	9.27	8.54	7.41	12.86	10.58	15.99	6.02	6.37	5.51	10.91	7.14	43.82	4.95	7.60	3.20	9.53	.69
L3	27.00	8.78	10.24	10.35	10.28	9.92	22.32	10.18	10.97	8.74	19.74	16.94	51.56	4.86	7.13	3.55	14.68	.76
L4	42.23	12.94	11.18	12.66	13.34	10.83	24.44	17.38	8.54	9.09	23.54	16.04	44.28	3.01	6.83	3.55	14.47	3.85
L5	50.81	15.54	16.10	15.16	12.99	10.35	28.79	16.38	11.42	9.45	35.18	19.58	51.34	4.03	6.09	3.92	2.42	.25
L6	79.96	16.32	21.07	15.29	13.26	12.83	67.22	17.10	8.22	8.53	28.19	21.03	54.83	4.41	7.24	5.03	5.31	7.66

Stochastic Subspace Identification (SSI)

Excit. Lv.	Fixed						Pile						Box					
	M1	M2	M3	M4	M5	M6	M1	M2	M3	M4	M5	M6	M1	M2	M3	M4	M5	M6
L1	8.11	5.42	4.32	4.79	5.26	5.66	26.76	7.83	4.01	2.83	7.60	5.97	4.04	6.28	17.52	5.07	15.38	17.81
L2	15.02	12.32	9.06	9.13	15.45	10.39	47.56	8.21	10.91	6.86	13.58	6.62	91.74	7.17	13.69	5.37	18.14	7.95
L3	30.80	6.34	12.07	10.95	9.97	11.58	53.63	21.87	15.24	8.11	-	-	51.13	8.09	9.54	5.63	23.60	6.78
L4	79.51	21.78	15.17	16.29	18.10	13.98	-	20.75	-	-	-	-	67.37	8.30	9.34	4.63	19.47	12.66
L5	84.68	19.03	-	17.69	17.99	12.79	-	29.48	-	-	-	-	85.00	8.35	9.01	4.72	-	7.95
L6	-	14.59	-	17.82	19.01	15.74	76.43	20.11	-	7.59	-	15.93	89.69	7.73	11.37	-	-	-

### Eigensystem Realization Algorithm with Natural Excitation Technique (NExT-ERA)

Excit. Lv.	Fixed						Pile						Box					
	M1	M2	M3	M4	M5	M6	M1	M2	M3	M4	M5	M6	M1	M2	M3	M4	M5	M6
L1	10.46	2.28	2.15	2.90	2.58	1.88	18.66	3.04	1.42	1.09	-	-	21.52	3.91	5.51	-	-	
L2	9.59	6.32	3.11	3.70	2.79	-	34.96	3.76	3.64	3.10	-	-	26.64	2.70	4.68	1.91	3.73	1.42
L3	20.45	4.95	3.98	4.61	3.80	-	15.52	8.58	6.04	5.26	-	-	17.56	7.64	2.42	2.72	-	1.01
L4	29.00	7.43	2.90	-	-	-	11.41	9.67	3.59		-	-	27.02	5.18	3.00	1.84	3.52	-
L5	28.16	16.33	-	-	8.73	-	-	8.75	-	2.81	-	-	34.79	3.94	4.82	1.44	2.38	-
L6	37.19	3.00	11.06	9.21	-	-	22.66	-	5.47	3.49	-	-	24.56	3.36	7.49	1.89	-	2.41

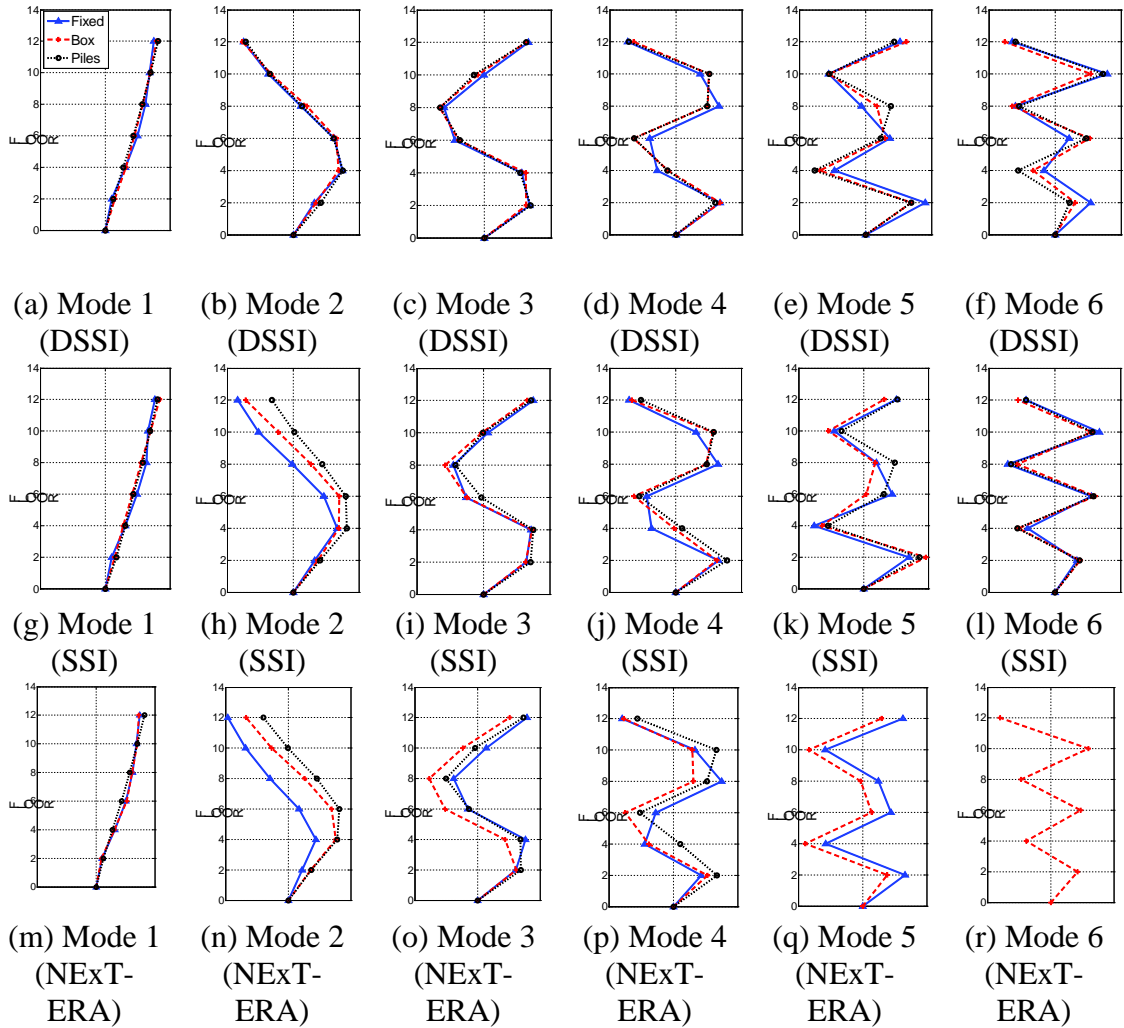


Figure 2.2: Comparison of the mode shapes of the superstructures with the fixed, pile and box foundations, identified using DSSI, SSI and NExT-ERA.

## 2.6 Discussion

The results of the modal analysis are discussed in this section. The identification errors are quantified and discussed in Section 2.6.1. The effects of nonlinearity on modal parameter identification are discussed in Section 2.6.2. The effects of foundation types are discussed in Section 2.6.3. The modal parameters identified using different modal analysis methods are compared and discussed in Section 2.6.4.

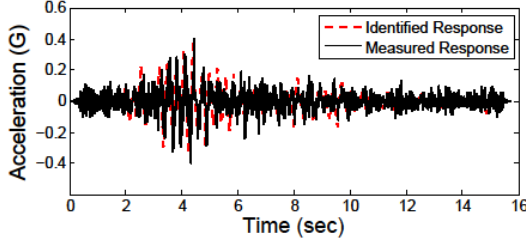
### 2.6.1 Quantification of Identification Errors

To evaluate identification accuracy in section 2.5, DSSI identification errors were quantified for the MIMO superstructure model with the fixed foundation. With the identified modal parameters in Tables 2.4 and 2.5, identified system output was calculated using the following state space model for the system input of  $u_k = -\bar{u}\ddot{s}_k$  (see Equation 2.1):

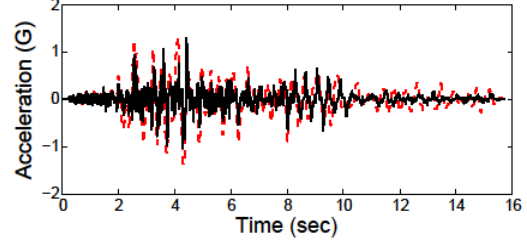
$$\begin{aligned}\hat{z}_{k+1} &= \hat{\mathbf{A}}z_k + \hat{\mathbf{B}}(-\bar{u}\ddot{s}_k) \\ \hat{Y}_k &= \hat{\mathbf{C}}z_k + \hat{\mathbf{D}}(-\bar{u}\ddot{s}_k)\end{aligned}\tag{2.36}$$

where  $\hat{\Lambda}$  represents estimate.

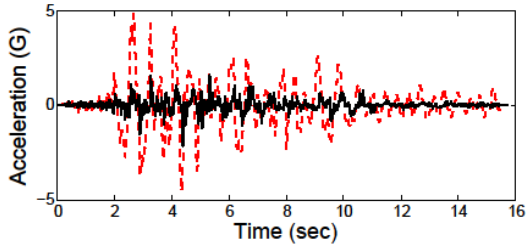
A comparison between the measured and identified system output for different excitation levels is shown in Figure 2.3. The time histories show that the magnitude of the identified acceleration (dashed line) is overestimated compared to the measured acceleration (solid line) as the excitation level increases.



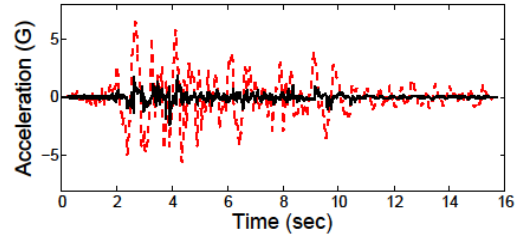
(a) Excitation level 1 (peak acc. = 0.093 G)



(b) Excitation level 3 (peak acc. = 0.399 G)



(c) Excitation level 5 (peak acc. = 0.665 G)



(d) Excitation level 6 (peak acc. = 0.798 G)

Figure 2.3: A comparison between the measured and identified system output for different excitation levels. The system output is for the acceleration on the 12-th floor (A7) of the superstructure with the fixed foundation.

For further investigation, the error between the measured and identified accelerations was measured using three different indices: i) energy ratio,  $R_E$ , ii) time lag,  $\tau$ , and iii) correlation coefficient,  $r$ , as shown in the following equations:

$$R_E = \frac{P(\hat{Y}_k)}{P(\dot{Y}_k)} = \frac{\sum_{k=1}^n \hat{Y}_k \hat{Y}_k}{\sum_{k=1}^n \dot{Y}_k \dot{Y}_k} \quad (2.37)$$

$$\begin{aligned} \tau &= \arg \max_t \left( R(\hat{Y}_k, \dot{Y}_k)(t) \right) \Delta t \\ &= \arg \max_t \left( \frac{1}{n-t} \sum_{k=t+1}^n \hat{Y}_k \dot{Y}_{k-t} \right) \Delta t \end{aligned} \quad (2.38)$$

$$r = \frac{R(\hat{Y}_k, \ddot{Y}_k)}{\sqrt{P(\hat{Y}_k)P(\ddot{Y}_k)}} = \left( \frac{n}{n - \tau/\Delta t} \right) \frac{\sum_{k=\frac{\tau}{\Delta t}+1}^n \hat{Y}_k \ddot{Y}_{k-\tau/\Delta t}}{\sqrt{\left( \sum_{k=1}^n \hat{Y}_k \hat{Y}_k \right) \left( \sum_{k=1}^n \ddot{Y}_k \ddot{Y}_k \right)}} \quad (2.39)$$

where  $P(\cdot)$  is the power of signal;  $\Delta t$  is the time step; and  $R(\cdot)$  is the cross-correlation function. The energy ratio was measured to quantify the error between the two signals in terms of their magnitude, while the time lag and correlation coefficient were to measure to quantify the error in terms of their phase.

The error analysis results are shown in Figure 2.4. The energy ratio increases as the peak acceleration increases for all floors (see Figure 2.4a). For a given peak acceleration, a larger energy ratio is observed for an upper floor. For  $R_E > 1$ , the magnitude of the identified acceleration is larger than that of the measurement acceleration. Therefore, the result shows that the identified acceleration is overestimated in terms of its magnitude with strong ground motion.

Figure 2.4b shows the time lag between the identified and measured acceleration for their maximum cross correlation. In the figure, the positive time lag means the identified acceleration is shifted to right compared to the measured acceleration. It is observed that the time lag increases as the peak acceleration increases. For a given peak acceleration, the time lag increases for an upper floor. Therefore, this result shows that the phase error tends to increase with strong ground motion. A similar result can be observed in the correlation coefficient. Figure 2.4c shows that the correlation coefficient decreases as the peak acceleration increases for all floors. Since the cross correlation decreases when the error in phase increases, the result shows that the phases of the identified and measured

acceleration are less correlated with stronger ground motion. For a given peak acceleration, the cross correlation decreases for a lower floor. This is because the measured acceleration on a lower has more high-frequency contents than the acceleration on an upper floor (compare Figure 2.3a and 2.3d).

The escalated errors with stronger ground motion would be due to the effect of the superstructure's nonlinear behaviors. The nonlinear effects can be caused by two reasons. One may be that the superstructure dynamic response exceeded its linear range at higher ground peak acceleration. The other may be due to damage accumulated in the superstructure as a series of the seismic tests were conducted. In modal analysis, however, the superstructure is assumed to be a linear system in DSSI, SSI and NExT-ERA. Consequently, the identification results are inaccurate when these nonlinear effects are significant.

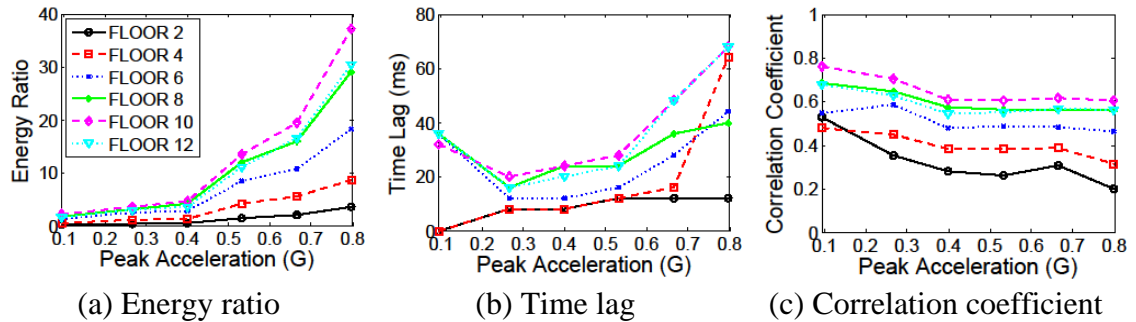


Figure 2.4: DSSI errors for the superstructure with the fixed foundation at different excitation levels.

### 2.6.2 Effects of System Nonlinearity

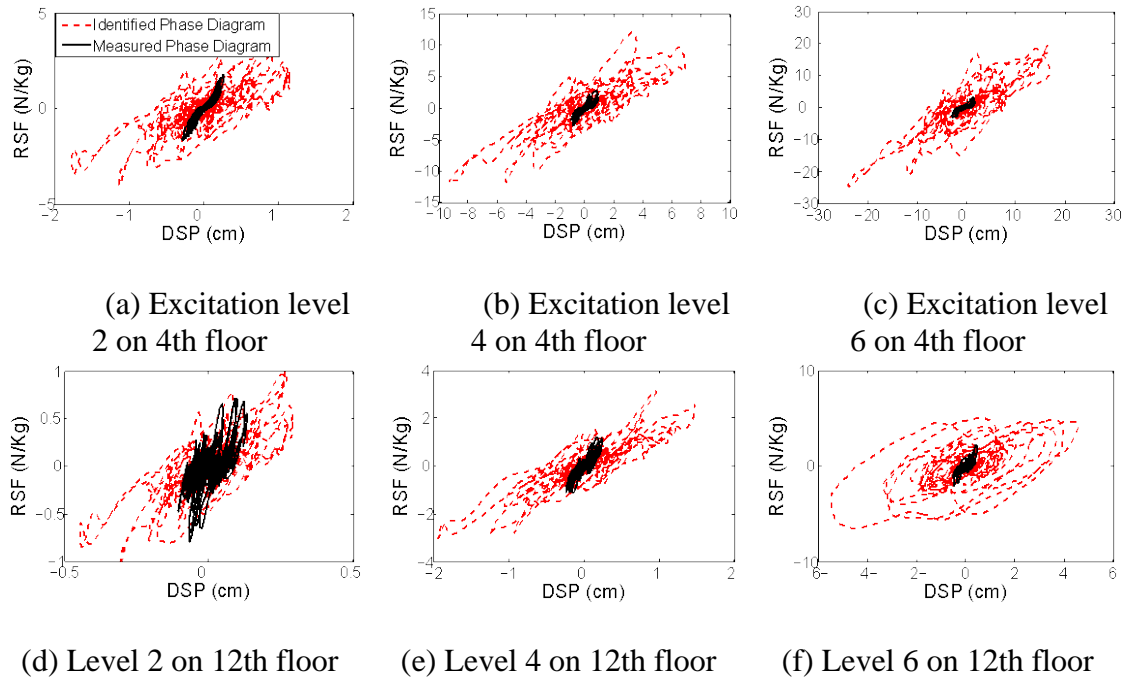
To investigate the nonlinearity effects on mode identification, the interstory restoring force was calculated using the following equation [25]:

$$\begin{aligned}
\frac{G_n(z_n, \dot{z}_n)}{m} &= -\ddot{x}_n \\
\frac{G_{n-1}(z_{n-1}, \dot{z}_{n-1})}{m} &= -\ddot{x}_{n-1} + \frac{G_n(z_n, \dot{z}_n)}{m} \\
&\vdots \\
\frac{G_2(z_2, \dot{z}_2)}{m} &= -\ddot{x}_2 + \frac{G_3(z_3, \dot{z}_3)}{m} \\
\frac{G_1(z_1, \dot{z}_1)}{m} &= -\ddot{x}_1 + \frac{G_2(z_2, \dot{z}_2)}{m}
\end{aligned} \tag{2.40}$$

where  $G_k$  is the nonlinear interstory restoring force of the  $2k$ -th floor mass;  $m_k$  is the interstory mass of the  $2k$ -th floor, and  $m = m_1 = \dots = m_6$ ;  $z_1 = x_1 - s$ , and  $\dot{z}_1 = \dot{x}_1 - \dot{s}$ ;  $z_k = x_k - x_{k-1}$ , and  $\dot{z}_k = \dot{x}_k - \dot{x}_{k-1}$  for  $2 \leq k \leq 6$ ;  $x_k$  and  $\dot{x}_k$  are the absolute displacement and velocity of the  $2k$ -th floor, respectively;  $s$  and  $\dot{s}$  are the ground displacement and velocity, respectively.

Figure 2.5 shows the phase diagrams of the 12th-floor restoring force,  $G_6$ , for the superstructure with the fixed foundation subject to different excitation levels.  $\hat{x}_k$  and  $\hat{\dot{x}}_k$  were calculated through the numerical integration of the identified acceleration of  $\hat{\ddot{x}}_k$ , and  $x_k$  and  $\dot{x}_k$  were calculated through the numerical integration of the measured acceleration of  $\ddot{x}_k$ . The figure shows that the discrepancy between the identified (dashed line) and measured (solid line) restoring-force phase diagrams increases as the excitation level increases, similar to the results in Figure 2.3.





(a) Excitation level 2 on 4th floor      (b) Excitation level 4 on 4th floor      (c) Excitation level 6 on 4th floor  
 (d) Level 2 on 12th floor      (e) Level 4 on 12th floor      (f) Level 6 on 12th floor  
 Figure 2.5: Comparison of the identified and measured restoring-force phase diagrams for the superstructure with the fixed foundation subject to different excitation levels. The identified phase diagram was calculated using DSSI.

Figure 2.6 shows the measured restoring-force phase diagrams for the superstructure with the fixed foundation (solid lines). It turned out that the nonlinearity of the superstructure increased at all floors with a stronger ground motion, including stiffness hardening and hysteresis since the structure response exceeded its linear range at a high excitation level. The linear interstory stiffness of the identified restoring phase diagram was estimated using the least square regression with the first-order polynomial (dashed lines) and compared with the measured restoring-force phase diagrams. Interestingly, in spite of the large discrepancy between the measured and identified restoring-force diagrams in Figure 2.5, the identified linear interstory stiffness (dashed lines) was close to the linear stiffness of the measured restoring-force phase diagrams (solid lines). The error

of the identified linear stiffness increased for large displacements due to the stiffness hardening in the measured phase diagrams.

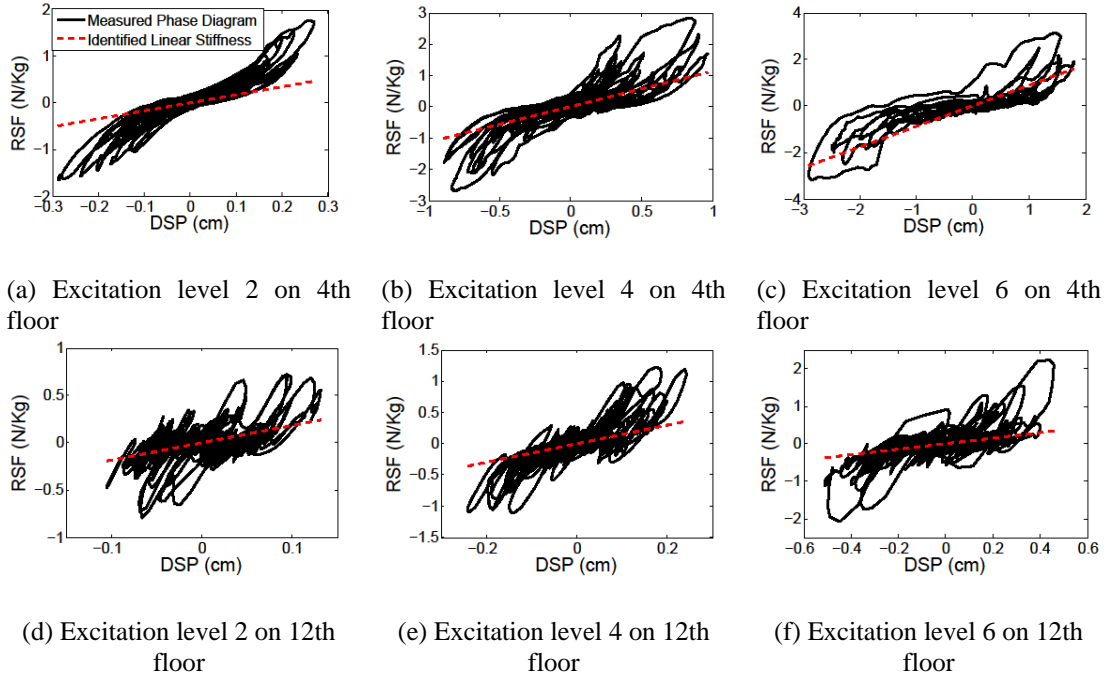


Figure 2.6: Measured restoring-force phase diagrams for the superstructure with the fixed foundation (solid line). The linear stiffness was estimated using the least square regression of the identified restoring-force phase diagrams with the first-order polynomial (dashed line).

The linear stiffness of the identified restoring-force diagram estimated using the least square regression with the first-order polynomial was calculated for different peak acceleration using the superstructure with the fixed foundation. Figure 2.7 shows the change of the identified linear stiffness of different floors for increasing excitation levels. It is observed that the linear stiffness of all floors decreases as the excitation level increases. The reduction of the linear stiffness reflects the effect of accumulated damage in superstructure during the tests.

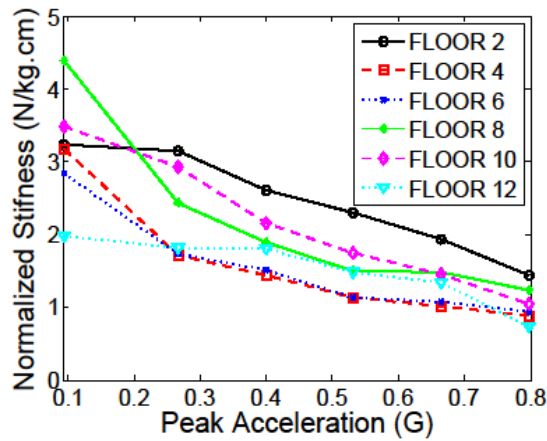


Figure 2.7: Change of the linear interstory stiffness for different excitation levels.

### 2.6.3 Effects of Foundation Type

The effects of different foundation types on modal parameter identification were also investigated. Figure 2.8 shows the change of modal parameters of the superstructures with the fixed, pile and box foundations for the escalating peak acceleration of the shake table motion. The identified modal frequencies and damping ratios using DSSI are compared in the figure. The modal frequencies for the fixed foundation decreased as the peak acceleration increased (see Figure 2.8a), while the modal frequencies for the box foundation remained relatively constant (see Figure 2.8c). It was observed that the reduction rate of the modal frequencies for the pile foundation was approximately between those for the fixed and box foundations (see Figure 2.8b). On the other hand, the damping ratios for the fixed foundation increased as the excitation level (see Figure 2.8d), while the damping ratios for the box foundation remained constant (see Figure 2.8f). The rising rate of the damping ratios for the pile foundation is between those for the fixed and box foundations (see Figure 2.8e).

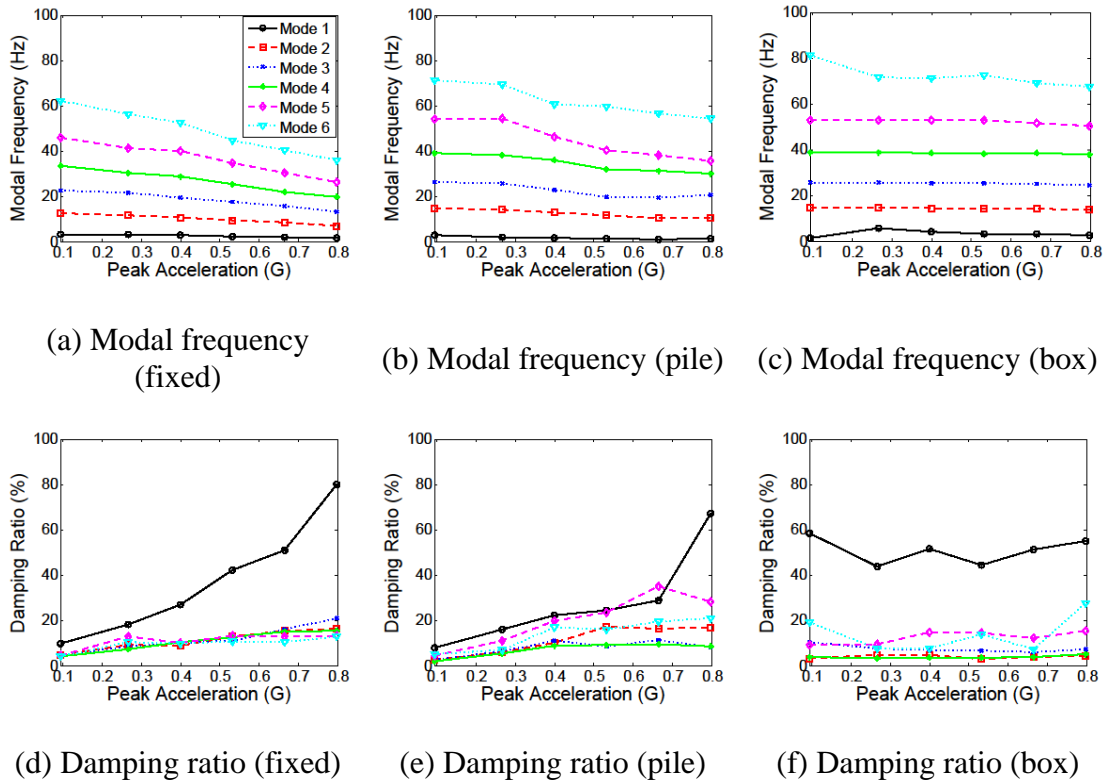


Figure 2.8: Change of the modal parameters using DSSI for different foundation types.

The reduced modal frequencies and rising damping ratios were due to structural damage accumulated in the superstructures during the seismic tests. Visual inspection during and after the tests showed that the superstructure with the *fixed* foundation had the most severe damage out of those three foundation types. After the tests, severe damage was found concentrating on lower floors, including crushed concrete columns on floors 2 and 3, and major horizontal cracks on the columns on floors 1–3. For the superstructure with the *pile* foundation, major cracks were observed on the first-floor columns and fine cracks on the beams on floors 1–6. The least severe damage was observed from the superstructure

with the *box* foundation after the tests, including only fine cracks on the beams on floors 1–5 and on the columns on the first floor.

The amount of seismic energy fed into the superstructures varied depending on the foundation type. Figure 2.10 shows the amount of energy transferred from the shaker to the superstructure base for different foundation types. For the fixed foundation, almost all seismic energy generated from the shaker (i.e., A0) was transferred to the superstructure base (i.e., A1) since the superstructure was rigidly connected to the shaker (see Figure 2.9a). The least amount of seismic energy was transferred to the superstructure with the box foundation due to energy dissipation through the soil and foundation (see Figure 2.9c). For the pile foundation, the amount of energy was larger than the energy for the box foundation and smaller than the energy for the fixed foundation (see Figure 2.9b). Interestingly, the ground energy decreased after the level-3 excitation (i.e., the peak acceleration of 0.399 G) due to damage in the piles.

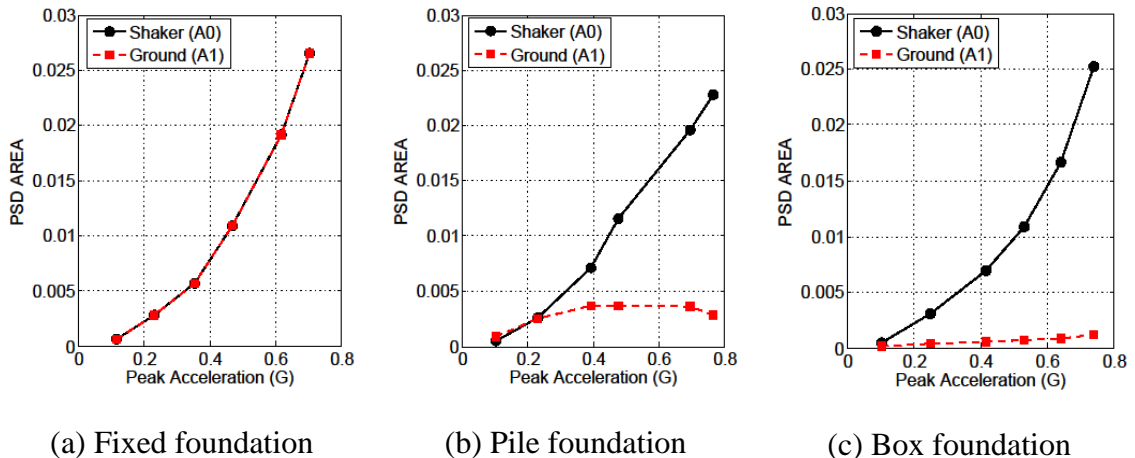


Figure 2.9: The energies of the acceleration at the shaker (A0) and the superstructure base (A1) for different foundation types. The energy was calculated by measuring the area of the power spectral density of acceleration at the sensors A0 and A1.

Since the foundation type determines the boundary conditions of the superstructure, the dynamic properties of the superstructure are largely affected by the foundation type for the given shake table motion (A0). The above results show the modal parameters identified using DSSI have a good correlation with physical structural damage during the tests for all three foundation types.

#### **2.6.4 Effects of Modal Analysis Methods**

To investigate the effects of modal analysis methods, the modal parameters identified using DSSI, SSI and NExT-ERA are compared. Figure 2.10 shows the three lowest modal frequencies and damping ratios of the superstructure with the fixed foundation. The identified modal frequencies with all three modal analysis methods decrease as the peak acceleration increases, while the damping ratios identified with all three modal analysis methods increase as the peak acceleration increases. The decreasing modal frequencies and increasing damping ratios are due to accumulated damage in the superstructure during the shake table tests. Thus, these identification results show that all three modal analysis methods can be used to quantify damage severity in the superstructure. It is also observed that the trends of identified modal frequency and damping ratio with DSSI less fluctuate for increasing peak acceleration than those with SSI and NExT-ERA. The larger fluctuation with SSI and NExT-ERA may be due to the validity of assumption on the system input (i.e., “white noise” excitation). DSSI estimates more reliable modal parameters than the other methods since DSSI requires using measured

excitation instead of relying on the white noise assumption of system input. However, the excitation measurement of each floor is not always available in many field monitoring applications.

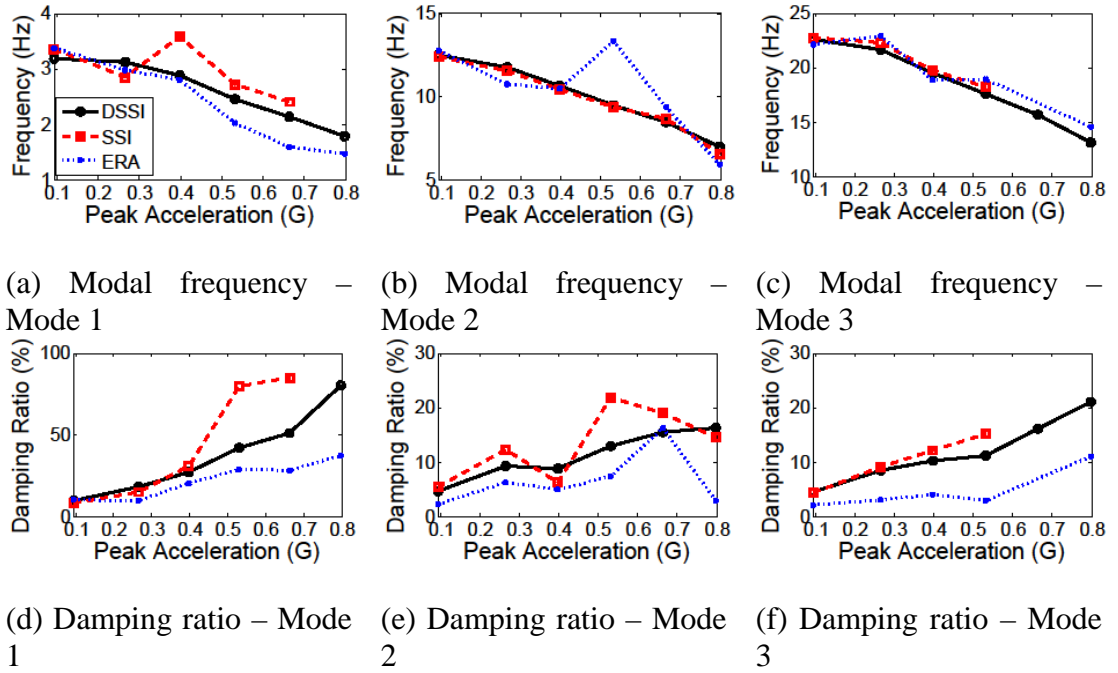
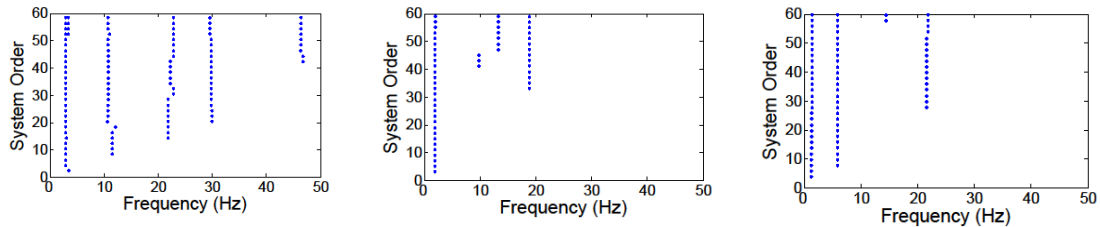


Figure 2.10: Change of identified modal parameters for the superstructure with the fixed foundation for DSSI, SSI and NExT-ERA.

The stabilization diagram is commonly used to determine true modes among multiple sets of modal parameters. These diagrams visualize the stability in the realization of modal frequencies. Figure 2.11 shows the stabilization diagrams of the modal frequencies identified with NExT-ERA. The figure shows the change of the modal frequencies with increasing system orders for the excitation levels of 2, 4 and 6. The figure shows that overall the realization of the modal frequencies is stable at different frequencies. In addition, less high-modal frequencies were realized for higher excitation levels (see

Table 2.4) using the given mode realization criteria of NExT-ERA described in Section 2.5. This may be due to higher nonlinear damage effect with higher excitation levels.



(a) Excitation level 2  
(peak acc. = 0.266 G)

(b) Excitation level 4  
(peak acc. = 0.532 G)

(c) Excitation level 6  
(peak acc. = 0.798 G)

Figure 2.11: Stabilization diagrams of NExT-ERA for the superstructure with the fixed foundation.

## 2.7 Conclusion

The 1:10-scale 12-story concrete frame models with the fixed, pile and box foundations embedded in soil were tested on the shake table using three different excitation waves of the peak acceleration escalated from 0.093 G to 0.931 G. Therefore, structural damage was accumulated in the SFS systems during the shake table test. A comparative study was conducted to investigate the effects of the different foundation effects on modal analysis results. The modal parameters of the superstructures were identified using widely accepted time-domain modal analysis methods of DSSI, SSI and NExT-ERA. The modal parameters identified using these three methods were also compared. From this comparison study, the following findings were observed related to different effects on modal parameter identification:

- The identification errors were quantified in terms of energy ratio, time lag and correlation coefficient between the measured and identified dynamic response



of the superstructures. It was found that the identification errors increased due to increasingly accumulated damage effects during the shake table tests.

- The nonlinearity effects, such as stiffness hardening and hysteresis, were observed in the superstructure's dynamic response. The error between the measured and identified response increases as the excitation level increases. The linear stiffness of the superstructure could be estimated with the linear slope of the identified displacement-restoring force phase diagram.
- Foundation types also affect the modal parameter identification of the superstructure. Visual inspection during and after shake table tests reveal the fixed foundation had the most severe damage in the superstructure, and the box foundation had the least severe damage in the superstructure. The difference of structural damage was due to load transfer with different foundation types from the shake table to the base of the superstructure. The identified modal frequencies and damping ratios agreed with the visual inspection results. The highest reduction rate of the modal frequency was observed with the rigid foundation (i.e., fixed foundation), and the lowest reduction rate of the modal frequency was observed with flexible foundation (i.e., box foundation). The highest increasing rate of the damping ratio was observed with the rigid foundation, and the lowest increasing rate of the damping ratio was observed with the flexible foundation. Thus, the identified modal parameters can be used as good indicators to measure structural damage.

- The effects of modal analysis methods on the modal parameter identification were also investigated. All tested modal analysis methods, including DSSI, SSI and NExT-ERA, could be used to quantify the structural damage in the superstructures. With the measurements of the system input, DSSI had the least fluctuation in the identified modal parameters. However, the measurements are not always available in many monitoring applications.

The identification methods used in this study are global identification techniques based on the assumption of linear dynamic characteristics of the superstructure. The above results show that the identified dynamic response of the superstructure can be significantly erroneous when nonlinear effects of the SFS system are not negligible. However, the identified modal frequencies and damping ratios can still be used as an indicator to quantify linear damage effect of the superstructure.

## **2.8 Acknowledgement**

This work was partially supported by the project (Grant No. 51178349) of the National Natural Science Foundation of China, the Kwang-Hua Foundation for the College of Civil Engineering at Tongji University, China, and research collaboration between the University of Central Florida (UCF), and Korea Institute of Construction Technology (KICT).

## **2.9 References**

- [1] P. Cawley and R. D. Adams, “The location of defects in structures from measurements of natural frequencies,” *The Journal of Strain Analysis for Engineering Design*, vol. 14, no. 2, pp. 49–57, Apr. 1979.
- [2] C. Farrar, S. W. Doebling, P. J. Cornwell, and E. G. Straser, “Variability of modal parameters measured on the Alamosa Canyon Bridge,” in *Proc. 15th International Modal Analysis Conf., Orlando, FL*, 1997, pp. 257–263.
- [3] M. A. Wahab and G. De Roeck, “Effect of Temperature on Dynamic System Parameters of a Highway Bridge,” *Structural Engineering International*, vol. 7, no. 4, pp. 266–270, Nov. 1997.
- [4] O. S. Salawu, “Detection of structural damage through changes in frequency: a review,” *Engineering Structures*, vol. 19, no. 9, pp. 718–723, Sep. 1997.
- [5] H. J. Salane and J. W. Baldwin, “Identification of Modal Properties of Bridges,” *Journal of Structural Engineering*, vol. 116, no. 7, pp. 2008–2021, Jul. 1990.
- [6] C. R. Farrar and D. A. Jauregui, “Comparative study of damage identification algorithms applied to a bridge: i. experiment,” *Smart Materials and Structures*, vol. 7, no. 5, pp. 704–719, Oct. 1998.

- [7] W. M. West, “Illustration of the use of modal assurance criterion to detect structural changes in an Orbiter test specimen,” in *Proc. Air Force Conference on Aircraft Structural Integrity*, 1984, pp. 1–6.
- [8] J. Bielak, “Dynamic behaviour of structures with embedded foundations,” *Earthquake Engineering & Structural Dynamics*, vol. 3, no. 3, pp. 259–274, 1974.
- [9] A. S. Veletsos and J. W. Meek, “Dynamic behaviour of building-foundation systems,” *Earthquake Engineering & Structural Dynamics*, vol. 3, no. 2, pp. 121–138, 1974.
- [10] J. Bielak, “Dynamic response of non-linear building-foundation systems,” *Earthquake Engineering & Structural Dynamics*, vol. 6, no. 1, pp. 17–30, Jan. 1978.
- [11] K. T. Chau, C. Y. Shen, and X. Guo, “Nonlinear seismic soil–pile–structure interactions: Shaking table tests and FEM analyses,” *Soil Dynamics and Earthquake Engineering*, vol. 29, no. 2, pp. 300–310, 2009.
- [12] R. Paolucci, M. Shirato, and M. T. Yilmaz, “Seismic behaviour of shallow foundations: Shaking table experiments vs numerical modelling,” *Earthquake Engineering & Structural Dynamics*, vol. 37, no. 4, pp. 577–595, Apr. 2008.
- [13] M. Lou, H. Wang, X. Chen, and Y. Zhai, “Structure–soil–structure interaction: literature review,” *Soil Dynamics and Earthquake Engineering*, vol. 31, no. 12, pp. 1724–1731, Dec. 2011.

- [14] S. Shang, Z. Zhu, W. Tu, and F. Xie, "Modal experimental analysis for soil-box foundation-structure dynamic interaction system [J]," *Journal of Hunan University (Natural Science)*, vol. 5, p. 017, 2004.
- [15] C. Bo, X. Lu, P. Li, and Y. Chen, "Modeling of dynamic soil-structure interaction by ANSYS program," *2nd Canadian Specialty Conference on Computer Applications in Geotechnique*, vol. 1, no. December, pp. 21–26, 2002.
- [16] X. Lu, P. Li, Y. Chen, and B. Chen, "Shaking table model testing on dynamic soil-structure interaction system," in *13th World Conference on Earthquake Engineering*, 2004, no. 3231.
- [17] X. Lu, P. Li, B. Chen, and Y. Chen, "Computer simulation of the dynamic layered soil-pile-structure interaction system," *Canadian Geotechnical Journal*, vol. 42, no. 3, pp. 742–751, 2005.
- [18] P. Van Overschee and B. De Moor, *Subspace Identification for Linear Systems: Theory, Implementation, Applications*. Kluwer Academic Publishers, Norwell, Massachusetts, USA., 1996.
- [19] H. Thai, V. DeBrunner, L. S. DeBrunner, J. P. Havlicek, K. Mish, K. Ford, and A. Medda, "Deterministic - Stochastic Subspace Identification for Bridges," *2007 IEEE/SP 14th Workshop on Statistical Signal Processing*, pp. 749–753, Aug. 2007.

- [20] J.-N. Juang and R. S. Pappa, “Effects of noise on modal parameters identified by the Eigensystem Realization Algorithm,” *Journal of Guidance, Control, and Dynamics*, vol. 9, no. 3, pp. 294–303, May 1986.
- [21] G. H. James, T. G. Carne, and J. P. Lauffer, “The Natural Excitation Technique (NExT) for Modal Parameter Extraction From Operating Wind Turbines,” Sandia National Laboratories,, 1993.
- [22] R. S. Pappa, G. H. James, and D. C. Zimmerman, “Autonomous modal identification of the space shuttle tail rudder,” *Journal of Spacecraft and Rockets*, vol. 35, no. 2, pp. 163–169, 1998.
- [23] R. D. Nayeri, F. Tasbihgoo, M. Wahbeh, J. P. Caffrey, S. F. Masri, J. P. Conte, and A. Elgamal, “Study of Time-Domain Techniques for Modal Parameter Identification of a Long Suspension Bridge with Dense Sensor Arrays,” *Journal of Engineering Mechanics*, vol. 135, no. 7, p. 669, 2009.
- [24] R. Pappa, K. Elliott, and A. Schenk, “A consistent-mode indicator for the eigensystem realization algorithm,” *Journal of Guidance Control and Dynamics (1993)*, 1993.
- [25] R. D. Nayeri, S. F. Masri, R. G. Ghanem, and R. L. Nigbor, “A novel approach for the structural identification and monitoring of a full-scale 17-story building based on ambient vibration measurements,” *Smart Materials and Structures*, vol. 17, no. 2, p. 025006, Apr. 2008.

## **CHAPTER 3: QUANTIFICATION OF LOCALIZED EARTHQUAKE DAMAGE EFFECTS ON LARGE-SCALE SOIL-FOUNDATION-SUPERSTRUCTURE SYSTEMS USING NONLINEAR IDENTIFICATION METHOD**

### **3.1 Abstract**

This paper presents the quantification, characterization and localization of nonlinear damage effects on soil-foundation-superstructure (SFS) systems using nonlinear system identification method. For realistic damage quantification, a series of shake table tests were conducted using 12-stories reinforced cast-in-place concrete frames with fixed, pile and box foundations. The Multi-degree-of-freedom Restoring Force Method (MRFM) was employed as a nonlinear system identification technique using the measurements of the superstructure dynamic response. The identification results were validated with visual inspection independently conducted during and after the shaker tests. The results show that MRFM can be used to quantify significant nonlinear effects of interstory damage on the SFS systems by differentiating the effects of the foundation types. The comparison of the identification results using MRFM and classical modal analysis technique demonstrates that MRFM has many advantages in monitoring for realistic earthquake-induced damage in building structures.

### **3.2 Introduction**

Quantification of localized damage effects on building structures has been an important research topic in earthquake engineering and structural health monitoring fields. Many system identification techniques have been developed and applied to detect

unpredictable structural damage during seismic events or in service life. Recent review literatures related to system identification and structural health monitoring techniques include Kerschen et al. [1], Adams [2], Worden [3], Takewaki et al. [4], and Farrar and Worden [5].

Local damage quantification using vibration-based identification methods for building structures is technically challenging since (i) the damage effect usually involves *nonlinear* behavior of structures, and (ii) damage quantification is significantly affected by the *boundary conditions* of the superstructure-foundation-soil interaction (SFSI). Many system identification techniques, however, are based on the limited assumptions on (i) system linearity (i.e., structural behaviors usually become nonlinear under extreme excitation or damage), (ii) excitation forces (e.g., Gaussian white stationary excitation), and (iii) global dynamic characteristics rather than local characteristics for damage localization (e.g., modal parameters based on global stiffness and damping matrices), which are not realistic in many field applications.

In this study, the dynamic characteristics of complex soil-foundation-superstructure (SFS) systems are identified to investigate the nonlinear effects of localized damage on realistic building-like (or chain-like) systems subjected to various seismic excitations. To achieve this research goal, analytical study is conducted using an extensive series of shake table test datasets, which were collected at Tongji University, China [6-8] with 1:10 scaled, 12-story reinforced concrete frames with different boundary conditions of fixed, pile and box foundations. The Multi-degree-of-freedom Restoring Force Method (MRFM) [9] is used as a non-parametric identification method to *quantify*, *characterize*, and *localize* the



effects of localized damage on dynamic response of the above realistic soil-foundation-superstructure systems.

This paper will be outlined as follows: the experimental studies of the SFS system with the fixed, pile and box foundations are shown in Section 2; the system identification results using MRFM as a nonlinear localized system identification method are shown in Section 3; the quantification of the localized interstory damage using MRFM is presented in Section 4; finally the conclusions are followed in Section 5.

### **3.3 Large-Scale Shake Table Tests**

#### **3.3.1 Test Setup**

To investigate building foundation effects on nonlinear system identification, three identical reinforced cast-in-place concrete frame models were fabricated in the State Key Laboratory at Tongji University, Shanghai, China. The fabricated concrete frames were 12-story building models in 1:10 scale. Then the fabricated models were placed on three different foundation types including pile, box and fixed foundations (Figure 2.1).

The building models with the pile and box foundations were placed on three layers of soil with silty clay, powder sand soil and sandy soil. To reduce the “box-effect” of the soil container, the soil was contained in a flexible cylindrical container with a 3000-mm diameter and a 5-mm flexible rubber membrane. A top plate with a large diameter hole held the flexible rubber membrane and was supported by four columns fixed to the base plate. Reinforcement with a stack of steel loops was added to the outside of the container to provide radial rigidity and at the same time to allow the soil to have shear deformation

in the horizontal direction. Crushed rocks were epoxied to the floor of the container to prevent the soil from slipping.

Then the pile and box foundation models with the flexible soil container were placed on a large-scale shake table. The 4.0 m × 4.0 m shake table has the maximum capacity of 25 tons and can be operated at the maximum acceleration of 1.2g in x-direction. The base plate of the soil container was rigidly bolted to the shake table. The fixed foundation model was not placed on the soil container and was directly bolted to the shake table.

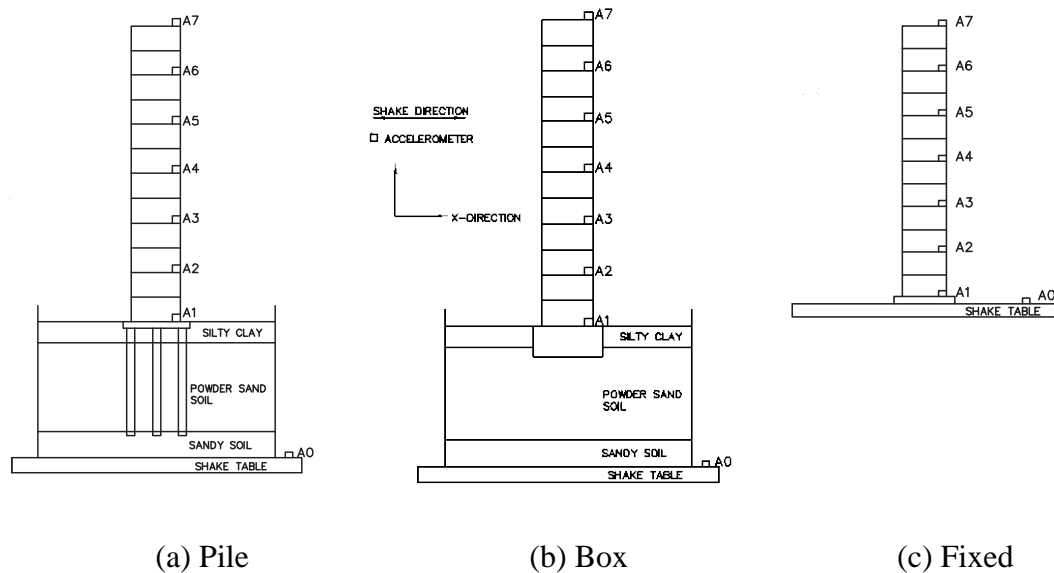


Figure 3.1: Large-scale reinforced cast-in-place concrete frame models placed on three different foundation types tested on a shake table, and the accelerometer locations installed on the shake table and the superstructures (A0 to A7). The measurement direction for all accelerometers is in x-direction.

A photo of the soil-foundation-superstructure (SFS) test setup is shown in Figure 3.2. Properties and dimensions of the superstructure, foundations and soil of the models are summarized in Table 3.1.

Table 3.1: Properties and dimensions of the superstructure, foundation and soil of the tested building models.

Superstructures	Pile foundation	Box foundation	Soil
<ul style="list-style-type: none"> <li>• Model scale: 1:10</li> <li>• Floor number: 12</li> <li>• Floor height: 300 mm</li> <li>• Total height: 3600 mm</li> <li>• Column net spacing: 600 mm × 600 mm</li> <li>• Beam cross-section: 30 mm × 60 mm</li> <li>• Column cross-section: 50 mm × 60 mm</li> <li>• Floor slab thickness: 12 mm</li> </ul>	<ul style="list-style-type: none"> <li>• Pile number: 9</li> <li>• Pile length: 1200 mm</li> <li>• Pile cross-section: 45 mm × 45 mm</li> </ul>	<ul style="list-style-type: none"> <li>• Box size: 650 mm × 650 mm</li> </ul>	<ul style="list-style-type: none"> <li>• Soil layer type: silty clay, powder sand soil, sandy soil</li> <li>• Total soil height: 1600 mm</li> </ul>



(a) A large-scale building model placed on soil foundation



(b) Three identical reinforced cast-in-place building models tested in this study (two models are shown)

Figure 3.2: A photo of the large-scale soil-foundation-superstructure test setup (note that the size of the experimental setup is compared with the size of a test operator). [6-8]

The building superstructures were instrumented with seven accelerometers at every two floors from the building base (A1 to A7) to measure the dynamic response of the building. An additional accelerometer was installed on the shake table (A0). Therefore, the acceleration measured at A1 was the ground motion, and the acceleration measured at A0 was the original input acceleration to the SFS models. The accelerations were sampled at 250 Hz for all sensor channels.

### 3.3.2 Test Protocol

A series of shake table tests was conducted for three different earthquake types with seven different excitation magnitude levels for the building models with three foundation types. Four types of excitation were tested including El Centro earthquake (EL), Kobe earthquake (KB), Shanghai artificial wave (SH), and Gaussian white wave (GW). Seven levels of excitation were used in x-direction or xz-directions with the shaker's peak acceleration from 0.093 G to 0.532 G (or Levels 1 to 7) for EL, KB and SH. The peak accelerations were determined considering the gravity deformation effects using the Buckingham Pi Theorem. The control tests were conducted using GW for the shaker's peak acceleration of 0.07 G for all cases (i.e., 1GW, 10GW, 16GW, 22GW, 28GW, 34GW and 40GW) before and after tests at each excitation level of EL, KB and SH. The above test protocols are summarized in Table 3.2.

As shown in the table, the level of excitation increased from low peak acceleration to high peak acceleration gradually for each foundation type. Therefore, damage in the superstructure, foundation and soil were accumulated as the experiments for each foundation type were being conducted. It should be noted that Tests 35-40 could not be conducted for the fixed foundation due to the superstructure failure during the tests, while all 40 tests were conducted for the pile and box foundations. The effects of the accumulated damage in the SFS systems will be quantified and discussed in Section 4.

Table 3.2: Test protocols with different earthquake excitation waves for the building models with the fixed, pile and box foundations. EL: El Centro wave, SH: Shanghai artificial wave, KB: Kobe wave, and GW: Gaussian white wave.

Test No.	Excitation Type	Peak Acc. (G)		Test No.	Excitation Type	Peak Acc. (G)	
		X	Z			X	Z
1	1GW	0.07	-	22	22GW	0.07	-
2, 3, 4	EL1, SH1, KB1	0.093	-	23, 24, 25	EL5, SH5, KB5	0.665	-
5, 6, 7	EL2, SH2, KB2	0.266	-	26, 27	ELZ5, KBZ5	0.665	0.53
8, 9	ELZ2, KBZ2	0.266	0.266	28	28GW	0.07	-
10	10GW	0.07	-	29, 30, 31	EL6, SH6, KB6	0.798	-
11, 12, 13	EL3, SH3, KB3	0.399	-	32, 33	ELZ6, KBZ6	0.798	0.53
14, 15	ELZ3, KBZ3	0.399	0.399	34	34GW	0.07	-
16	16GW	0.07	-	35, 36, 37	EL7, SH7, KB7	0.931	-

Once the acceleration datasets were measured at the shake table and the super structure, they were preprocessed to obtain the corresponding velocity and displacement. First, the acceleration was detrended using up to the 6th order polynomials, and then lowpass filtered using a zero-phase distortion filter with the passband of 110 Hz, the stopband of 120 Hz, the passband ripple of 1 dB, and stopband attenuation of 60 dB. After the detrending and lowpass-filtering, the preprocessed acceleration was numerically integrated to obtain the corresponding velocity and displacement. After numerical integration for velocity and displacement, the same detrending and lowpass-filtering procedures were applied. Sample earthquake time histories of the acceleration, velocity and displacement are shown in Figure 3.3. The obtained velocity and displacement datasets will be used in the nonlinear system identification with the multi-degree-of-freedom Restoring Force Method that will be described in Section 3.

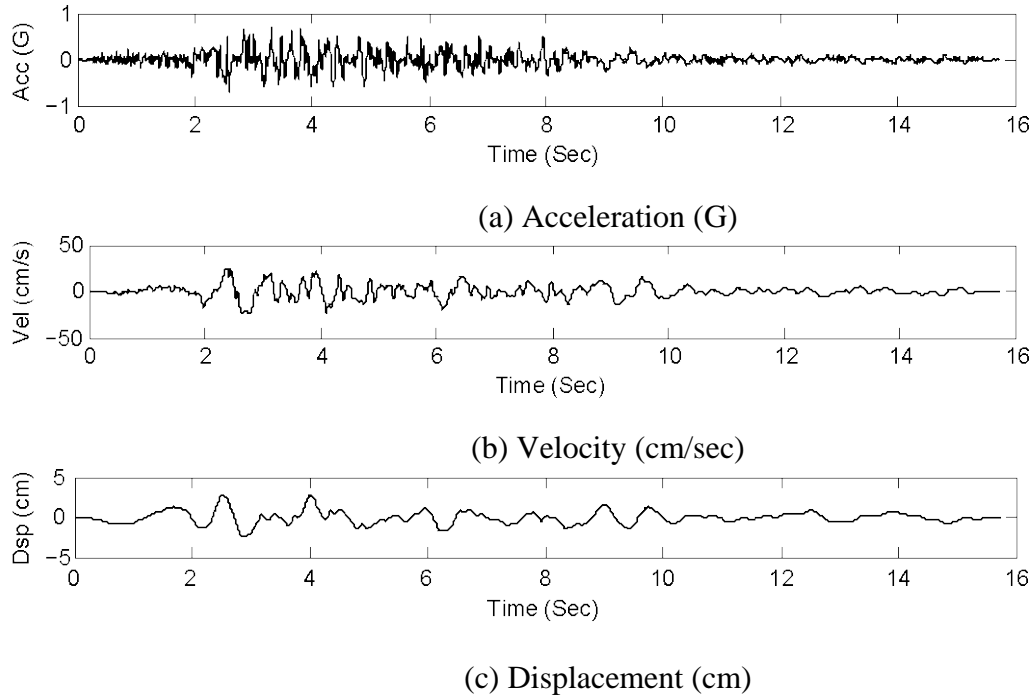


Figure 3.3: Shake table motions of the acceleration, velocity and displacement time histories for the Shanghai artificial wave at Level 6.

### **3.4 Nonlinear Identification for Chain-like Systems**

In this section, nonlinear identification results using the Restoring Force Method are presented. Section 3.1 shows mathematical background of the multi-degree-of-freedom Restoring Force Method.

#### **3.4.1 MDOF Restoring Force Method**

The multi-degree-of-freedom Restoring Force Method (MRFM) was originally developed by Masri et al. [9] as an extension of the single-degree-of-freedom Restoring Force Method (SRFM) by Masri and Caughey [10]. Nayeri et al. [11] applied MRFM to identify a full-scale 17-story building subjected to ambient excitation.

A multi-degree-of-freedom (MDOF) chain-like system with nonlinear restoring forces,  $G_k(x, \dot{x})$ , is illustrated in Figure 3.4. The relative displacement and velocity between two consecutive masses can be expressed as

$$z_k = x_k - x_{k-1}, \quad \dot{z}_k = \dot{x}_k - \dot{x}_{k-1} \quad (3.1)$$

where  $x_k$  and  $\dot{x}_k$  are absolute displacement and velocity of  $k$ -th mass, respectively. In the same manner, the relative displacement and velocity of the first mass are

$$z_1 = x_1 - s, \quad \dot{z}_1 = \dot{x}_1 - \dot{s} \quad (3.2)$$

where  $s$  and  $\dot{s}$  are ground displacement and velocity, respectively. Consequently, the equations of motion for the chain-like system are

$$\begin{aligned} m_n \ddot{x}_n + G_n(z_n, \dot{z}_n) &= F_n(t) \\ m_{n-1} \ddot{x}_{n-1} + G_{n-1}(z_{n-1}, \dot{z}_{n-1}) &= G_n(z_n, \dot{z}_n) + F_{n-1}(t) \\ &\vdots \\ m_2 \ddot{x}_2 + G_2(z_2, \dot{z}_2) &= G_3(z_3, \dot{z}_3) + F_2(t) \\ m_1 \ddot{x}_1 + G_1(z_1, \dot{z}_1) &= G_2(z_2, \dot{z}_2) + F_1(t) \end{aligned} \quad (3.3)$$

Equation 3.3 can be rewritten for the restoring forces as

$$\begin{aligned} G_n(z_n, \dot{z}_n) &= -m_n \ddot{x}_n + F_n(t) \\ G_{n-1}(z_{n-1}, \dot{z}_{n-1}) &= -m_{n-1} \ddot{x}_{n-1} + G_n(z_n, \dot{z}_n) + F_{n-1}(t) \\ &\vdots \\ G_2(z_2, \dot{z}_2) &= -m_2 \ddot{x}_2 + G_3(z_3, \dot{z}_3) + F_2(t) \\ G_1(z_1, \dot{z}_1) &= -m_1 \ddot{x}_1 + G_2(z_2, \dot{z}_2) + F_1(t) \end{aligned} \quad (3.4)$$

Therefore, the nonlinear restoring forces of the chain-like system can be determined consecutively from the top (i.e.,  $G_n$ ) by measuring the force and the acceleration of each



mass. The restoring forces induced by the ground motion only (i.e., the forces on the masses are zero) can be normalized by their masses as

$$\begin{aligned}
\frac{G_n(z_n, \dot{z}_n)}{m_n} &= -\ddot{x}_n \\
\frac{G_{n-1}(z_{n-1}, \dot{z}_{n-1})}{m_{n-1}} &= -\ddot{x}_{n-1} + \frac{G_n(z_n, \dot{z}_n)}{m_{n-1}} \\
&\vdots \\
\frac{G_2(z_2, \dot{z}_2)}{m_2} &= -\ddot{x}_2 + \frac{G_3(z_3, \dot{z}_3)}{m_2} \\
\frac{G_1(z_1, \dot{z}_1)}{m_1} &= -\ddot{x}_1 + \frac{G_2(z_2, \dot{z}_2)}{m_1}
\end{aligned} \tag{3.5}$$

The advantage of using the mass-normalized restoring force is that the absolute value of the lumped mass of each element, which is not often available, is not necessarily known.

Let  $\frac{G_k(z_k, \dot{z}_k)}{m_k} = G_k^m$ , then the mass-normalized restoring force can be estimated with a series of two-dimensional Chebyshev polynomials and power-series polynomials of the  $k$ -th element as

$$G_k^m \approx \hat{G}_k^m = \sum_{i=0}^p \sum_{j=0}^q C_{ij}^m T_i(\bar{z}_k) T_j(\bar{\dot{z}}_k) = \sum_{i=0}^p \sum_{j=0}^q a_{ij}^m z_k^i \dot{z}_k^j \tag{3.6}$$

where  $C_{ij}^m$  and  $a_{ij}^m$  are the mass-normalized Chebyshev and power series coefficients, respectively;  $T_i$  is the  $i$ -th order of Chebyshev polynomial; and  $\bar{z}_k$  and  $\bar{\dot{z}}_k$  are the normalized relative displacement and velocity over the range of  $[-1, 1]$  as

$$\bar{z}_k = \frac{z_k - (z_{\max} + z_{\min})/2}{(z_{\max} - z_{\min})/2}, \quad \bar{\dot{z}}_k = \frac{\dot{z}_k - (\dot{z}_{\max} + \dot{z}_{\min})/2}{(\dot{z}_{\max} - \dot{z}_{\min})/2} \tag{3.7}$$

in which  $z_{\max}$  ( $\dot{z}_{\max}$ ) and  $z_{\min}$  ( $\dot{z}_{\min}$ ) are the maximum and minimum values of  $z_k$  ( $\dot{z}_k$ ), respectively.

Finally, the mass-normalized nonlinear restoring force of each mass,  $G_k^m$ , can be identified by determining the Chebyshev coefficients,  $C_{ij}^m$  using  $z_k$  and  $\dot{z}_k$ . Detailed procedures to determine  $C_{ij}^m$  can be found in Masri and Caughey. [10]

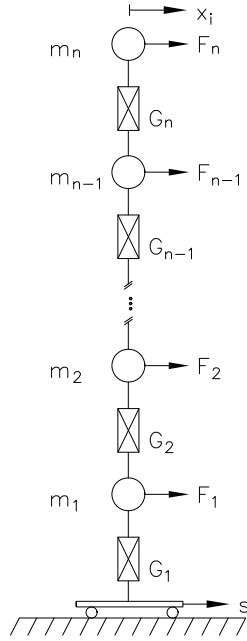


Figure 3.4: A schematic of a multi-degree-of-freedom chain-like system with nonlinear restoring forces.

It should be also noted that the power-series coefficients in Equation 3.6 can be obtained from the Chebyshev coefficients using the following relationships:

$$T_{n+1}(x) = 2xT_n(x) - T_{n-1}(x) \quad (3.8)$$

where  $T_0(x) = 1$ ,  $T_1(x) = x$ ,  $T_2(x) = 2x^2 - 1$ , ... The advantage of using the Chebyshev coefficients is that since their basis functions are orthogonal over the range of  $[-1, 1]$ , the identification of the Chebyshev coefficients is statistically unbiased. On the other hand,

the advantage of using the power-series coefficients is that interpreting physical meaning of the identified coefficients is straightforward (e.g.,  $a_{10}^m$  is the linear spring constant normalized to its mass, and  $a_{01}^m$  is the linear damping constant normalized to its mass). A comparison between the Chebyshev and power-series coefficients through an extensive stochastic experimental study using nonlinear magneto-rheological dampers was given in Yun and Masri. [12-13]

### **3.4.2 Determination of Nonlinear Interstory Restoring Forces**

The mass-normalized interstory restoring forces were determined using Equation 3.5, and sample measured interstory restoring force time histories are shown in Figure 3.5 as solid lines. The amplitudes of the mass-normalized restoring force ( $G_k^m$ ) are greater on lower floors than upper floors due to the ground motion at the bottom of the superstructure frame model. It should be noted that, however, the time history shape of the determined interstory restoring force remains similar from  $G_6^m$  to  $G_1^m$  since the interstory dynamic characteristics of the superstructure model should be similar each other with the same materials and dimensions of each building floor used in the model fabrication.

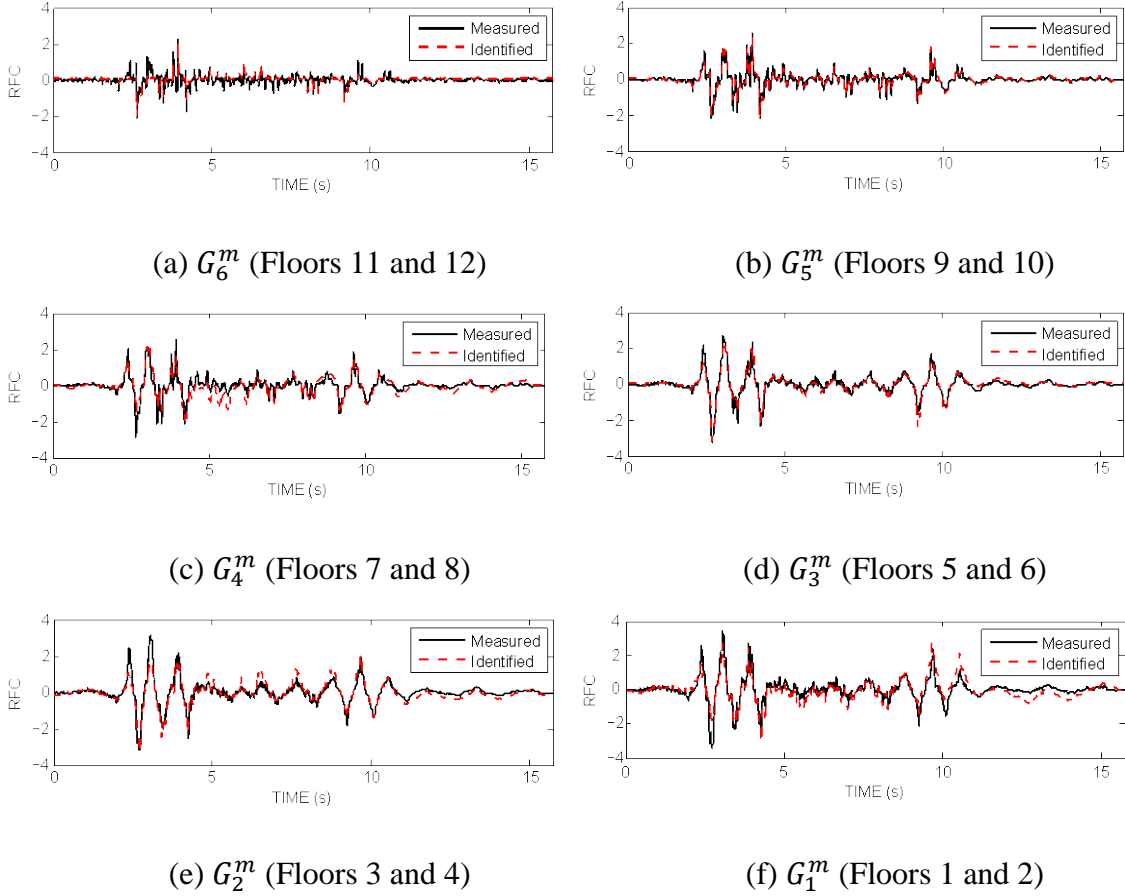


Figure 3.5: Measured and identified *time histories of the interstory mass-normalized restoring force* ( $G_k^m$ ) for the fixed foundation subjected to the Shanghai artificial earthquake excitation at Level 6. The restoring forces are shown from the top story.

Once the interstory mass-normalized restoring forces were obtained, the interstory stiffness phase diagrams were plotted for the displacement ( $x_k$ ) and the mass-normalized restoring force ( $G_k^m$ ) as shown in the *solid lines* in Figure 3.6. The stiffness phase diagrams are constructed using the dataset of the superstructure with the fixed foundation subjected to the Shanghai artificial wave excitation at Level 6 (peak acceleration of 0.768 G).

Therefore, as described in Section 2.2, structural damage in the superstructure had been accumulated that was induced by increasing levels of excitation in Tests 1-30 in Table 3.2.

The stiffness phase diagrams show the significant nonlinearity with *stiffness hardening* on all floors when the displacement is large. It can be also observed that the *linear stiffness* decreases on lower floors. In addition, the lower floor restoring forces have significantly larger *hysteresis* than those on the upper floors. The larger hysteresis indicates more dissipated energy due to the damage of the reinforced concrete model during the seismic excitation. Consequently, it can be postulated that the reduced stiffness and increased hysteresis on lower floors are due to the accumulated damage since the superstructure was shaken from the bottom.

The interstory damping phase diagrams are also plotted for the velocity ( $\dot{x}_k$ ) and the mass-normalized restoring force ( $G_k^m$ ) shown as the *solid lines* in Figure 3.7. The damping phase diagrams show that the interstory restoring forces have a little effect of damping, which is reasonable for the brittle reinforced cast-in-place concrete frame models.

Therefore, the localized nonlinear damage effects on the superstructure can be evaluated *qualitatively* from the stiffness and damping phase diagrams. Section 3.3 presents how the localized nonlinear damage effects can be evaluated *quantitatively* using MRFM.

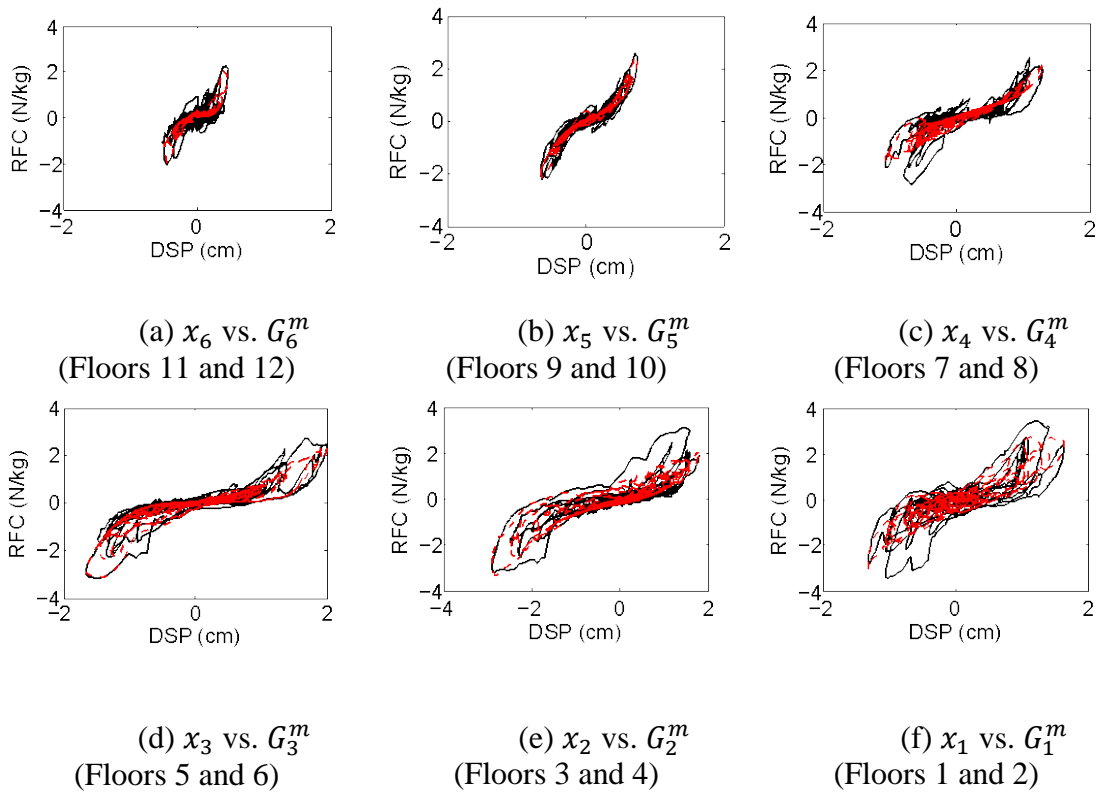


Figure 3.6: Measured and identified *interstory phase plots of the displacement ( $x_k$ ) and the mass-normalized restoring force ( $G_k^m$ )* for the fixed foundation subjected to the Shanghai artificial wave excitation at Level 6. The measured data are shown in the solid line, and the identified data are shown in the dashed line. The phase plots are shown from the top story.

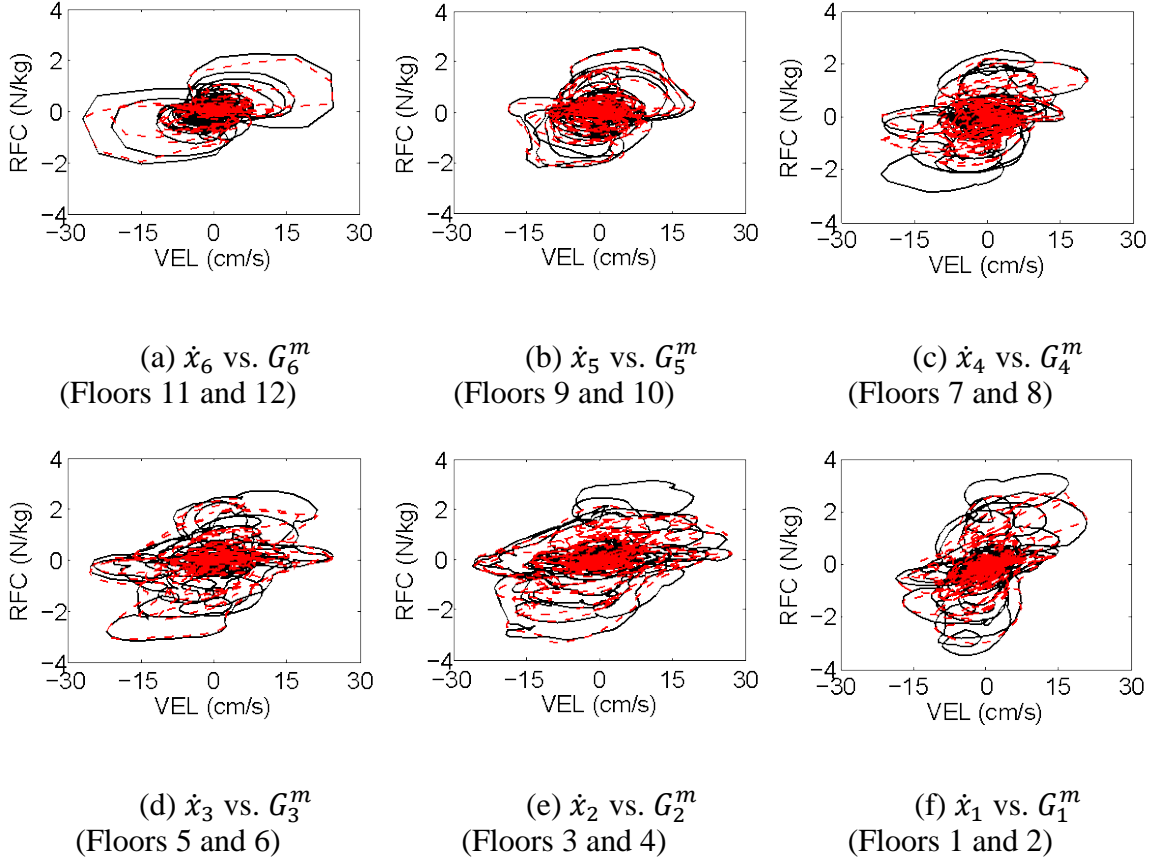


Figure 3.7: Measured and identified *interstory phase plots of the velocity* ( $\dot{x}_k$ ) *and the mass-normalized restoring force* ( $G_k^m$ ) for the fixed foundation subjected to the Shanghai artificial earthquake excitation at Level 6. The measured data are shown in the solid line, and the identified data are shown in the dashed line. The phase plots are shown from the top floor.

### 3.4.3 Surface Fitting for Scattered Data in 3-D Restoring Force Phase Domain

Once the mass-normalized restoring forces were determined in Section 3.2, MRFM was used to identify the nonlinear restoring forces. To determine the proper model order of MRFM, the normalized mean square error was calculated for different model orders as

$$\text{NMSE}(\hat{x})(\%) = \frac{100}{N\sigma_x^2} \sum_{i=1}^N (x_i - \hat{x}_i)^2 \quad (3.9)$$

where  $x$  is the measured data, in this case the mass-normalized restoring force ( $G_k^m$ ), and  $\hat{x}$  is the identified restoring force data using MRFM. The error analysis results showed that NMSE becomes saturated after the 4th order for all foundation types. Therefore, the model order of 4 was used in MRFM analysis for all cases. The averaged NMSE for all excitation levels using SH datasets was 33.60% for the fixed foundation; 61.69% for the box foundation; and 24.70% for the pile foundation. Sample identified interstory restoring forces are shown in Figure 3.5 as the *dashed lines*.

In MRFM analysis, the scattered triplet data ( $\bar{x}_k, \dot{\bar{x}}_k, G_k^m$ ) of each floor should be first fitted to obtain the corresponding restoring force surface with equally spaced grids in  $\bar{x}_k$  and  $\dot{\bar{x}}_k$ . It should be noted that Masri and Caughey in their original paper [10] suggested a surface regression scheme to obtain a three-dimensional restoring force surface in the displacement, velocity and restoring force domain assuming that

$$G(z, \dot{z}) \approx \sum_{i=0}^p a_i T_i(\bar{z}) + \sum_{j=0}^q b_j T_j(\dot{\bar{z}}) \quad (3.10)$$

where  $a_i$  and  $b_j$  can be calculated from  $G(z, 0) \approx \sum_{i=0}^p a_i T_i(\bar{z})$  and  $G(0, \dot{z}) \approx \sum_{j=0}^q b_j T_j(\dot{\bar{z}})$ . With this assumption, however, the extrapolated portion of the restoring surface near  $(\bar{z}, \dot{\bar{z}}) = (\pm 1, \pm 1)$  and  $(\pm 1, \mp 1)$  could be inaccurate when the coupled terms of displacement and velocity for the restoring force are significant:  $C_{ij}^m \neq 0$  where  $i \neq 0$  and  $j \neq 0$ . To address this inaccuracy problem of the restoring force surface extrapolation, Worden and Tomlinson [14] suggested using only the interpolated portion of the restoring



force surface by removing data near  $(\bar{z}, \bar{\dot{z}}) = (\pm 1, 0)$  and  $(\bar{z}, \bar{\dot{z}}) = (0, \pm 1)$ . Removing the large magnitude data of  $\bar{z}$  and  $\bar{\dot{z}}$  in the Worden and Tomlinson's approach, however, is not desirable for the nonlinear system, whose nonlinearity is significant for large displacement or velocity, such as stiffness (or damping) softening or hardening. Therefore, the Radial Basis Function (RBF) interpolation and approximation code developed by Chirokov [15] is used in this study to fit the restoring force surface using Gaussian bases as

$$G(\bar{z}, \bar{\dot{z}}) \approx \sum_{i=1}^N \lambda_i \phi^i(\bar{z}, \bar{\dot{z}}) \quad (3.11)$$

where  $\phi(r) = \exp(-(\epsilon r)^2)$ ;  $r = \|\mathbf{z} - \mathbf{z}_c\|$  is the Euclidean distance of the scattered data  $\mathbf{z}$  from the center  $\mathbf{z}_c$ ;  $\epsilon$  is the weight of RBF; and  $N$  is the highest order of RBFs. Advantages of using the RBF regression include: (i) it is a mesh-free interpolation which means that there is no restriction for the geometry of known data points; (ii) the end product from the interpolation is a smooth single-valued function; (iii) RBFs are suited to interpolate scattered data, even when those data contains large dataless areas because of their variational characterization. Figure 3.8 shows the three-dimensional mass-normalized interstory restoring force ( $G_k^m$ ) surface using the RBF interpolation for the normalized displacement ( $\bar{z}_k$ ) and velocity ( $\bar{\dot{z}}_k$ ) with the range over [-1, 1].

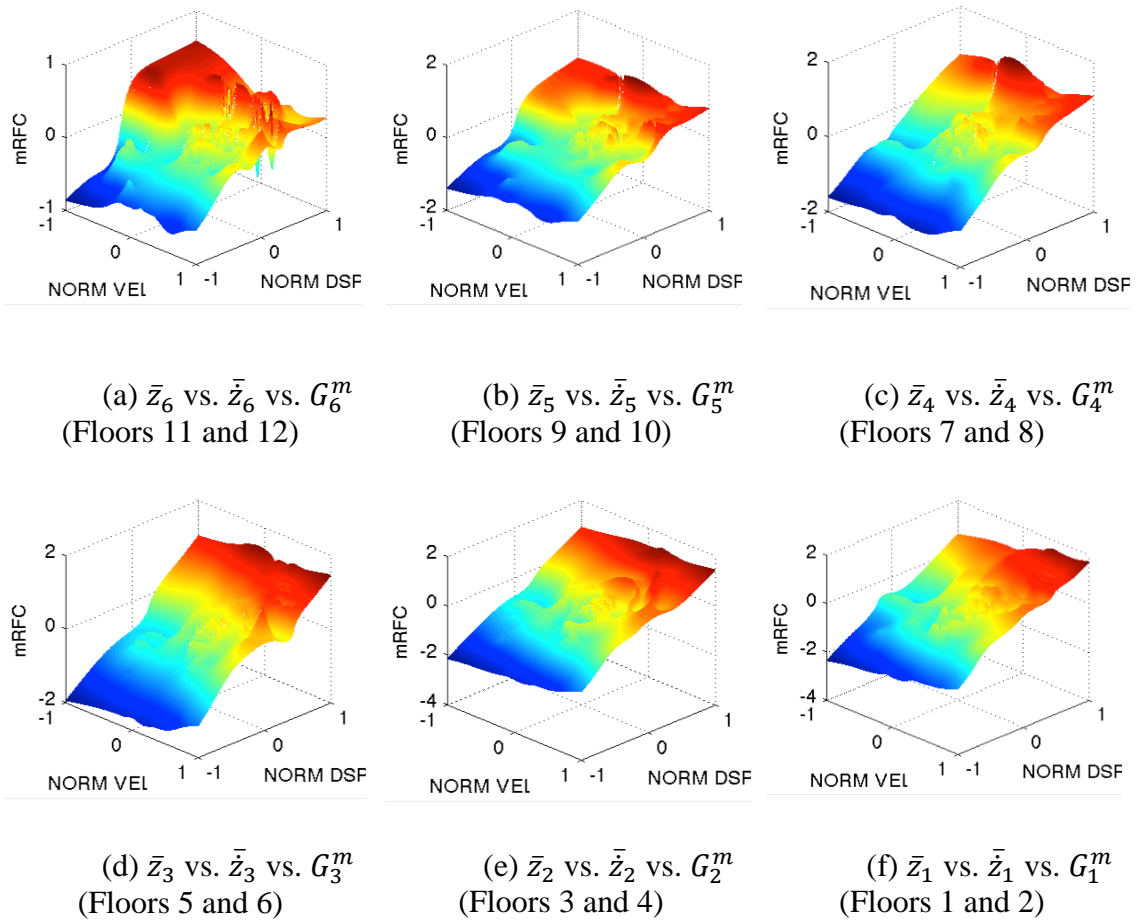


Figure 3.8: Three-dimensional interstory restoring phase surfaces fitted using the Radial Bases Functions for the superstructure with the fixed foundation subjected to the Shanghai artificial earthquake excitation at Level 6. The normalized displacement and velocity with the range over  $[-1 \ 1]$  are shown in x- and y-axis, respectively, and the mass-normalized restoring force is shown in z-axis.

### 3.4.4 Term-wise Identification Using MRFM

Once the mass-normalized interstory restoring force surfaces were fitted, MRFM were used to identify the Chebyshev coefficients. Sample identification results for the mass-normalized interstory restoring forces are shown in Figures 3.6 and 3.7 as *dashed lines*, and the corresponding Chebyshev coefficients are shown in Figure 3.9. The x- and

y-axis in Figure 3.9 indicate the order of the Chebyshev polynomials (i.e.,  $i$  and  $j$ , respectively) in Equation 3.6. The identification results showed that the first-order stiffness term ( $C_{10}^m$ ) had dominant contribution for all test cases. The power-series coefficients were converted from the Chebyshev coefficients using Equation 3.8, and the corresponding set of the power-series coefficients converted from the Chebyshev coefficients in Figure 3.9 are shown in Figure 3.10.

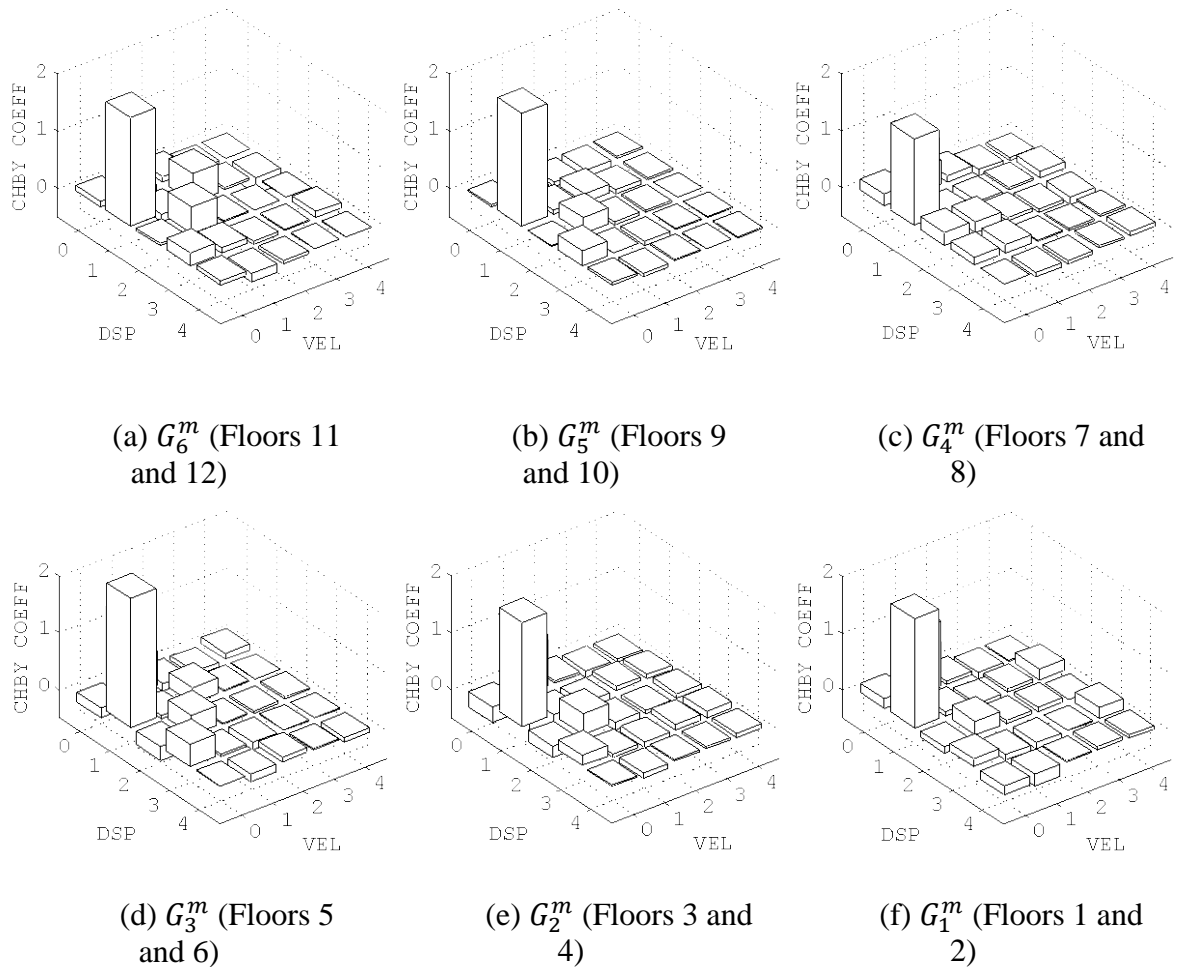


Figure 3.9: Identified Chebyshev coefficients for the superstructure with the fixed foundation subjected to the Shanghai artificial excitation at Level 6.

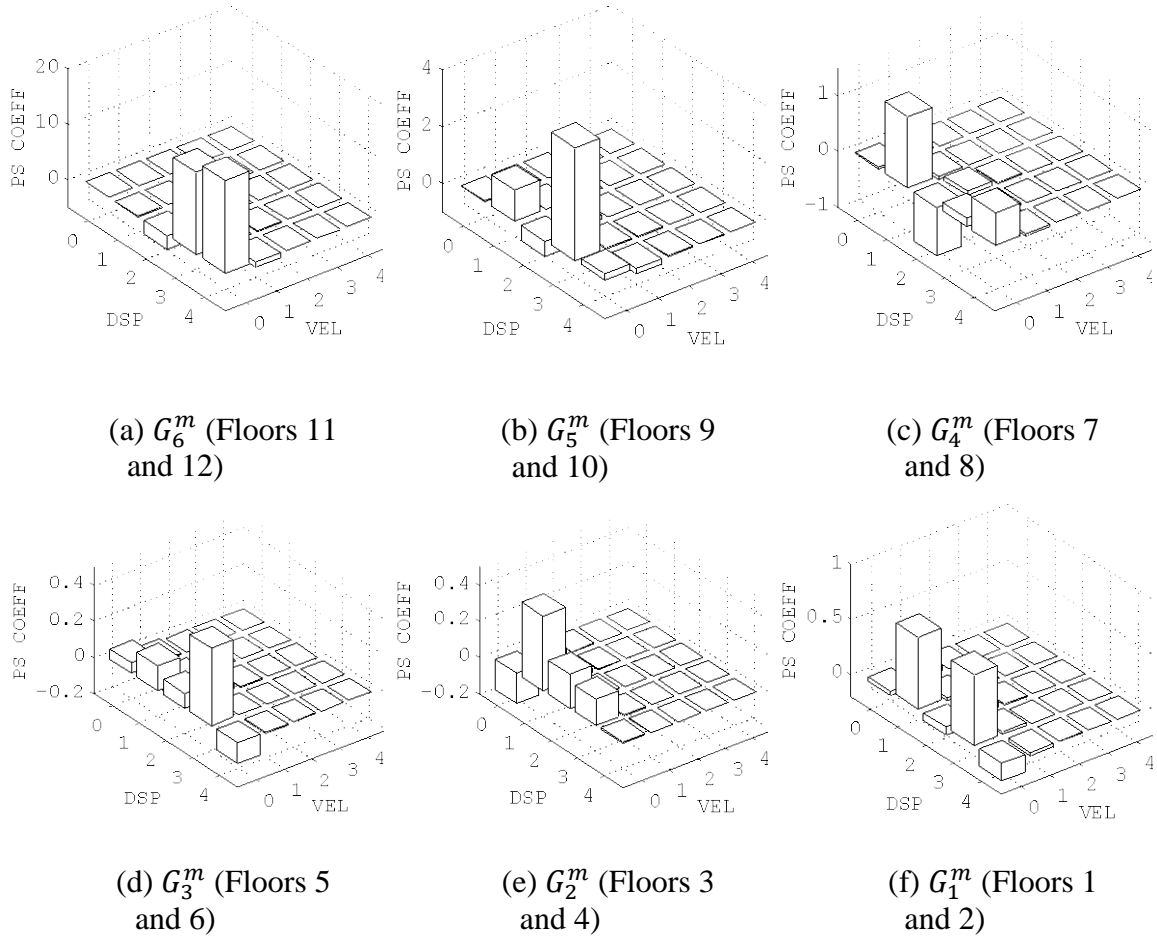


Figure 3.10: Power-series coefficients converted from the Chebyshev coefficients in Figure 9 for the superstructure with the fixed foundation subjected to the Shanghai artificial excitation at Level 6.

Figure 3.11 compares three dominant term-wise identification results of the linear stiffness, cubic stiffness and linear damping using the identified Chebyshev and power-series coefficients that were shown in Figures 3.9 and 3.10. The measured data are shown in the solid lines, and the term-wise identified data are shown in the dashed lines. It can be found that the stiffness-related Chebyshev coefficients,  $C_{10}^m$  and  $C_{30}^m$ , have contribution to the displacement-dependent behavior of the mass-normalized restoring force that

absorbs seismic energy to the superstructure (Figures 3.11a and 3.11b), and the damping-related Chebyshev coefficient,  $C_{01}^m$ , has contribution to the velocity-dependent behavior of the mass-normalized restoring force that dissipates seismic energy from the superstructure (Figure 3.11c). The Chebyshev coefficients are advantageous with statistical unbiasedness in the identification due to their orthogonal basis functions.

The power-series coefficients, on the other hand, have more straightforward physical meanings than the Chebyshev coefficients:  $a_{10}^m$ ,  $a_{30}^m$  and  $a_{01}^m$ , are equivalent to the linear stiffness constant (Figure 3.11d), the cubic stiffness constant (Figure 3.11e) and the linear damping constant (Figure 3.11e) for the mass-normalized restoring force, respectively. The identification of the power-series coefficients, however, could be statistically biased since the power-series polynomial basis functions are not orthogonal. A comparison of the stochastic characteristics between the Chebyshev and power-series identification was presented through an extensive experimental and analytical study using nonlinear magneto-rheological dampers in Yun and Masri. [12-13]

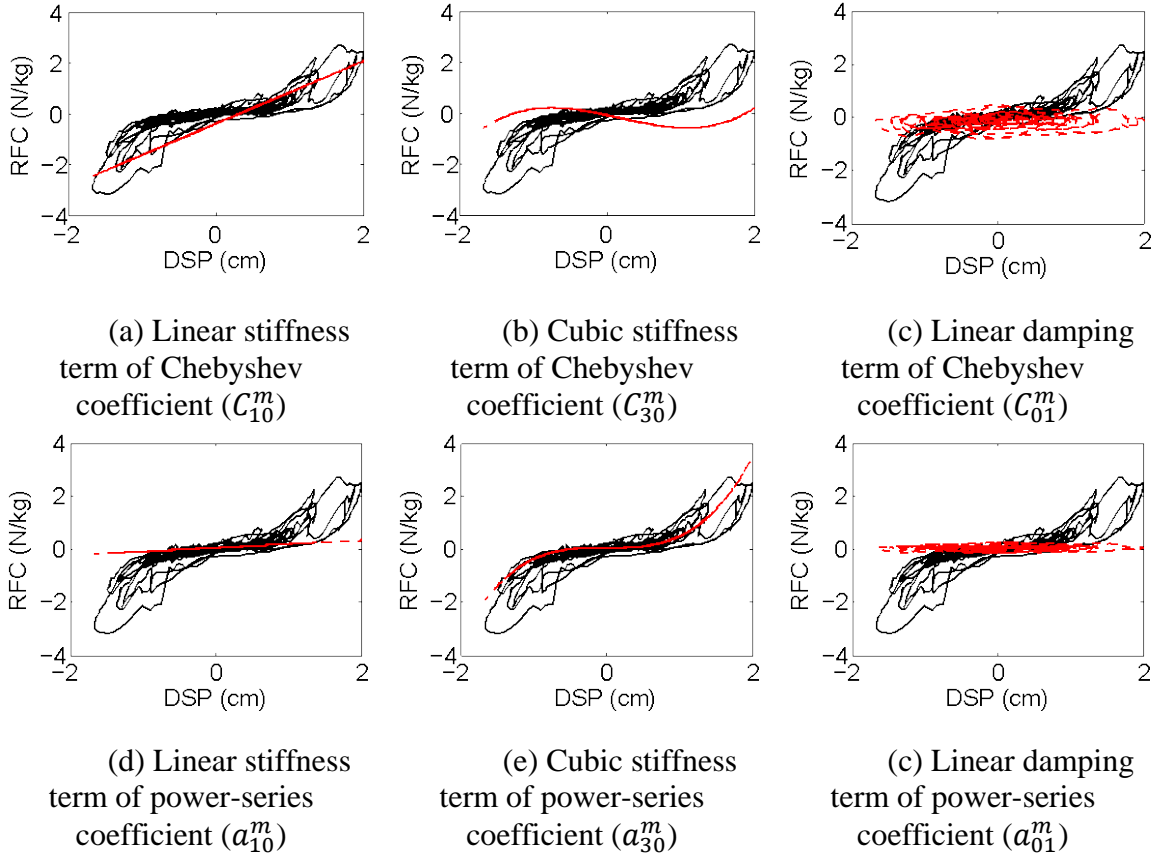


Figure 3.11: Term-wise identification results for the mass-normalized interstory restoring force,  $G_3^m$  (Floors 5 and 6), of the superstructure with the fixed foundation subjected to the Shanghai artificial excitation at Level 6: (a)-(c) for the Chebyshev power-series coefficients; (d)-(f) for the power-series coefficients. The measured data are shown in the solid line, and the term-wise identified data are shown in the dashed line.

### **3.5 Quantification of Localized Interstory Damage**

After the soil-foundation-superstructure (SFS) systems were identified using MRFM, localized interstory damage was quantified, and compared with visual inspection results during or after the shaker tests were conducted. The visual inspection results of the SFS systems are described in Section 4.1; the quantification of localized interstory damage

is discussed in Section 4.2; the mode shapes determined using MRFM are compared with the mode shapes using classical modal analysis in Section 4.3.

### **3.5.1 Visual Inspection of Damage in the Soil-Foundation-Superstructure Systems**

The damage in the SFS systems was accumulated as the shaker tests were conducted using the earthquake waves with increasing peak accelerations as described in Table 3.2. The severeness of damage in the SFS systems was visually inspected during and after the shaker tests. The visual inspection results on the damage in the SFS systems with the fixed, pile and box foundations are summarized in Sections 4.1.1 to 4.1.3, respectively.

#### *3.5.1.1 Fixed foundation*

**Superstructure:** The shake table tests were conducted until the superstructure failed. No cracks were observed on the superstructure during the first 8 shaker tests. After Test 9 (Excitation Lv. 2 with the peak acceleration of 0.266 G), fine vertical cracks with the width of less than 0.05 mm were found on the beams along x-direction (i.e., the shaker vibration direction) on Floors 1 to 4. There were no cracks found on the columns at these excitation levels. After Test 10 (Excitation Lv. 2 with the peak acceleration of 0.093 G), vertical cracks with the width of less than 0.1 mm were found on the beams close to the connected columns on Floors 1 to 5. After Test 22 (Excitation Lv. 4 with the peak acceleration of 0.532 G), vertical crack width increased to about 0.5 mm on the beams on Floors 3 and 4. Cracks were also observed on the columns on Floor 1, and the upper part of a concrete column on Floor 3 crushed. It was observed that those cracks were

continuously developed as the excitation level increased. After Test 34 (Excitation Lv. 6 with the peak acceleration of 0.798 G), horizontal cracks were observed on the columns: the cracks with the width of 0.2 mm ~ 0.5 mm were on the bottom outer side of the columns on Floors 1 to 3, and concrete crushed on the upper outer side of some columns on Floors 2 and 3. Vertical cracks with the width of 0.1 mm ~ 1.0 mm were also observed on the beams on Floors 1 to 8, and the cracks on Floors 2 to 5 were wider than the cracks on the other floors. Most cracks were found along x-direction, and a few cracks were also found in y-direction (i.e., perpendicular to the shaker direction).

#### *3.5.1.2 Pile foundation*

**Settlement:** For the pile foundation, the SFS system was settled evenly during the first 22 tests in Table 3.2, and uneven settlement was observed with higher peak acceleration tests. The final settlement of the pile foundation plate was measured at 10.7 cm at the northwest corner, 9.5 cm at the northeast corner, 9.7 cm at the southwest corner, and 7.6 cm at the southeast corner, which resulted in the inclination of the superstructure at 1/48 northward and at 1/42 westward.

**Superstructure:** During the first 26 tests for the pile foundation, no cracks were observed in the superstructure. After Test 27 (Excitation Lv. 5 with the peak acceleration of 0.665G), fine cracks with the width of less than 0.02 mm were observed on the bottom of the northeast corner column on Floor 1, the beams along x-direction on Floors 1 and 2. After the shaker tests were completed, thick cracks of about 0.5 mm were observed on the



bottom of the four columns on Floor 1, and some fine vertical cracks were observed on the beams on from Floors 1 to 6 along x-direction. Compared to the superstructure with the fixed foundation, the cracks with the pile foundation were developed slowly and small in terms of their counts and sizes.

**Pile foundation:** After the shaker tests, the pile foundation was taken out from the soil container, and the crack patterns on the piles were inspected. Figure 3.12 illustrates the pile layout and visual inspection results of the crack patterns on the piles after the shaker tests. The wider and denser cracks were found near the junctions of the pile cap and the piles than near the pile tips. Relatively a smaller number of cracks were found on the middle piles (i.e., piles 4, 5 and 6). The crack directions were mostly horizontal, which indicated that they were bending cracks.

#### *3.5.1.3 Box foundation*

**Settlement:** The settlement of the SFS system with the box foundation was observed after Test 15 (Excitation Lv. 3 with the peak acceleration of 0.399 G). The superstructure inclined northward about 1%. It was observed that the settlement and inclination increased as the excitation level increased. The final settlement was observed at about 6.5 cm with the superstructure inclination of about 5.6% westward and about 0.6% northward.

**Superstructure:** After the completion of the shaker tests, only minor cracks were observed on the superstructure. Fine cracks of 0.05 mm were found on the bottom of the

columns on Floor 1, and fine vertical cracks of less than 0.08 mm were found on the beams on Floors 1 to 5. No cracks were observed on columns on other floors.

**Box foundation:** After the shaker tests, the box foundation was taken out from the soil container. No cracks were observed from the box foundation.

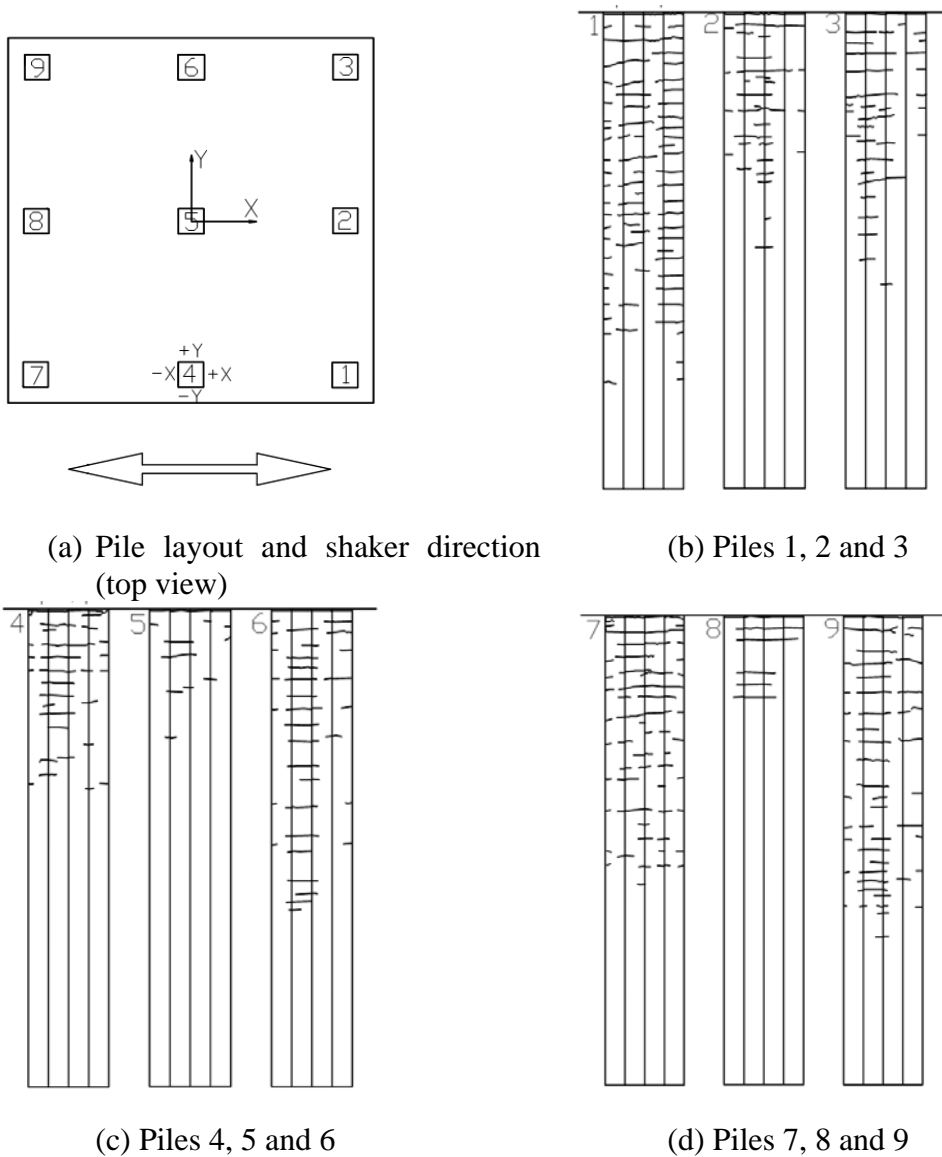


Figure 3.12: Layout of the pile foundation and cracks on the piles visually inspected after the shaker tests.

### 3.5.2 Local Damage Quantification Using Nonlinear MRFM Identification

The damage in the SFS systems involves localized structural characteristics change associated with coupled nonlinear behaviors of the superstructure, the foundation and the soil. Therefore, MRFM could be used to quantify such localized nonlinear damage in a chain-like system by identifying the individual interstory restoring forces in Equation 3.5.

When the earthquake-induced damage occurred in the superstructure of the SFS systems, a portion of the seismic energy absorbed into the superstructure was dissipated in the form of the damage described in Section 4.1. Therefore, if the dissipated energy during a seismic event can be quantified, it can be used as an indicator to quantify the severeness of structural damage. The amount of this energy dissipation can be determined by calculating the area of the identified interstory restoring forces of the stiffness phase diagrams in Figure 3.6. Figure 3.13 illustrates the dissipated energies associated with structural damage in the superstructure with the fixed, pile and box foundations at different excitation levels of the Shanghai artificial wave. In the figure, as the peak acceleration increases, it is hypothesized that more damage is accumulated in the SFS systems. The largest dissipated energies were observed with the fixed foundation (Figure 3.13a), and the smallest dissipated energies were observed with the box foundation (Figure 3.13c). These results can be explained because the seismic energy induced by the shaker was transferred to the superstructure with the fixed foundation without energy loss, while the foundation and the soil of the superstructures through the pile and box foundations dissipated the seismic energy of the shaker motion.

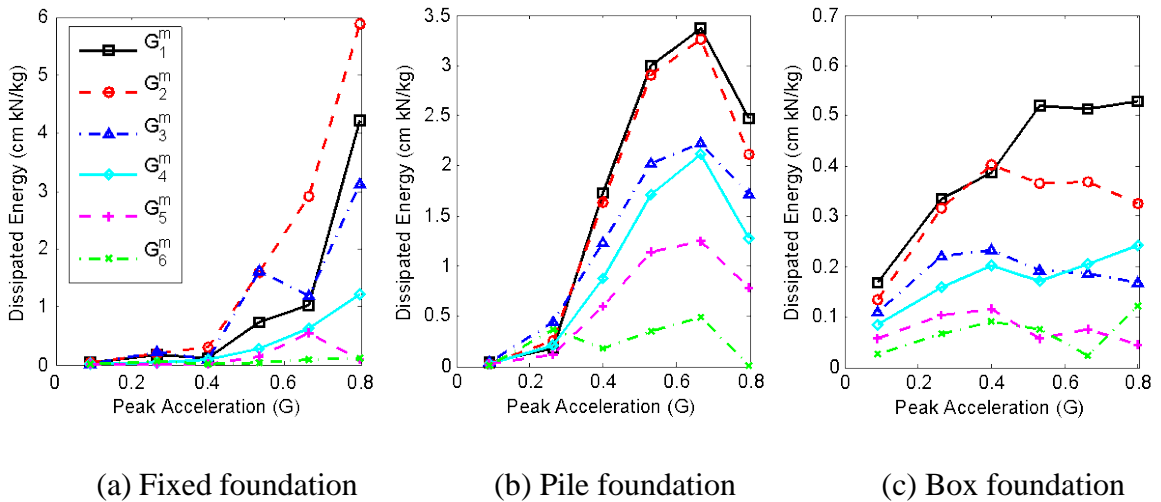


Figure 3.13: Dissipated energies associated with structural damage in the superstructure with fixed, pile and box foundations at different excitation levels of the Shanghai artificial waves.

To understand the energy dissipation effects of the soil and the foundations, the energies of the acceleration at the shaker (A0) and the ground (A1) were calculated by finding the areas under their power spectral densities for different foundation types (Figure 3.14). The solid line indicates the original seismic energy induced by the shaker motion (A0), and the dashed line indicates the seismic energy introduced to the superstructure (A1) that is reduced due to energy dissipation through the soil and the foundation. For the fixed foundation (Figure 3.14a), the acceleration energies at A0 and A1 were identical due to no seismic energy dissipation with the rigid connection between the shaker and the superstructure base. Larger energy dissipation was observed with the box foundation (Figure 3.14c) than the pile foundation (Figure 3.14b) since the pile foundation was a more rigid foundation than the box foundation.

For the fixed foundation in Figure 3.13a, it was shown that the dissipated energy of  $G_1^m$  (Floors 1 and 2),  $G_2^m$  (Floors 3 and 4), and  $G_3^m$  (Floors 5 and 6) increased significantly from Excitation Lv. 4 (peak acceleration of 0.532 G). This result agrees with the visual inspection result since vertical cracks in the beams on Floors 1 to 5 observed at Excitation Lv. 2 were continuously developed as the excitation level increased, and cracks were observed on those Floor 1 columns. The largest energy was dissipated with  $G_2^m$  since the upper part of a concrete column on Floor 3 crushed at Excitation Lv.4. At Excitation Lv. 6 (the peak acceleration of 0.798 G), the largest dissipated energies were estimated with  $G_2^m$  and  $G_3^m$  since the concrete columns on Floors 2 and 3 crushed.

For the pile foundation in Figure 3.13b, the dissipated energy with  $G_1^m$  (Floors 1 and 2) was dominant with similar magnitudes at Excitation Lv. 6 (peak acceleration of 0.798 G). This result agrees with the visual inspection result that cracks were observed only on the Floor 1 columns. It should be noted that, for the fixed foundation, the dissipated energy of  $G_2^m$  was dominant instead of  $G_1^m$ . The overall dissipated energy with the pile foundation is smaller than the energy with the fixed foundation since the shaker seismic energy transferred to the superstructure is smaller with the pile foundation, which can be validated with the fact that the cracks with the pile foundation were less severe than those with the fixed foundation from the visual inspection. However, the largest dissipated energy was found for all floors at Excitation Lv. 5 (peak acceleration of 0.665 G), and the dissipated energy decreased although the shaker motion increased Excitation Lv. 6 (peak acceleration of 0.798 G). This is because the seismic energy transferred into the superstructure at A1 was saturated at Excitation Lv.3 (peak acceleration of 0.399 G) and

decreased at Excitation Lv.6 (peak acceleration of 0.798 G) as shown in Figure 3.14b. The decrease of the transferred energy could be due to the damage in the pile foundation illustrated in Figure 3.12. For the box foundation, on the other hand, the transferred energy at A1 continuously increased as the shaker excitation increased (Figure 3.14c) since no cracks were found on the box foundation from the visual inspection.

For the box foundation in Figure 3.13c, prominent change in dissipated energy was observed with  $G_1^m$  (Floors 1 and 2) at Excitation Lv. 4 (the peak acceleration of 0.532 G), which agrees with the visual inspection results that cracks were observed on both the beams and columns only on Floor 1. No significant change of the dissipated energy was observed on the other floors, which also agrees with the visual inspection results.

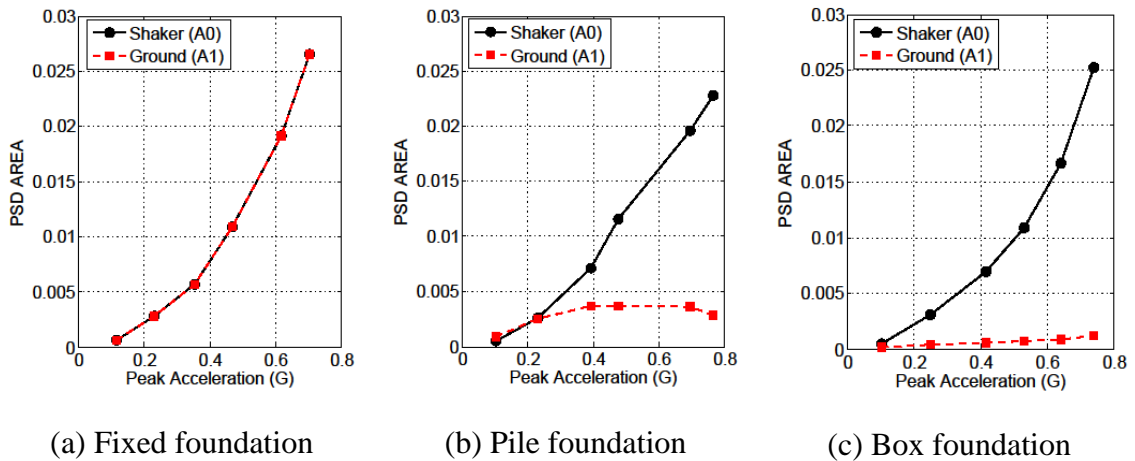


Figure 3.14: The energies of the acceleration at the shaker (A0) and the ground (A1) for different foundation types. The accelerometer locations are shown in Figure 3.1.

The superstructure damage quantified as the dissipated energy can be further investigated using the identified power-series coefficients that were shown in Figure 3.10.

Figure 3.15 shows the identified power-series coefficients of the linear stiffness ( $a_{10}^m$ ), cubic stiffness ( $a_{30}^m$ ), and linear damping ( $a_{01}^m$ ) for different peak acceleration excitations. As the superstructure damage was accumulated by increasing the excitation level, the stiffness-related coefficients (i.e.,  $a_{10}^m$  and  $a_{30}^m$ ) decreased while the damping-related coefficient (i.e.,  $a_{01}^m$ ) increased for the lower floors ( $G_1^m$  and  $G_2^m$ ). Therefore, the structural damage can be characterized that the damage reduced the linear and cubic stiffness, and increased the damping.

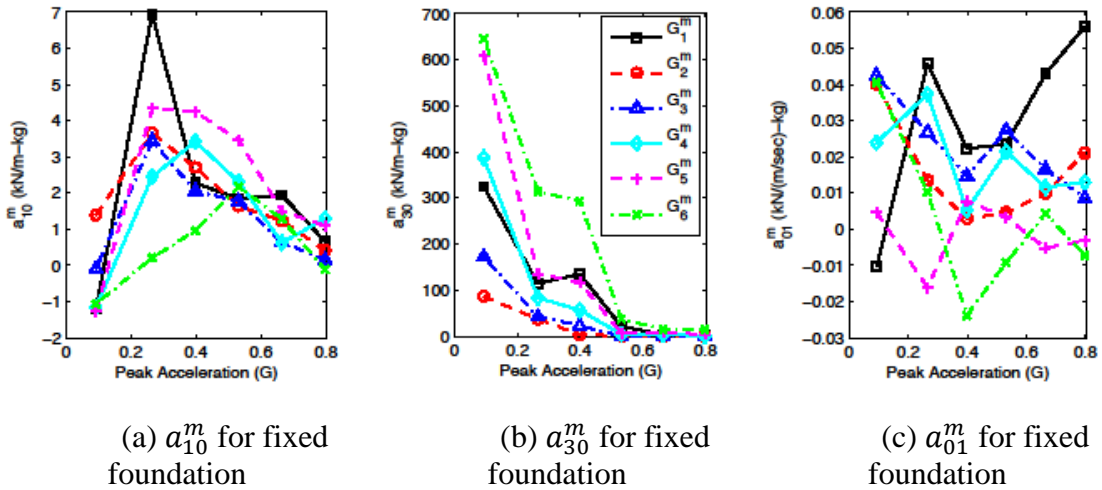


Figure 3.15: Identified power-series coefficients of (a) the linear stiffness,  $a_{10}^m$ , (b) cubic stiffness,  $a_{30}^m$ , and (c) linear damping,  $a_{01}^m$ , at different excitation levels of the Shanghai artificial waves.

### 3.5.3 Nonlinear Effects on Mode Shape Identification

Among numerous multi-degree of freedom system identification methods, the experimental modal analysis method would be considered as the standard vibration-based global system identification technique for multi-degree-of-systems. Therefore, it will be

useful if the MRFM identification results can be expressed to be comparable to the modal analysis identification results.

Assumed to be a *linear* system, the superstructure can be expressed with the following equation of motion:

$$M\ddot{y}(t) + C\dot{y}(t) + Ky(t) = -Mu\ddot{s}(t) \quad (3.12)$$

where  $M$  is the mass matrix;  $C$  is the damping matrix;  $K$  is the stiffness matrix;  $u$  is the unit column vector;  $\ddot{s}(t)$  is the base acceleration, and  $\dot{y}(t) = \dot{x}(t) - \dot{s}(t)$  is the relative acceleration of the absolute acceleration  $\dot{x}(t)$ . The *global*  $M^{-1}K$  and  $M^{-1}C$  matrices can be determined using the *local* stiffness and damping coefficients,  $k_i^m$  and  $c_i^m$ , using the identified the linear stiffness and damping power-series coefficients ( $a_{10}^m$  and  $a_{01}^m$ , respectively) as

$$M^{-1}K = \begin{bmatrix} k_1^m + k_2^m \bar{m}_1 & -k_2^m \bar{m}_1 & 0 & \dots & 0 \\ -k_2^m & k_2^m + k_3^m \bar{m}_2 & -k_3^m \bar{m}_2 & \dots & 0 \\ 0 & \ddots & \ddots & \ddots & 0 \\ 0 & \dots & -k_{n-1}^m & k_{n-1}^m + k_n^m \bar{m}_{n-1} & -k_n^m \bar{m}_{n-1} \\ 0 & \dots & 0 & -k_n^m & k_n^m \end{bmatrix} \quad (3.13)$$

and

$$M^{-1}C = \begin{bmatrix} c_1^m + c_2^m \bar{m}_1 & -c_2^m \bar{m}_1 & 0 & \dots & 0 \\ -c_2^m & c_2^m + c_3^m \bar{m}_2 & -c_3^m \bar{m}_2 & \dots & 0 \\ 0 & \ddots & \ddots & \ddots & 0 \\ 0 & \dots & -c_{n-1}^m & c_{n-1}^m + c_n^m \bar{m}_{n-1} & -c_n^m \bar{m}_{n-1} \\ 0 & \dots & 0 & -c_n^m & c_n^m \end{bmatrix} \quad (3.14)$$

where  $i$  is the index of the lumped mass, and  $\bar{m}_i = m_{i+1}/m_i = 1$  in this study since the lumped mass of each floor of the superstructure is identical.



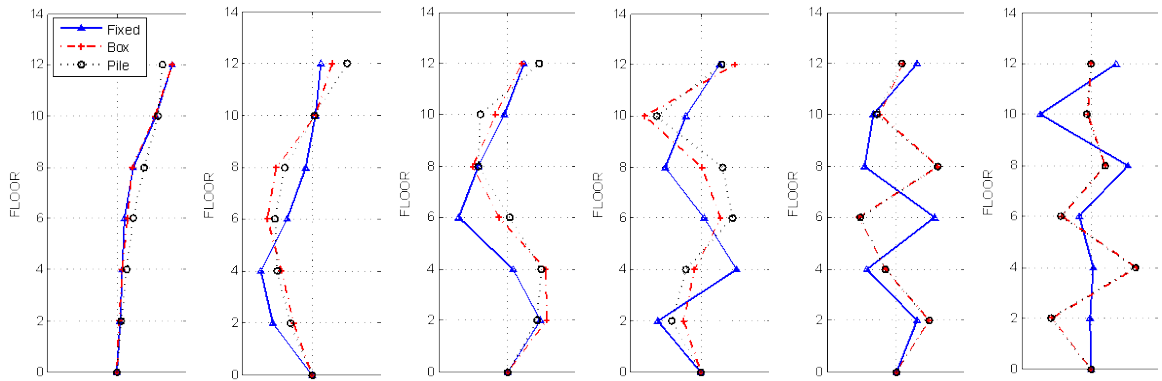
Combining with the Natural Excitation Technique (NExT) [16] for the unknown ambient excitation, Nayeri et al. [11] showed that the mode shapes identified using the MRFM (NExT -MRFM) had a good agreement with the mode shapes identified using the Eigensystem Realization Algorithm (NExT-ERA) [17-19] for a full-scale 17-story building subjected to ordinary service loads. At the low level of such service loads, the *linear* assumption of the building dynamic behaviors would be valid. Using the Shanghai artificial wave Lv. 6 in this study, however, the superstructure behaviors are significantly *nonlinear* as shown in Figure 3.6; consequently, the linear assumption in the experimental modal analysis is not valid.

In Figures 3.16a to 3.16f, a comparison is shown between the mode shapes determined using MRFM with the local stiffness coefficients ( $a_{10}^m$ ) and damping coefficients ( $a_{01}^m$ ) identified, and the mode shapes determined with the global stiffness matrix ( $M^{-1}K$ ) and damping matrix ( $M^{-1}C$ ) using the Deterministic Stochastic Subspace Identification (DSSI) in Figures 3.16g to 3.16l. The DSSI mode shapes were identified using the N4SID algorithm in Matlab System Identification Toolbox for the model order of 12, which is equivalent to 6 degrees of freedoms. The detailed description of DSSI can be found in Overschee and Moor. [20-21]

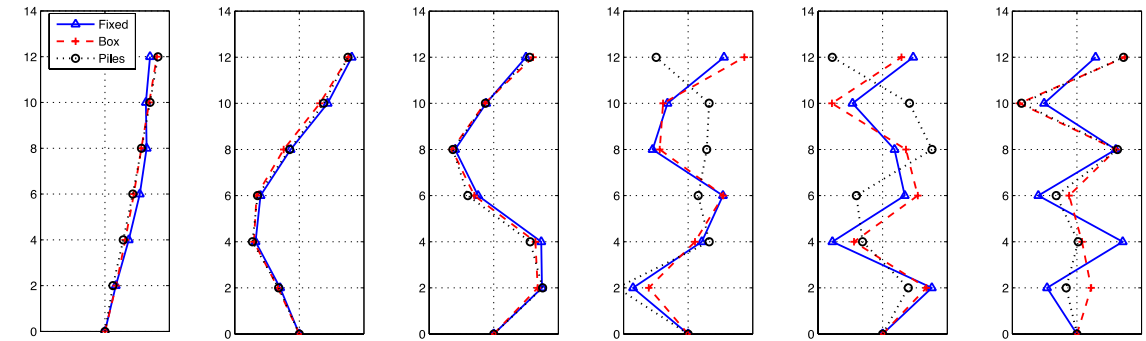
The MRFM mode shapes identified with the *local* stiffness and damping coefficients (Figures 3.16a to 3.16f) show that the mode shapes for the fixed foundation are different from those for the pile and box foundations for Modes 2 to 6, while the mode shapes for the pile and box foundations are similar for all modes. For the fixed foundation, the mode shapes for Modes 2 and 3 have larger slopes on  $m_1$  (Floors 1 to 2),  $m_2$  (Floors 3

to 4),  $m_3$  (Floors 5 to 6) than those for the pile and box foundations. These results agree with the interstory stiffness phase diagrams in Figure 3.6 (i.e., the decreased linear stiffness, and the increased hysteresis on Floors 1 to 6) as well as the visual inspection results (i.e., the concrete crush on Floors 2 and 3, and the wide cracks on Floors 2 to 5).

The DSSI mode shapes identified with the *global* stiffness and damping matrices (Figures 3.16g to 3.16l) show that the mode shapes for the fixed, pile and box foundations are almost identical for lower modes (i.e., Modes 1 to 3), while discrepancy is observed in higher modes (i.e., Modes 4 to 6). Therefore, the localized damage patterns for different foundation types observed in the visual inspection cannot be detected from the DSSI mode shapes.



(a) MRFM-Mode 1    (b) MRFM-Mode 2    (c) MRFM-Mode 3    (d) MRFM-Mode 4    (e) MRFM-Mode 5    (f) MRFM-Mode 6



(g) DSSI-Mode 1    (h) DSSI-Mode 2    (i) DSSI-Mode 3    (j) DSSI-Mode 4    (k) DSSI-Mode 5    (l) DSSI-Mode 6

Figure 3.16: Comparison of (a)-(f) the mode shapes determined with the localized stiffness and damping constants using the MRFM; and (g)-(l) the mode shapes determined with the global stiffness and damping matrices using the Deterministic Stochastic Subspace Identification (DSSI).

### 3.6 Conclusions

An extensive series of the shaker tests were conducted using the 1:10-scale, 12-story frame models with the fixed, pile and box foundations. The SFS models were tested using the El Centro, Kobe, Shanghai and white Gaussian earthquake excitations at 7

different peak acceleration levels with a shake table. The reinforced cast-in-place concrete frames were gradually damaged until they were failed as the excitation level increased. The dynamic response of the superstructure was measured using accelerometers during the shake table tests. Visual inspection was also conducted during and after the tests to examine damage on the superstructures and the foundations.

Significant nonlinear dynamic behaviors of the superstructures were observed from the interstory stiffness and damping phase diagrams. These interstory phase diagrams were useful for *qualitative* investigation for the localized nonlinear effects of damage on the superstructure dynamic behavior. Localized damage effects on the large-scale soil-foundation-superstructure (SFS) models were *quantified* using the nonlinear identification method of the Multi-degree-of-freedom Restoring Force Method (MRFM).

The main advantages of MRFM include:

1. MRFM is a *nonlinear* system identification method. Therefore, this method is useful when one has to characterize nonlinear system behaviors under extreme excitation conditions (e.g., earthquake or hurricane) or to quantify damage effects since damage usually involves nonlinear structural behavior.
2. MRFM is a *localized* system identification method. Therefore, combined with the above advantage of the nonlinear identification, this method is useful to localize structural damage with high accuracy since damage usually involves localized structural property change.
3. MRFM is a *non-parametric* identification method. Therefore, this method is useful to detect and characterize unpredictable system change (i.e., damage)

since damage involves not only the change of system parameter values, but also evolution into different system types. MRFM is flexible to model time-varying systems whose system parameters deteriorate over time.

4. There are no practical limitations on system excitation unlike some classical modal analysis techniques, such as the Eigensystem Realization Algorithm (ERA) or the Stochastic Subspace Identification (SSI).
5. The dissipated energy quantified using the term-wise identification can be used an excellent indicator to detect localized damage. The quantified damage effects can be further characterized using the identified power-series coefficients.
6. Mode shapes can be determined using the *local* stiffness and damping coefficients using Equations 3.13 and 3.14. The determined mode shapes can be compared with the mode shapes determined using the experimental modal analysis techniques with the *global* stiffness and damping matrices.
7. Storage requirements are compact for the characterization of arbitrary nonlinear systems in long-term monitoring applications: in this study, only a (5×5) two-dimensional array of the identified Chebyshev coefficients.

MRFM also has the following drawbacks including:

1. MRFM is only applicable to a chain-like system having a free end. Therefore, if the free end is structurally restrained (e.g., bridge-like structures), this method cannot be used without knowing the restoring force between the restraining boundary condition at the end of the system.

2. For nonlinear system identification, the force applied on each mass should be either negligible or known. Measuring those forces could be technically difficult in field applications. When the force applied on each mass is unknown, the system can still be analyzed with the assumption on system linearity combined with the Natural Excitation Technique. [11]

This paper is a part of companion literatures by the authors related to quantifying the seismic response datasets for the large-scale SFS systems with different foundation types, including computational modeling using the Artificial Neural Networks for response prediction and change detection in the SFS systems. [22]

### **3.7 Acknowledgement**

This work was supported by the project (Grant No. 51178349) of the National Natural Science Foundation of China, the Kwang-Hua Foundation for the College of Civil Engineering at Tongji University, China, and research collaboration between the University of Central Florida (UCF), and Korea Institute of Construction Technology (KICT).

### **3.8 References**

- [1] Kerschen, G., Worden, K., Vakakis, A. F., and Golinval, J.-C. (2006). “Past, present and future of nonlinear system identification in structural dynamics.” *Mechanical Systems and Signal Processing*, 20(3), 505–592.

- [2] Adams, D. (2007). *Health Monitoring of Structural Materials and Components: Methods with Applications*. John Wiley & Sons Inc, Chichester, West Sussex, England.
- [3] Worden, K., Farrar, C. R., Haywood, J., and Todd, M. (2008). “A review of nonlinear dynamics applications to structural health monitoring.” *Structural Control and Health Monitoring*, 15, 540–567.
- [4] Takewaki, I., Nakamura, M., and Yoshitomi, S. (2011). *System Identification for Structural Health Monitoring*. WIT Press, Billerica, MA, USA.
- [5] Farrar, C. R., and Worden, K. (2013). *Structural Health Monitoring: A Machine Learning Perspective*. John Wiley & Sons Inc.
- [6] Chen, B., Lu, X., and Li, P. (2002). “Modeling of dynamic soil-structure interaction by ANSYS.” *2nd Canadian Specialty Conference on Computer Applications in Geotechnique*, Winnipeg, Canada, 21–26.
- [7] Lu, X., Li, P., Chen, Y., and Chen, B. (2004). “Shaking table model testing on dynamic soil-structure interaction system.” *13th World Conference on Earthquake Engineering*, Vancouver, B.C., Canada.
- [8] Lu, X., Li, P., Chen, B., and Chen, Y. (2005). “Computer simulation of the dynamic layered soil–pile–structure interaction system.” *Canadian Geotechnical Journal*, 42(3), 742–751.
- [9] Masri, S. F., Bekey, G. A., Sassi, H., and Caughey, T. K. (1982). “Non-parametric identification of a class of nonlinear multidegree dynamic systems.” *Earthquake Engineering & Structural Dynamics*, 10(1), 1–30.

- [10] Masri, S. F., and Caughey, T. K. (1979). "A Nonparametric Identification Technique for Nonlinear Dynamic Problems." *Journal of Applied Mechanics*, 46(2), 433–447.
- [11] Nayeri, R. D., Masri, S. F., Ghanem, R. G., and Nigbor, R. L. (2008). "A novel approach for the structural identification and monitoring of a full-scale 17-story building based on ambient vibration measurements." *Smart Materials and Structures*, 17(2), 025006.
- [12] Yun, H.-B., and Masri, S. F. (2008). "Stochastic change detection in uncertain nonlinear systems using reduced-order models: system identification." *Smart Materials and Structures*, 17(1), 015040.
- [13] Yun, H.-B., and Masri, S. F. (2009). "Stochastic change detection in uncertain nonlinear systems using reduced-order models: classification." *Smart Materials and Structures*, 18(1), 015004.
- [14] Worden, K., and Tomlinson, G. R. (2001). *Nonlinearity in Structural Dynamics: Detection, Identification and Modelling*. Institute of Physics Publishing, Bristol, UK.
- [15] Chirokov, A. (2006). "Scattered Data Interpolation and Approximation using Radial Base Functions."  
<<http://www.mathworks.com/matlabcentral/fileexchange/10056-scattered-data-interpolation-and-approximation-using-radial-base-functions>> (Oct. 3, 2013).



- [16] James, G. H., Carrie, T. G., and Lauffer, J. P. (1993). *The Natural Excitation Technique (NExT) for Modal Parameter Extraction From Operating Wind Turbines. Sandia Report*, Albuquerque, NM, USA.
- [17] Juang, J. N., and Pappa, R. S. (1985). “An eigensystem realization algorithm for modal parameter identification and model reduction.” *Journal of guidance, control, and dynamics*, 8, 620–627.
- [18] Juang, J. N., and Pappa, R. S. (1986). “Effects of noise on modal parameters identified by the Eigensystem Realization Algorithm.” *Journal of Guidance, Control, and Dynamics*, 9(3).
- [19] Caicedo, J. M. (2011). “Practical Guidelines for the Natural Excitation Technique (NExT) and the Eigensystem Realization Algorithm (ERA) for Modal Identification Using Ambient Vibration.” *Experimental Techniques*, 35(4), 52–58.
- [20] Overschee, P. Van, and Moor, B. De. (1992). *N4SID: Subspace Algorithms for the Identification of Combined Deterministic-Stochastic Systems*. Heverlee, Belgium.
- [21] Overchee, P. Van, and Moor, B. De. (1996). *Subspace Identification for Linear Systems: Theory, Implementation, Applications*. Kluwer Academic Publishers, Norwell, Massachusetts, USA.
- [22] Derkevorkian, A., Hernandez-Garcia, M., Yun, H.-B., and Masri, S. F. (2013). “Computational models for response prediction and change detection in nonlinear soil-foundation-superstructure systems.” *ASCE Engineering Mechanics*. (under review)

## **CHAPTER 4: A COMPARATIVE STUDY OF MODE DECOMPOSITION USING NExT-ERA, PCA AND ICA FOR DIFFERENT EXCITATIONS**

### **4.1 Abstract**

This paper discusses a comparative study to relate parametric and non-parametric mode decomposition algorithms for response-only data. Three popular mode decomposition algorithms are included in this study: the Eigensystem Realization Algorithm with the Natural Excitation Technique (NExT-ERA) for the parametric algorithm, as well as the Principal Component Analysis (PCA) and the Independent Component Analysis (ICA) for the non-parametric algorithms. A comprehensive parametric study is provided for i) different response types, ii) excitation types, iii) system damping, and iv) sensor spatial resolution to compare the mode shapes and modal coordinates of using a 10-DOF building model. The mode decomposition results are also compared using a unique dynamic response data collected in a ship-bridge collision accident for ambient excitation with traffic loading, ambient excitation without traffic loading, and impulse excitation.

### **4.2 Nomenclatures:**

$\ddot{X}(t), \dot{X}(t), X(t)$	The system acceleration, velocity and displacement, respectively.
$\Psi^{\text{TRU}}$	The true mode shape determined by the modal superposition method.

$\hat{\Psi}_{\ddot{X}}^{\text{ERA}}$ , $\hat{\Psi}_{\dot{X}}^{\text{ERA}}$ , $\hat{\Psi}_X^{\text{ERA}}$	The mode shapes estimated with the Eigensystem Realization Algorithm with Natural Excitation Method (NExT-ERA) for $\ddot{X}(t)$ , $\dot{X}(t)$ , and $X(t)$ , respectively.
$\hat{\Psi}_{\ddot{X}}^{\text{PCA}}$ , $\hat{\Psi}_{\dot{X}}^{\text{PCA}}$ , $\hat{\Psi}_X^{\text{PCA}}$	The mode shapes estimated with the Principal Component Analysis (PCA) method for $\ddot{X}(t)$ , $\dot{X}(t)$ , and $X(t)$ , respectively.
$\hat{\Psi}_{\ddot{X}}^{\text{ICA}}$ , $\hat{\Psi}_{\dot{X}}^{\text{ICA}}$ , $\hat{\Psi}_X^{\text{ICA}}$	The mode shapes estimated with the Independent Component Analysis (ICA) method for $\ddot{X}(t)$ , $\dot{X}(t)$ , and $X(t)$ , respectively.
$p^{\text{TRU}}$	The true modal coordinate determined by the modal superposition method.
$\hat{p}_{\ddot{X}}^{\text{ERA}}$ , $\hat{p}_{\dot{X}}^{\text{ERA}}$ , $\hat{p}_X^{\text{ERA}}$	The modal coordinates estimated with the Eigensystem Realization Algorithm with Natural Excitation Method (NExT-ERA) for $\ddot{X}(t)$ , $\dot{X}(t)$ , and $X(t)$ , respectively.
$\hat{p}_{\ddot{X}}^{\text{PCA}}$ , $\hat{p}_{\dot{X}}^{\text{PCA}}$ , $\hat{p}_X^{\text{PCA}}$	The modal coordinates estimated with the Principal Component Analysis (PCA) method for $\ddot{X}(t)$ , $\dot{X}(t)$ , and $X(t)$ , respectively.
$\hat{p}_{\ddot{X}}^{\text{ICA}}$ , $\hat{p}_{\dot{X}}^{\text{ICA}}$ , $\hat{p}_X^{\text{ICA}}$	The modal coordinates estimated with the Independent Component Analysis (ICA) method for $\ddot{X}(t)$ , $\dot{X}(t)$ , and $X(t)$ , respectively.

### **4.3 Introduction**

Mode decomposition techniques are popularly used in the identification of multi degree-of-freedom (MDOF) dynamic systems. The experimental modal analysis is classified into the parametric mode decomposition technique. The modal analysis can be further categorized into input-output modal identification and output-only modal

identification, depending on the availability of the excitation measurement in forced vibration applications. Since measuring the forces of MDOF systems is technically difficult and often expensive, the output-only modal identification method is commonly used when the force measurement is not available, but usually with an assumption that the excitation input is a zero-mean Gaussian white noise. There are two main groups of the output-only modal identification method: frequency-domain and time-domain methods [1].

On the other hand, the Principal Component Analysis (PCA) and Independent Component Analysis (ICA) can be classified into the non-parametric mode decomposition techniques which are in a family of the Blind Source Separation (BSS) techniques. The mathematical models of these techniques are not based on certain physical assumptions (e.g., the equation of motion) but data-driven. The identification is relatively simple and straightforward since the vibration modes can be determined from the columns of the transformation matrix that can be determined based on underlying statistics of the response data. The PCA, known also as the Proper Orthogonal Decomposition (POD), Second-Order Blind Identification (SOBI), or Karhunen-Loève (K-L) decomposition, decomposes multivariate response data into statistically uncorrelated data based on the second-order statistics, while the ICA decomposes the response data into statistically independent data based on the fourth-order statistics.

The objective of this paper is to compare the mode decomposition results using NExT-ERA, PCA and ICA methods for MDOF systems through simulation and experimental studies. A parametric study was conducted to evaluate the performance of the mode decomposition techniques for i) response types, ii) excitation types, iii) system

damping, and iv) sensor spatial resolution. The simulation study was conducted using 10-DOF lumped-mass models. The experimental study was conducted using a full-scale suspension bridge under different excitation conditions in a ship-bridge collision accident, including traffic, no traffic, and collision. The mode shapes and modal coordinates were identified using those mode decomposition methods. Then, in the simulation study the mode shapes and modal coordinates identified by NExT-ERA, PCA and ICA were compared with the true ones, and in the experimental study the mode shapes and modal coordinates identified by PCA and ICA were compared with those by NExT-ERA. An overview of the proposed comparative study is shown in Figure 4.1.

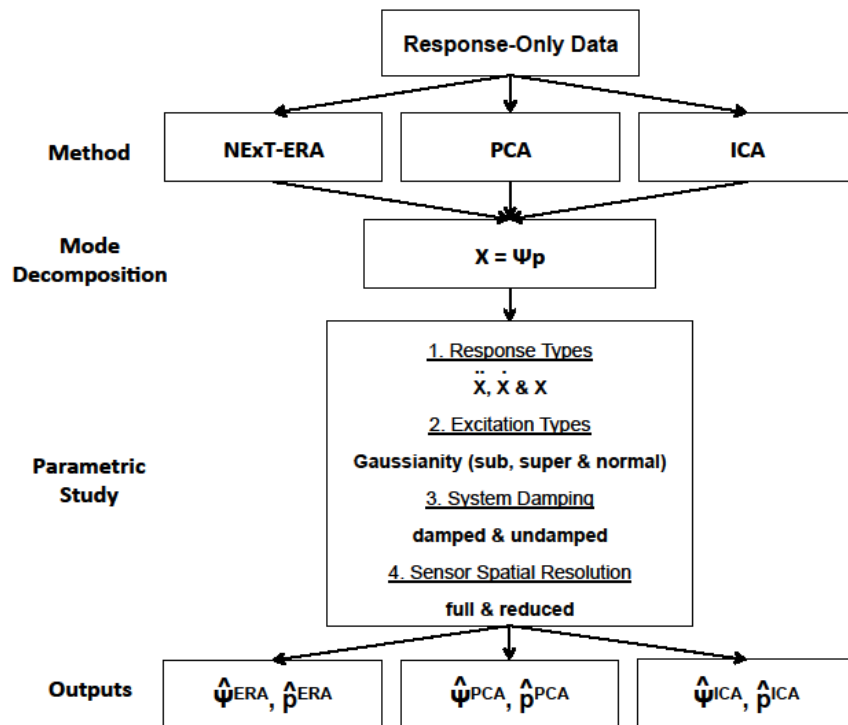


Figure 4.1: Study overview for the performance evaluation of the mode decomposition using NExT-ERA, PCA and ICA.

Prior to this study, there were analytical and experimental studies to relate the parametric modal analysis methods to the non-parametric blind source separation methods for the identification of vibrational structures. For PCA, Feeny and Kappagantu [2] related POD to free vibration and compared mode shapes and modal coordinates using low-dimensional numerical models. Feeny and Liang [3] related POMs to linear normal of lumped and continuous-mass systems. They found that POD works with random excitation. Kerschen et al. [4] presented an overview of POD method for dynamic characterization and the order reduction of mechanical systems. They stated that the proper orthogonal modes (POMs) may be considered as an alternative to the linear mode shapes although they do not have the theoretical foundations. POMs and Proper Orthogonal Values (POVs) provide a good characterization of the dynamics without requiring the knowledge of the structural matrices. They stated that POD can thus determine an appropriate embedding space for a low-dimensional structure. Zhou and Chelidze [5] compared the Algorithm for Multiple Unknown Signal Extraction (AMUSE), SOBI, and Ibrahim Time-Domain Modal Analysis (ITD) methods using noisy free response data for damped and undamped systems. Smith and Saitta [6] employed PCA for analysis and damage detection for complex structures, compared with multiple model-free data interpretation methods including the Correlation Analysis, Continuous Wavelet Transform (CWT), Short-Term Fourier Transform (STFT), and Instance-Based Method (IBM). Posenato et al. [7] applied PCA combined with the K-mean clustering for data mining to interpret multiple model predictions. McNeil and Zimmerman [8] discussed the

relationship between independent component and free-vibration modal responses using the free-vibrational modal responses of a diagonally-damped model through their simulation study. They deduced that undamped modal responses closely correspond to independent components, while damped modal responses do not. Antoni and Chauhan [9] compared SOBI method with the Stochastic Subspace Identification (SSI) method for an analytical 15-DOF systems by comparing their mode shapes and natural frequencies. They found that the validity of is in principle limited to conservative systems, yet it is quite robust to this assumption.

For ICA, Roan et al. [10] applied ICA to detect and analyze gear tooth failure. Kerschen et al. [11] related the vibration modes of mechanical systems to ICA modes for their mode shapes and modal coordinates. They found that the ICA modes agreed well with the vibrational modes for an undamped system subjected to impulse and uniform random excitation while a damped system gave higher discrepancy. Poncelet et al. ([12]; [13]) compared the mode shapes and modal coordinates identified with ICA and SOBI to true ones. ICA gave a good agreement for weakly damped systems. SOBI gave smaller discrepancy for strongly damped systems than ICA. Yang and Nagarajaiah [14] found that the time-domain ICA is limited to lightly damped structure, and SOBI lost robustness in nonstationary and unknown noisy environment. They proposed STFT-ICA for both lightly and highly damped structures.

More recently, the Sparse Component Analysis (SCA) has been studied to estimate modal parameters for underdetermined problems: Yang and Nagarajaiah [15] applied SCA to the underdetermined problem where sensors may be highly limited compared to the

number of active modes. Yu and Bai (2014) applied SCA to estimate both time-invariant and time-varying modal parameters of a small-scale column in laboratory tests using a limited number of accelerometers.

The above studies were conducted using numerical or laboratory models. Large-scale field structures have been identified using BSS methods. Oh et al. [17] applied Kernel PCA (KPCA) for the structural health monitoring of the Yeongjong suspension bridge in South Korea to perform data normalization and incorporated with a novelty index and generalized extreme value statistics for novelty detection. Kallinikidou et al. [18] applied POD for long-term monitoring of the Vincent Thomas suspension bridge in California, U.S.A. The statistics of acceleration covariance matrices (ACMs) were evaluated, and the relation between POMs and vibrational mode shapes were studied. Yun et al. [19] applied adaptive PCA to a tunnel structure to evaluate proximity excavation effects on the tunnel using POMs and POVs.

Although the relationships between NExT-ERA, PCA, and ICA have been investigated in the above studies, these studies were conducted for a limited number of parameters that affect the performance of mode decomposition. This paper presents a comprehensive parametric study for response types, excitation types, system damping, and sensor spatial resolution. Most of the studies were conducted only using simulation models or small-scale models in laboratory, and the response data obtained from full-scale field structures were relatively rarely studied. The experimental study includes analysis results for the impulse vibration, ambient vibration with traffic, and ambient vibration without



traffic, which are unique datasets to investigate the performance of the mode decomposition for different excitation types.

This paper is outlined as follows: the mathematical background of NExT-ERA, PCA and ICA methods are described in Section 4.4; the results of the simulation study using the 10-DOF building models are presented and discussed in Section 4.5; the results of the experimental study using the ship-bridge collision data are also presented and discussed in Section 4.6; and finally the conclusions are shown in Section 4.7.

#### **4.4 Mode Decomposition Techniques**

##### **4.4.1 Eigen Realization Algorithm with Natural Excitation Technique (NExT-ERA)**

In general, the MDOF linear system subjected to the forced vibration of ambient excitation can be expressed as the following equation of motion:

$$\mathbf{M}\ddot{\mathbf{X}}(t) + \mathbf{C}\dot{\mathbf{X}}(t) + \mathbf{K}\mathbf{X}(t) = \mathbf{F}(t) \quad (4.1)$$

where  $m$  is the number of sensors that is larger than the degrees of freedom of the system;  $N$  is the number of data points over time;  $\mathbf{M}$ ,  $\mathbf{C}$  and  $\mathbf{K}$  are the  $(m \times m)$  mass, damping and stiffness matrices, respectively;  $\ddot{\mathbf{X}}(t)$ ,  $\dot{\mathbf{X}}(t)$ ,  $\mathbf{X}(t)$ , and  $\mathbf{F}(t)$  are the  $(m \times N)$  matrices of the system displacement, velocity, acceleration, and ambient excitation, respectively.

The Eigen Realization Algorithm (ERA) is an output-only modal analysis technique for a MDOF linear dynamic system with an assumption of impulse excitation [20]. Since ERA is designed for free vibration, the original ERA should be modified to

deal with ambient excitation. The Natural Excitation Technique (NExT) [21] is commonly used with ERA for this modification as

$$\mathbf{M}R_{X_{\text{ref}}\ddot{X}}(\tau) + \mathbf{C}R_{X_{\text{ref}}\dot{X}}(\tau) + \mathbf{K}R_{X_{\text{ref}}X}(\tau) = R_{X_{\text{ref}}F}(\tau) \quad (4.2)$$

where  $R(\cdot)$  is the cross-correlation function; and  $X_{\text{ref}}(\tau)$  is the reference displacement with a time lag,  $\tau$ . If the reference channel displacement and input force are statistically uncorrelated, the RHS of Equation 4.2 vanishes. Using the following relationships

$$R_{X_{\text{ref}}\ddot{X}}(\tau) = \dot{R}_{X_{\text{ref}}\dot{X}}(\tau), \quad R_{X_{\text{ref}}\dot{X}}(\tau) = \ddot{R}_{X_{\text{ref}}X}(\tau) \quad (4.3)$$

Equation 4.3 becomes

$$\mathbf{M}\ddot{R}_{X_{\text{ref}}X}(\tau) + \mathbf{C}\dot{R}_{X_{\text{ref}}X}(\tau) + \mathbf{K}R_{X_{\text{ref}}X}(\tau) = 0 \quad (4.4)$$

Then, the original ERA technique can be applied to Equation 4.4 for the system modal parameters. In ERA, due to the noise in the data, the system order should be chosen to be higher than the real system order. Many studies, including Pappa et al. [22], discussed the system order role on the realization.

The mode condensation algorithm gives practical solution to distinguish between physical and noisy modes and perform the modal realization without the need to predefine the system order ([22]; [23]). Juang and Pappa [20] and Pappa et al. [24] suggested different mode indicators to measure the accuracy of mode identification. These mode indicators are incorporated in the mode condensation algorithm in order to separate physical modes from the noisy modes. The Consistent Mode Indicator (CMI) used in this study is expressed as [24]

$$\text{CMI}_i = \text{EMAC}_i \cdot \text{MPC}_i \quad (4.5)$$

where  $\text{EMAC}_i$  is the extend mode amplitude coherence of mode  $i$ , which quantifies the temporal consistency of the identified mode, and  $\text{MPC}_i$ , the modal phase collinearity, quantifies the spatial consistency of the corresponding mode. Therefore  $\text{CMI}_i$  quantify both of the temporal and spatial consistency.  $\text{CMI}_i$ ,  $\text{EMAC}_i$ , and  $\text{MPC}_i$  have values from 0 % to 100 %.

#### 4.4.2 Principal Component Analysis (PCA)

The Principal Component Analysis (PCA) converts the response data that are correlated between sensor channels into *statistically uncorrelated* data as follows:

$$\begin{aligned} \ddot{X}(t) &= \Psi_X^{\text{PCA}} p_X^{\text{PCA}}(t), & \dot{X}(t) &= \Psi_X^{\text{PCA}} p_X^{\text{PCA}}(t), \\ X(t) &= \Psi_X^{\text{PCA}} p_X^{\text{PCA}}(t) \end{aligned} \quad (4.6)$$

where  $p_X^{\text{PCA}}(t)$ ,  $p_{\dot{X}}^{\text{PCA}}(t)$ , and  $p_{\ddot{X}}^{\text{PCA}}(t)$  are the  $(m \times N)$  matrices of the modal coordinates for the system acceleration, velocity and displacement, which are statistically uncorrelated between the coordinate components;  $\Psi_X^{\text{PCA}}$  is the transformation matrix of the acceleration to be determined for the linear transformation from  $\ddot{X}(t)$  to  $p_X^{\text{PCA}}(t)$ ; and in the same manner for  $\dot{X}(t)$  and  $X(t)$ . The columns of  $\Psi_X^{\text{PCA}}$  represent the mode shapes of the response data.

The purpose of PCA is to find the orthonormal  $\Psi_X^{\text{PCA}}$ ,  $\Psi_{\dot{X}}^{\text{PCA}}$ , or  $\Psi_{\ddot{X}}^{\text{PCA}}$  matrices that make the components of  $p_X^{\text{PCA}}(t)$ ,  $p_{\dot{X}}^{\text{PCA}}(t)$ , or  $p_{\ddot{X}}^{\text{PCA}}(t)$  be statistically uncorrelated by

making the covariance matrix of the modal coordinates be a diagonal matrix. The uncorrelated modal coordinates can be determined by using the second-order statistics from

$$\Sigma_{\ddot{X}} = E[p_{\ddot{X}}^{\text{PCA}} p_{\ddot{X}}^{\text{PCA} T}] = E[\Psi_{\ddot{X}}^{\text{PCA}} p_{\ddot{X}}^{\text{PCA}} p_{\ddot{X}}^{\text{PCA} T} \Psi_{\ddot{X}}^{\text{PCA} T}] = \Psi_{\ddot{X}}^{\text{PCA}} \Gamma_{\ddot{X}} \Psi_{\ddot{X}}^{\text{PCA} T} \quad (4.7)$$

where  $\Sigma_{\ddot{X}}$  is the covariance matrix of  $\ddot{X}(t)$ ;  $\Gamma_{\ddot{X}}$  is the covariance matrix of  $p_{\ddot{X}}(t)$ .

Equation 4.7 can be applied in the same manner for  $\dot{X}(t)$  and  $X(t)$ . PCA is the optimal linear algorithm since it obtains the minimum expected squared distance between the original signal and its dimension-reduced representation [4].

#### 4.4.3 Independent Component Analysis (ICA)

The Independent Component Analysis (ICA) is another mode decomposition technique in the BSS family to convert the response data into *statistically independent* data by the following linear transformation:

$$\begin{aligned} \ddot{X}(t) &= \Psi_{\ddot{X}}^{\text{ICA}} p_{\ddot{X}}^{\text{ICA}}(t), & \dot{X}(t) &= \Psi_{\dot{X}}^{\text{ICA}} p_{\dot{X}}^{\text{ICA}}(t), \\ X(t) &= \Psi_X^{\text{ICA}} p_X^{\text{ICA}}(t) \end{aligned} \quad (4.8)$$

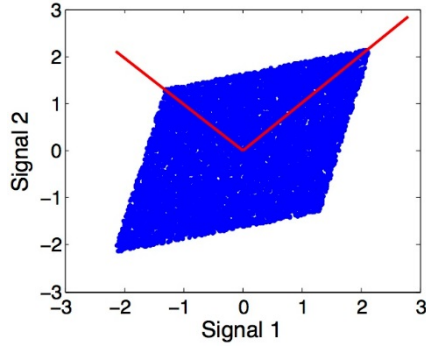
where  $p_{\ddot{X}}^{\text{ICA}}(t)$ ,  $p_{\dot{X}}^{\text{ICA}}(t)$ , and  $p_X^{\text{ICA}}(t)$  are the  $(m \times N)$  matrices of the modal coordinates for the system acceleration, velocity and displacement, which are statistically independent between the coordinate components;  $\Psi_{\ddot{X}}^{\text{ICA}}$  is the transformation matrix of the acceleration to be determined for the linear transformation from  $\ddot{X}(t)$  to  $p_{\ddot{X}}^{\text{ICA}}(t)$ ; and in the same manner for  $\dot{X}(t)$  and  $X(t)$ .

The objective of ICA is to find the mode shape matrices of  $\Psi_{\ddot{X}}^{\text{ICA}}$ ,  $\Psi_{\dot{X}}^{\text{ICA}}$ , or  $\Psi_X^{\text{ICA}}$ , which satisfy the components of  $p_{\ddot{X}}^{\text{ICA}}(t)$ ,  $p_{\dot{X}}^{\text{ICA}}(t)$ , or  $p_X^{\text{ICA}}(t)$  to be statistically

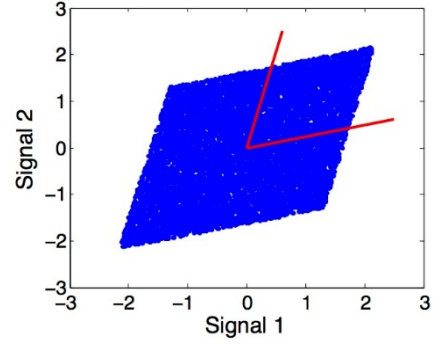
independent. Several methods are available to find the mode shape matrices. One approach is to maximize the non-Gaussianity of  $p_X^{\text{ICA}}(t)$ ,  $\dot{p}_X^{\text{ICA}}(t)$ , or  $\ddot{p}_X^{\text{ICA}}(t)$  for non-Gaussian system responses of  $\ddot{X}(t)$ ,  $\dot{X}(t)$ , or  $X(t)$  [24]. The major differences between PCA and ICA include

- PCA converts the system responses into statistically uncorrelated modal coordinates, while ICA converts the system responses into statistically independent modal coordinates.
- The PCA mode shape matrix (or transformation matrix) is orthonormal, while the ICA mode shape matrix is not necessarily orthonormal.
- The ICA modal coordinate (or transformed variable) has unit variance, while PCA modal coordinate is not necessarily having unit variance.
- PCA works with both Gaussian and non-Gaussian response data, while ICA does not work with Gaussian response data.

Figure 4.2 shows the phase diagram of bivariate uniform random variables with PCA and ICA mode components.



(a) PCA components



(b) ICA components

Figure 4.2: Comparison between PCA and ICA components for the bivariate uniform random variables.

#### 4.4.4 Mode Shapes and Modal Coordinates for Mode Decomposition Performance

In this study, the mode shapes and modal coordinates were identified to evaluate the mode-decomposition performance of the NExT-ERA, PCA and ICA as

$$p_Y(t) = \Psi_Y^{-1}Y(t) \quad (4.9)$$

where  $Y(t)$  is the system response of  $\ddot{X}(t)$ ,  $\dot{X}(t)$  or  $X(t)$ ;  $\Psi_Y$  is the matrix of the mode shapes or the transform matrix of NExT-ERA, PCA or ICA; and  $p_Y(t)$  is the modal coordinates of NExT-ERA, PCA or ICA.

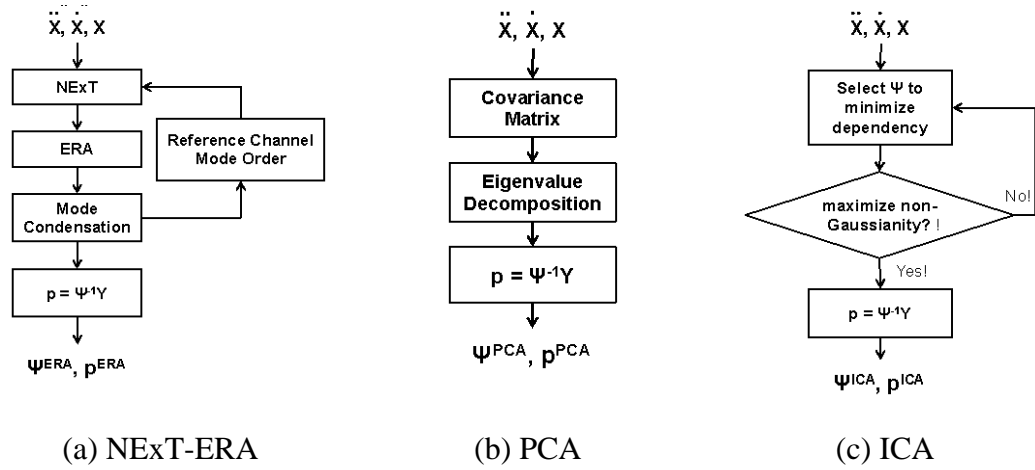


Figure 4.3: Procedures of NExT-ERA, PCA and ICA.

## 4.5 Simulation Study

### 4.5.1 Model Description

A 10-DOF multistory model was developed, which was fixed at the bottom and free at the top. The simulation model can be expressed using the following linear equation of motion:

$$\mathbf{M}\ddot{\mathbf{X}}(t) + \mathbf{C}\dot{\mathbf{X}}(t) + \mathbf{K}\mathbf{X}(t) = \mathbf{F}(t) \quad (4.10)$$

where  $\mathbf{M}$ ,  $\mathbf{K}$ , and  $\mathbf{C}$  are the  $10 \times 10$  matrices of the mass, damping, and stiffness, respectively;  $\mathbf{F}(t)$  is the  $(10 \times N)$  matrix of the external excitation;  $\mathbf{X}(t)$  are the  $(10 \times N)$  matrix of the system displacement; and  $N$  is the number of data points. The mass was set to be 1 kg, and the stiffness was set to be 500 N/m for all floors. The simulation models were developed for two different damping cases to investigate the effects of the system damping. The first is a zero-damping case as  $\mathbf{C} = \mathbf{0}$ , and the other is the damping case of

$\mathbf{C} = 0.001\mathbf{K} + 0.001\mathbf{M}$ . Equation 4.10 can be solved using the modal superposition method by writing the response in term of the generalized response as

$$X(t) = \Psi p(t) \quad (4.11)$$

where  $\Psi$  is the mode shape matrix; and  $p(t)$  is the modal displacement.  $\Psi$  can be evaluated by the eigenvalue decomposition as follows

$$\Psi \Omega^2 \Psi^{-1} = \mathbf{M}^{-1} \mathbf{K} \quad (4.12)$$

where  $\Omega$  is the frequency matrix of the system.

Equation 4.10 can be converted into uncoupled differential equations as

$$\mathbf{M}_n \ddot{p}(t) + \mathbf{C}_n \dot{p}(t) + \mathbf{K}_n p(t) = \Psi^{-1} F(t) \quad (4.13)$$

in which are the diagonal matrices of  $\mathbf{M}_n = \Psi^{-1} \mathbf{M} \Psi$ ,  $\mathbf{C}_n = \Psi^{-1} \mathbf{C} \Psi$ , and  $\mathbf{K}_n = \Psi^{-1} \mathbf{K} \Psi$ . The uncoupled differential equations can be written as

$$\ddot{p}_i(t) + 2 \omega_i \zeta_i \dot{p}_i(t) + \omega_i^2 p_i(t) = r_i(t) \quad (4.14)$$

where  $r_i(t)$  is the modal force that is the  $i$ -th row of  $\mathbf{M}_n^{-1} \Psi^{-1} F(t)$ ;  $p_i(t)$  is the modal displacement of the  $i$ -th mode; and  $i = 1, 2, \dots, 10$ .  $\omega_i$  and  $\zeta_i$  are the modal frequency and the damping ratio of the  $i$ -th mode, respectively as

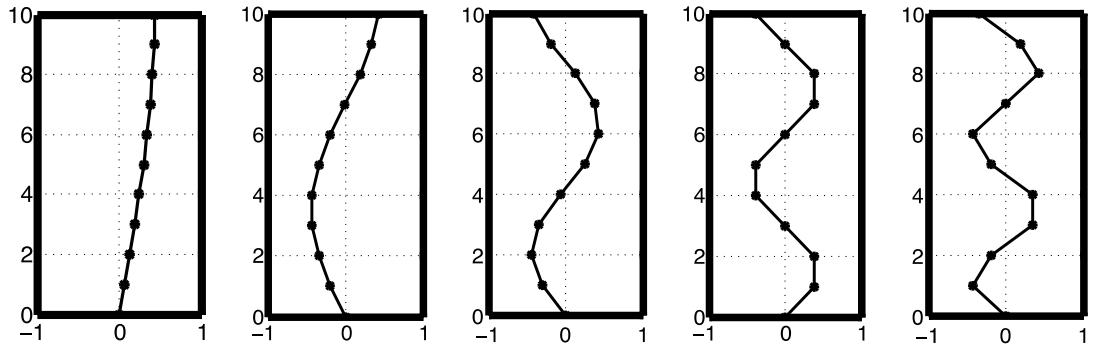
$$\omega_i = \Omega_{i,i} \quad \zeta_i = \frac{C_{n_{i,i}}}{2\omega_i M_{n_{i,i}}} \quad (4.15)$$

The modal frequencies and damping ratios of the simulation models are summarized in Table 4.1, and the mode shapes are shown in Figure 4.4.



Table 4.1: The modal frequencies and damping ratios of the simulation models.

Mode No.	Natural Frequency (Hz)	Damping Ratio (%)	Mode No.	Natural Frequency (Hz)	Damping Ratio (%)
1	0.53	0.26	6	5.22	2.32
2	1.58	0.71	7	5.88	2.61
3	2.60	1.16	8	6.41	2.85
4	3.56	1.58	9	6.8	3.02
5	4.44	1.97	10	7.04	3.13



(a) Mode 1 (b) Mode 2 (c) Mode 3 (d) Mode 4 (e) Mode 5  
Figure 4.4: Mode shapes of the simulation model.

The modal displacement can be calculated as

$$p_i(t) = \int_0^t r_i(t) h_i(t - \tau) d\tau \quad (4.16)$$

in which

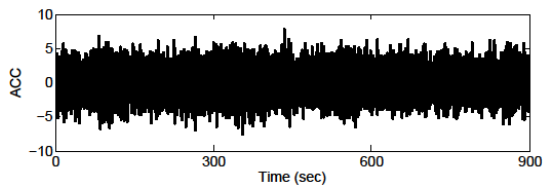
$$h_i(\tau) = \frac{1}{\omega_{D_i}} e^{-\zeta_i \omega_i \tau} \sin(\omega_i \tau) \quad (4.17)$$

where  $h_i(\tau)$  is the impulse response function for the displacement.

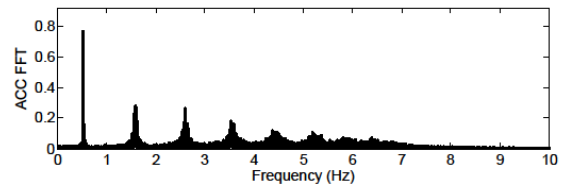
The numerical integration was used to calculate the dynamic response of the simulation model. Three excitation cases were simulated to investigate the effects of excitation types: Gaussian random, uniform random and impulse excitation cases. First,

$F(t)$  was chosen to be the  $(10 \times N)$  matrix that consists of ten Gaussian random sequences with the unit variance of  $\sigma^2 = 1 \text{ N}^2$ , which are mutually independent between the sequences. The second,  $F(t)$  was chosen to be the  $(10 \times N)$  matrix that consists of ten uniform random sequences with the amplitude between  $-0.5 \text{ N}$  and  $0.5 \text{ N}$ , which are mutually independent each other. In the last case,  $F(t)$  was chosen to be the  $(10 \times N)$  matrix of impulse excitation with the peak amplitude of  $1 \text{ N}$ .

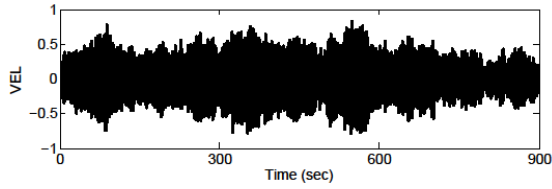
For the numerical simulation, first, the modal displacement,  $p_i(t)$ , was calculated for the sampling frequency of  $100 \text{ Hz}$  and the total duration of  $900 \text{ seconds}$ . The modal velocity,  $\dot{p}_i(t)$ , and the modal acceleration,  $\ddot{p}_i(t)$ , were also computed in the same way, using the first and second derivatives of the transfer function,  $h_i(\tau)$ . Then, the displacement,  $X(t)$ , velocity,  $\dot{X}(t)$ , and acceleration,  $\ddot{X}(t)$ , of each floor mass was found by multiplying the modal coordinates,  $p_i(t)$ ,  $\dot{p}_i(t)$ , and  $\ddot{p}_i(t)$ , by the mode shape vector,  $\phi$ . A sample result of the numerical simulation is shown in Figure 4.5. The test cases used in this simulation study are summarized in Table 4.2.



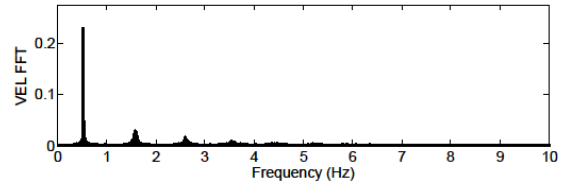
(a) Acceleration time history



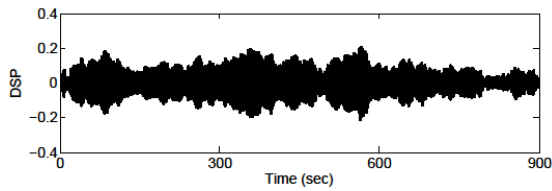
(b) Acceleration FFT



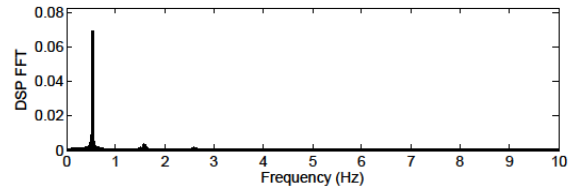
(c) Velocity time history



(d) Velocity FFT



(e) Displacement time history



(f) Displacement FFT

Figure 4.5: The dynamic response of the simulation model at the 10th floor.

Table 4.2: Control parameters evaluated in the simulation study.

Control parameters	Case no.	Description
Damping	Undamped	$\mathbf{C} = \mathbf{0}$
	Damped	$\mathbf{C} = 0.001\mathbf{K} + 0.001\mathbf{M}$
Excitation type	Gaussian	10 Gaussian random excitations with the unit variance of $\sigma^2 = 1 \text{ N}^2$ applied on all floors, which are statistically independent between the sequences
	Uniform	10 uniform random excitations with the amplitude between -0.5 N and 0.5 N applied on all floors, which are statistically independent between the sequences
	Impulse	10 impulse excitations applied on all floors with the peak amplitude of 1.0 N
Response type	ACC	Acceleration of the system response
	VEL	Velocity of the system response
	DSP	Displacement of the system response
Sensor spatial resolution	10	All ten sensors measuring at all floors
	5	Five sensors measuring at every other floors for the reduced spatial resolution

#### 4.5.2 Analysis Results of the Simulation Data

Once necessary system response datasets were obtained, they were analyzed using NExT-ERA, PCA and ICA methods. In the analysis, NExT-ERA require the user-defined parameters to be specified, including the system order and reference channels, while PCA and ICA do not need them. For NExT-ERA, the mode condensation algorithm developed by Pappa and Zimmerman [21] was used to evaluate the stabilization of the mode realization for the system orders from 10 to 30 which are equivalent to the maximum

number of modes from 5 to 15. All channels were used as reference positions, but not simultaneously. Ten valid modes were selected based on the modes with ten highest CMI values. All other modes having the CMI value less than 95% were excluded. Sample analysis results are shown in Figure 4.6.

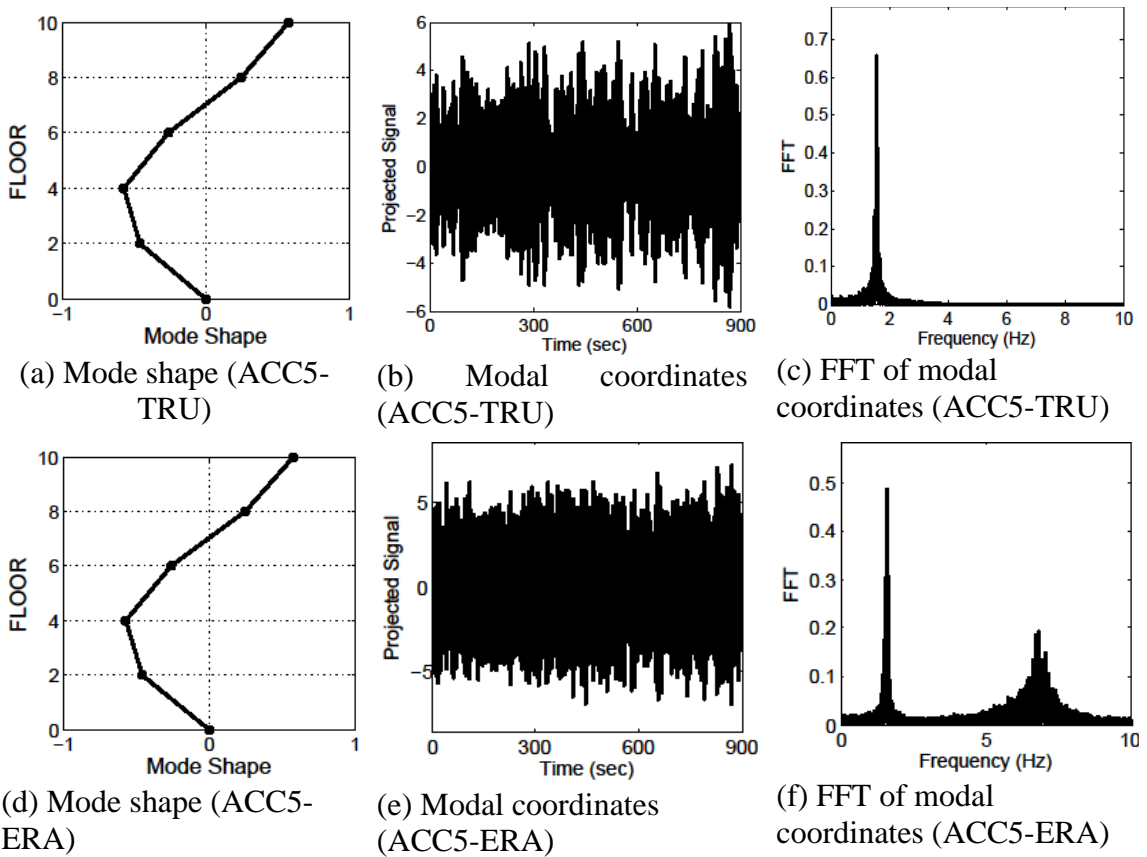


Figure 4.6: Mode shapes and modal coordinates of mode 2 for ACC5-TRU and ACC5-ERA.

### 4.5.3 Discussion on the Simulation Analysis Results

In this subsection, the effects of the test parameters listed in Table 4.2 on the analysis results will be discussed. For effective discussion, the following conventions will be used.  $\Psi$  and  $p$  indicate the mode shapes and the modal coordinates, respectively.  $\Psi^{\text{TRU}}$  and  $p^{\text{TRU}}$  indicate the true mode shapes and the modal coordinates determined by the modal superposition method in Equations 4.12 and 4.16.  $\hat{\Psi}$  and  $\hat{p}$  indicate the identified mode shapes and the modal coordinates. The superscript next to  $\hat{\Psi}$  and  $\hat{p}$  indicate the identification method, including ERA for the Eigensystem Realization Algorithm with the Natural Excitation Technique, PCA for the Principal Component Analysis, and ICA for the Independent Component Analysis. The subscript of  $\hat{\Psi}$  and  $\hat{p}$  indicate the response data types used in the identification, including the acceleration,  $\ddot{X}(t)$ , velocity,  $\dot{X}(t)$ , and displacement,  $X(t)$ . They are also summarized in the nomenclatures.

#### 4.5.3.1 Effects of the response types

In order to investigate the effects of the response types on the performance of the mode decomposition, three datasets were prepared for the system responses of the acceleration (ACC), velocity (VEL), and displacement (DSP) using the damped system under the Gaussian random excitation as described in Table 4.2. The full sensor spatial resolution (10 sensors) was used in the data preparation. The three datasets were processed using NExT-ERA, PCA and ICA methods. After the analyses, the mode shapes ( $\hat{\Psi}$ ) and the modal coordinates ( $\hat{p}$ ) were obtained using NExT-ERA, PCA and ICA for the three response types.

To measure the decomposition performance, the mode shapes and the modal coordinates were compared with  $\Psi^{\text{TRU}}$  and  $p^{\text{TRU}}$  using two indicators: the mode assurance criterion (MAC) for the mode shapes, and the correlation coefficients for the modal coordinates (COR). MAC can be calculated as

$$\text{MAC} = \frac{|\hat{\Psi}^* \Psi^{\text{TRU}}|^2}{(|\hat{\Psi}^* \hat{\Psi}|)(\Psi^{\text{TRU}*} \Psi^{\text{TRU}})} \times 100 \% \quad (4.18)$$

where \* represents transpose and conjugate;  $\hat{\Psi}$  is the identified mode shape vectors; and  $\Psi^{\text{TRU}}$  is the true mode shape vectors. Therefore, MAC can be a real number between 0 % and 100 %, indicating 100 % when the estimated mode shape vectors are identical to the true mode shape vectors. COR can be computed as

$$\text{COR} = \frac{(\sum_{k=1}^n \hat{p}_k p_k^{\text{TRU}})^2}{(\sum_{k=1}^n \hat{p}_k \hat{p}_k)(\sum_{k=1}^n p_k^{\text{TRU}} p_k^{\text{TRU}})} \times 100 \% \quad (4.19)$$

where  $\hat{p}_k$  is the identified modal coordinate vectors;  $p_k^{\text{TRU}}$  is the true modal coordinate vectors;  $n = 10$  for the full sensor spatial resolution, and  $n = 5$  for the reduced sensor spatial resolution. COR can also be a real number between 0 % and 100 %, indicating 100 % when the estimated modal coordinate vectors are identical to the true modal coordinate vectors.

The MAC and COR calculated for the first three modes are shown in Figure 4.7. The results of the three datasets are compared as ACC10-ERA (○), ACC10-PCA (□), and ACC10-ICA (×) in the figure, which are shown in the plot legend. In the plot, the x-axis shows MAC in percentage, and the y-axis shows COR in percentage. When the *full* sensor spatial resolution is used, for NExT-ERA (○) both MAC and COR were equal to one for

all modes and for all response types, which means that no errors were observed with NExT-ERA in both the mode shape and modal coordinate identification. For PCA ( $\square$ ), the results were the same as those for NExT-ERA, except  $\text{MAC} = 82\%$  in  $\hat{\Psi}_{\dot{x}}^{\text{PCA}}$  and  $\text{COR} = 82\%$  in  $\hat{p}_{\dot{x}}^{\text{PCA}}$  for mode 3 (Figure 4.7g). For ICA ( $\times$ ),  $\text{MAC}$  and  $\text{COR}$  were equal to one only for mode 1. Some errors were observed for other modes (Figures 4.7d to 4.7i). Therefore, the performance of the mode decomposition was observed the best with NExT-ERA, then with PCA, and the worst with ICA for these datasets.



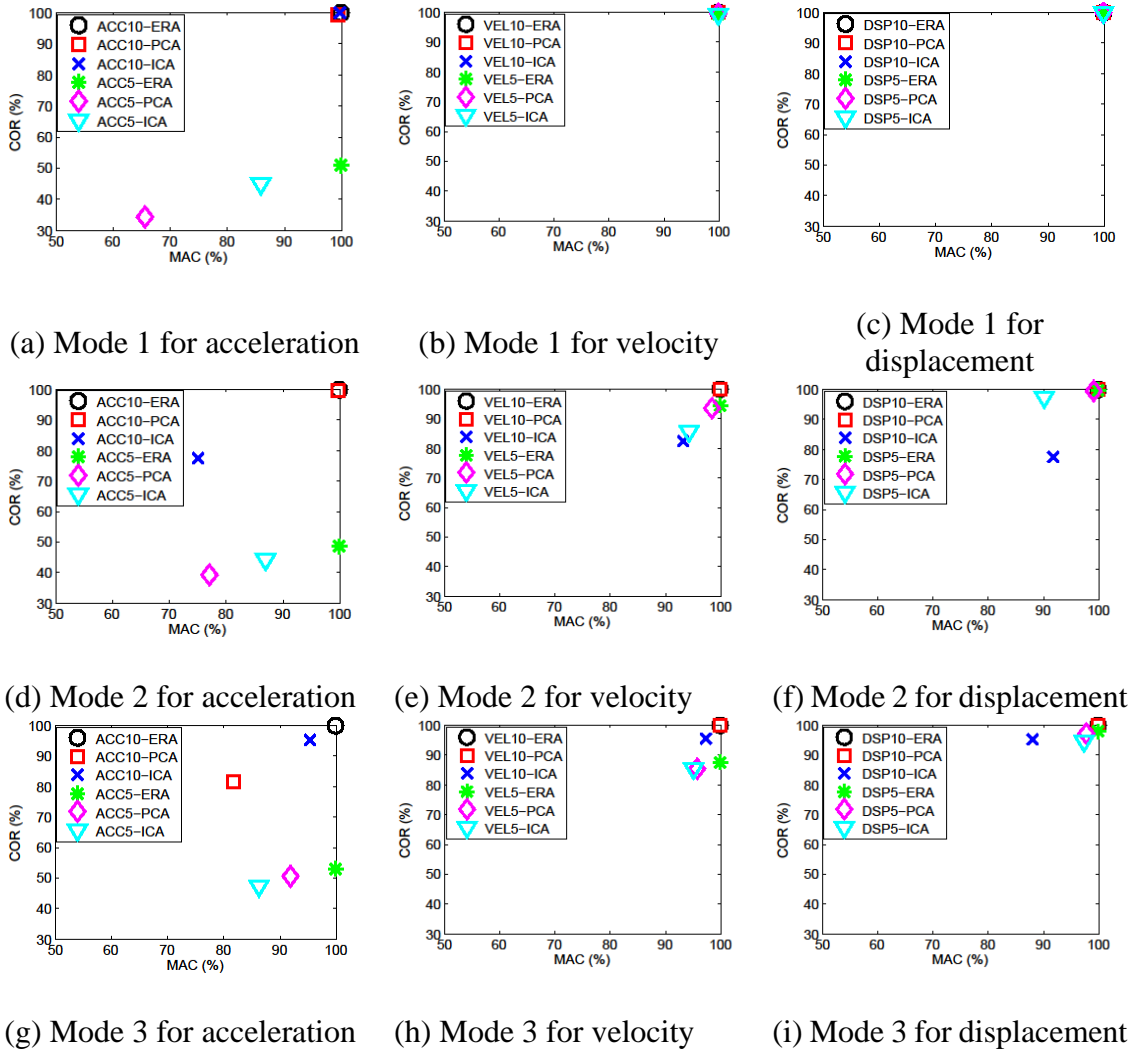


Figure 4.7: Comparison of MAC and COR between the identified and true mode shapes and modal coordinates of the first three modes.

The causes of the above mode decomposition errors for PCA and ICA were further investigated. Figure 4.8 shows the phase diagrams of the acceleration, velocity and displacement at Floors 1 and 2. The correlation coefficients ( $\rho$ ) of the Floor 1 and 2 system responses were measured  $\rho = 0.1\%$  for the acceleration,  $\rho = 50.2\%$  for the velocity, and  $\rho = 90.2\%$  for the displacement. The correlation coefficients show that the acceleration

sequences have almost no correlation, and the displacement sequences are highly correlated. The two mode components were also determined using NExT-ERA, PCA and ICA. The directions of the two components are shown as straight lines: the major mode direction is shown as 1 and the minor mode direction is shown as 2. The angles of the mode components were calculated, and the major component angle ( $\theta_1$ ) and the minor component angle ( $\theta_2$ ) are shown in the figure. The angle was measured in radian with respect to the horizontal line in the counter-clockwise direction.

The results show that the NExT-ERA mode components are identical to the true mode components. For PCA, the mode components for the velocity and displacement are identical to the true components in Figures 4.8e and 4.8f, while the identified modes for the acceleration has an error in Figure 4.8d. For ICA, errors are observed for all response types in Figures 4.8g to 4.8i. The above results agree with the results in Figure 4.7.

For the acceleration, the data are scattered in a circular boundary due to the low statistical correlation although the two floors are adjacent. For PCA, the low correlation of the acceleration data has the identification difficult since the PCA mode decomposition is based on the second-order statistics. The identification becomes more accurate for the velocity and displacement with the higher correlation coefficients. For ICA, the identification result using the acceleration has an error similar to the PCA result. However, the results using the velocity and displacement also have errors although the correlation coefficients are high. Further discussion will be made in the subsequent subsection to investigate the ICA identification.

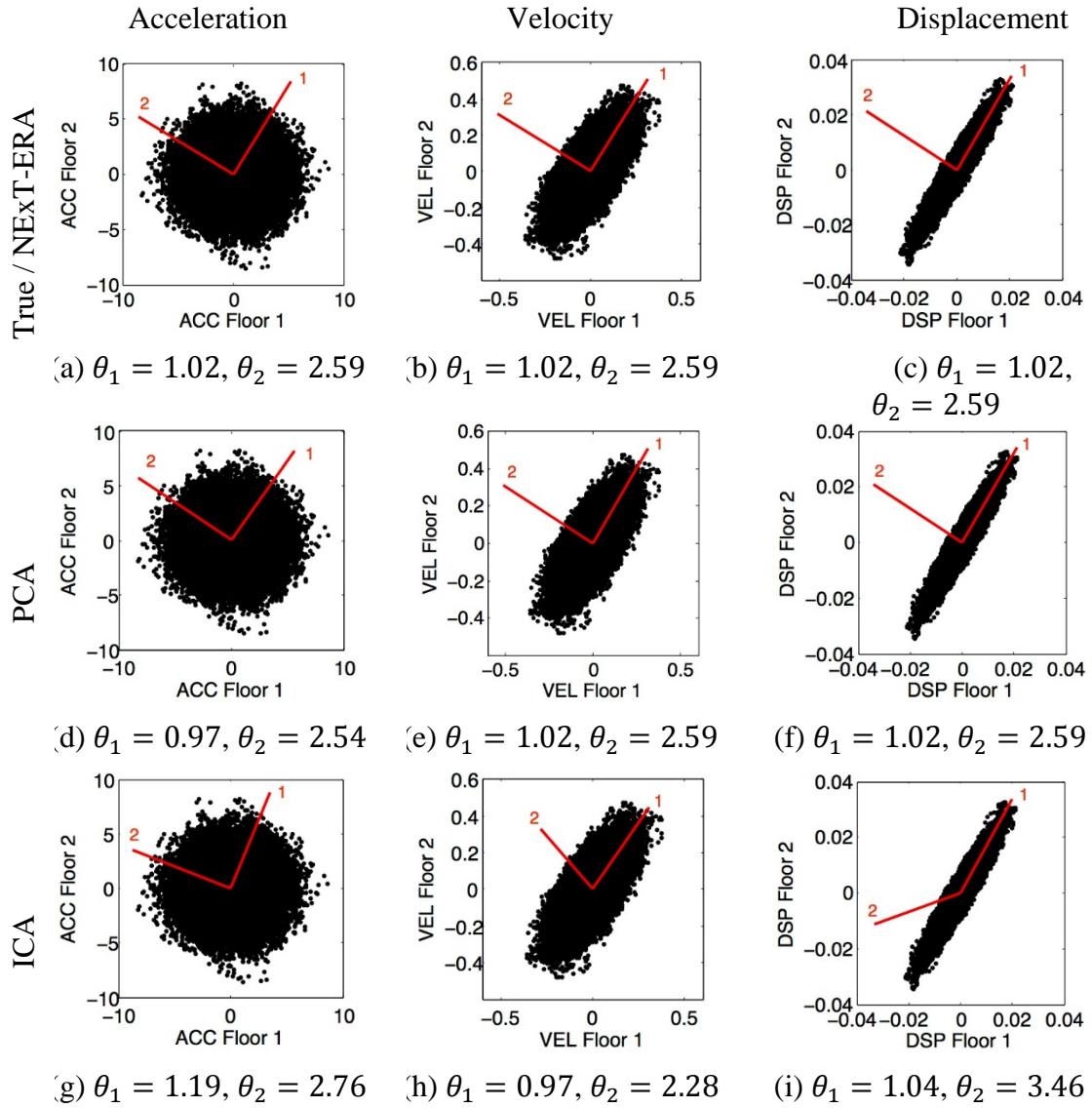


Figure 4.8: The mode components of the true, NEXt-ERA, PCA and ICA. The angles are shown in radian.

#### 4.5.3.2 Effects of the excitation types

In Section 4.5.3.1, it was observed that ICA had the lowest performance in the mode decomposition. The cause of the low performance is further investigated in this section. Figures 4.5.g to 4.5.i show the independent components identified using ICA method. The result in Figure 4.8.g shows that ICA has the same difficulty to determine the independent

components due to the statistically uncorrelated data that are scattered the circular boundary. As the result, the angles of the independent components are different from the true angles:  $\theta_1^{\text{ICA}} = 1.19$  rad, and  $\theta_2^{\text{ICA}} = 2.76$  rad. Unlike the PCA results in Figures 4.8e and 4.8f, however, for the velocity and displacement data, ICA determines the independent components, which are different from the true mode components:  $\theta_1^{\text{ICA}} = 0.97$  rad, and  $\theta_2^{\text{ICA}} = 2.28$  rad for the velocity in Figure 4.8h, and  $\theta_1^{\text{ICA}} = 1.04$  rad, and  $\theta_2^{\text{ICA}} = 3.46$  rad for the displacement in Figure 4.8i.

Hyvärinen and Oja (2000) stated that the fundamental restriction in ICA is that the independent components must be non-Gaussian since the distribution of any orthogonal transformation of the Gaussian variables  $(x_1, x_2)$  has the exactly the same distribution as  $(x_1, x_2)$ , in which  $x_1$  and  $x_2$  are statistically independent. When one of the independent components is non-Gaussian, the ICA model can still be estimated. Kerschen et al. [11] evaluated ICA for undamped vibrating structures with impulse and uniform random excitations. According to them, the application of ICA is limited to weakly damped system which typically has the damping ratios less than 1%. Another limitation stated by them is sensors should always be chosen in number greater or equal to the number of active modes. Poncelet et al. [13] also evaluated that the ICA model could be estimated for undamped vibrating structures using an impulse loading. They compared ICA with the Second-Order Based Identification (SOBI) and Stochastic Subspace Identification (SSI) methods using a 3-DOF system for different damping and noise levels. They showed that the accuracy of the mode shape identification decreased as the system damping or mode number increased. McNeil and Zimmerman [8] discussed about the damping effect on the kurtosis. They

deduced that undamped free-vibration modal responses closely corresponded to the independent components, while damped modal responses do not.

The effects of the excitation types on the ICA mode decomposition are discussed in this subsection, and the effects of the system damping are discussed in the subsequent subsection. For effective demonstration, the modal responses were simulated under the Gaussian random, uniform random and impulse excitations. Here, a simple 2-DOF oscillator is used for effective demonstration of the ICA's mode decomposition process. The one end of the oscillator was fixed, and the other was free. The same mass, stiffness, damping, which was used for the 10-DOF model in Section 4.5.1, were also used in this simulation. The excitation properties used in this simulation are described in Table 4.2. The two acceleration sequences of the 2-DOF system were obtained for the three excitations, and the joint probability density functions of the sequences are shown in Figure 4.9.

The kurtosis measures the sharpness or Gaussianity of the probability distribution. The random variable can be divided into sub-Gaussian, Gaussian and super-Gaussian. The sub-Gaussian random variable has lower peak than Gaussian having a negative kurtosis while the super-Gaussian variable has a higher peak having positive kurtosis [25]. The kurtoses of the acceleration data were measured as follows and are shown in Figure 4.9:

$$k(x) = \frac{E[x^4]}{(E[x^2])^2} - 3 \quad (4.20)$$

where  $E[x]$  is the expected value of the random variable,  $x$ ;  $k(x) = 3$  when  $x$  is the Laplace double exponential random variable;  $k(x) = 0$  when  $x$  is the Gaussian random variable; and  $k(x) = -1.2$  when  $x$  is the uniform random variable. Thus,  $k(x)$  is a positive value for the super-Gaussian random variable with a sharp peak, while  $k(x)$  is a negative value for the sub-Gaussian random variable with a flat peak.

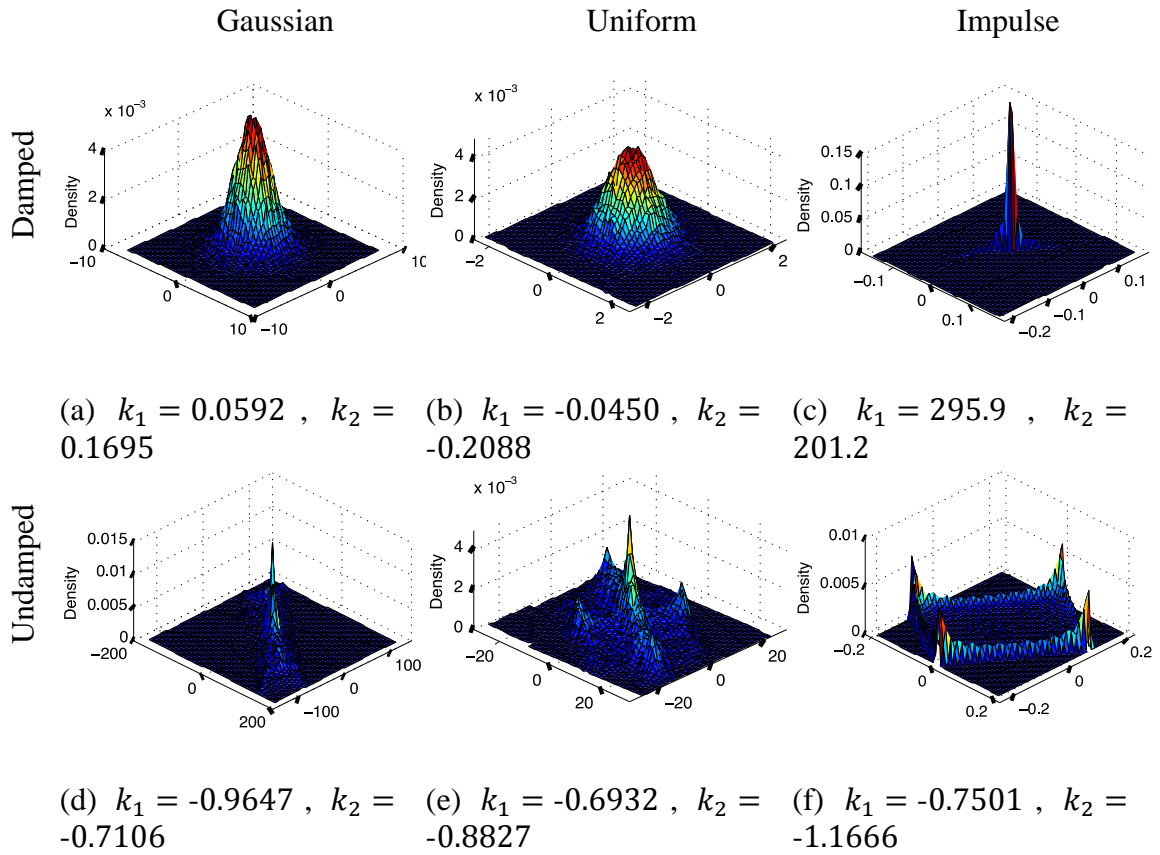


Figure 4.9: The joint probability density functions of the two acceleration sequences of the damped and undamped 2-DOF oscillator.

To investigate the effects of the excitation types, the independent components were determined and compared with the true modal components as shown in Figure 4.10. In the figure, the red lines indicate the independent components, and the green lines indicate the true modal components. The results showed that the independent components had no errors only when the undamped system was subjected to the impulse excitation.

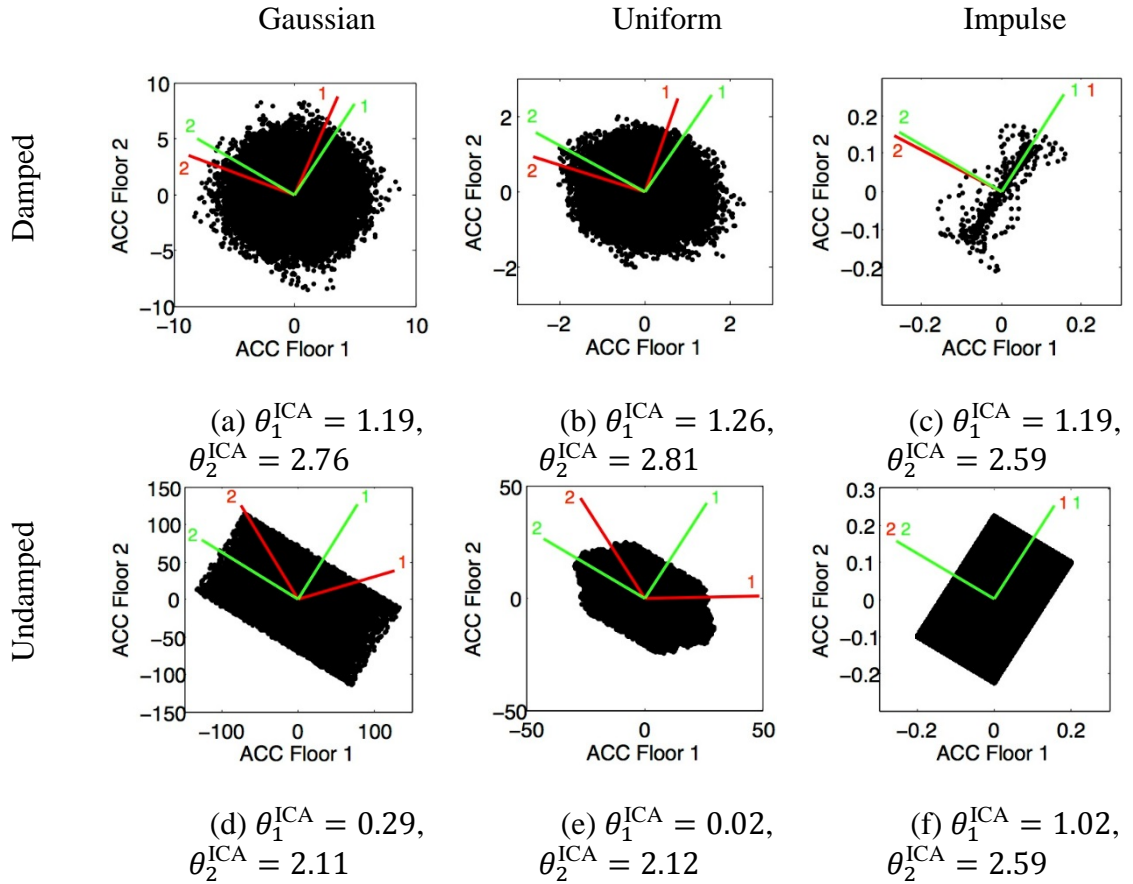


Figure 4.10: A comparison of true and ICA mode components for different excitation types using the acceleration data. The angles of the true modal components are  $\theta_1^{\text{TRU}} = 1.02$ , and  $\theta_2^{\text{TRU}} = 2.59$ .

#### 4.5.3.3 Effects of the system damping

The effects of the system damping on ICA were also investigated. Table 4.3 shows the averaged MAC and COR for the first three modes of the acceleration data of the damped and undamped 10-DOF systems in Table 4.2. Similar to the results of the 2-DOF systems in Figure 4.10, no errors were found with the undamped system under the impulse excitation, having both averaged MAC and COR equal to 100 %. The results also showed that both the system damping and the Gaussianity of the acceleration data caused errors in the ICA decomposition of  $\hat{\Psi}_{\ddot{x}}^{\text{ICA}}$  and  $\hat{p}_{\ddot{x}}^{\text{ICA}}$ .



Table 4.3: Averaged MAC and COR for the first three modes of the acceleration data.

	Gaussian		Uniform		Impulse	
	Damped	Undamped	Damped	Undamped	Damped	Undamped
Avg. MAC (%)	90	35	57	67	92	100
Avg. COR (%)	90	42	59	83	88	100

#### 4.5.3.4 Effects of the sensor spatial resolution

To investigate the effects of the sensor spatial resolution, three datasets were prepared for ACC, VEL and DSP using the same system (damped) and the same excitation type (Gaussian) in Section 4.5.3.1, but the reduced sensor spatial resolution (5 sensors). Then the datasets were processed using NExT-ERA, PCA and ICA methods to obtain the mode shapes ( $\hat{\Psi}$ ) and the modal coordinates ( $\hat{p}$ ). The MAC and COR were calculated for  $\hat{\Psi}$  and  $\hat{p}$ , respectively. The three datasets are shown as ACC5-ERA (\*), ACC5-PCA ( $\diamond$ ), and ACC5-ICA ( $\nabla$ ) in the legend. Unlike the full resolution datasets, when the *reduced* sensor spatial resolution was used, the all  $\hat{\Psi}$  and  $\hat{p}$  had identification errors, except the mode shapes using NExT-ERA of  $\hat{\Psi}_{\ddot{x}}^{ERA}$ ,  $\hat{\Psi}_{\dot{x}}^{ERA}$ , and  $\hat{\Psi}_x^{ERA}$ . This means that NExT-ERA was not affected with the reduced resolution in the mode shape identification of the first three modes for the acceleration, velocity and displacement data. For all methods, the accuracy of both  $\hat{\Psi}$  and  $\hat{p}$  was observed to be higher with the displacement data, and the accuracy was lowest with the acceleration data. In addition, both  $\hat{\Psi}$  and  $\hat{p}$  were less affected with a lower mode.

## **4.6 Field Study Using a Full-Scale Suspension Bridge**

### **4.6.1 Measurements of Bridge Responses in Ship-Bridge Collision Accident**

The Vincent Thomas Bridge (VTB) located in San Pedro, California in the U.S.A. was used in this experimental study (Figure 4.11). The bridge is an 1850-m long cable-suspension bridge with a main span length of 457 m, two-suspended side spans of 154 m each, and two 10-span cast-in-place concrete approaches of 545-m length on the both ends.

In 2006, the bridge was collided by a cargo ship that was passing underneath it. The freight-loading crane on the cargo ship struck the bridge main span from the side. About 30 minutes after the collision, the vehicular traffic on the bridge was stopped by the bridge authority to investigate potential damage. As the result, moderate damage was found on the bridge maintenance scaffold installed at the bridge main span. The investigation was continued for about two hours having no traffic on the bridge, and then the traffic was reopened. A detailed description of the ship-bridge collision accident can be found in Yun et al. [26].

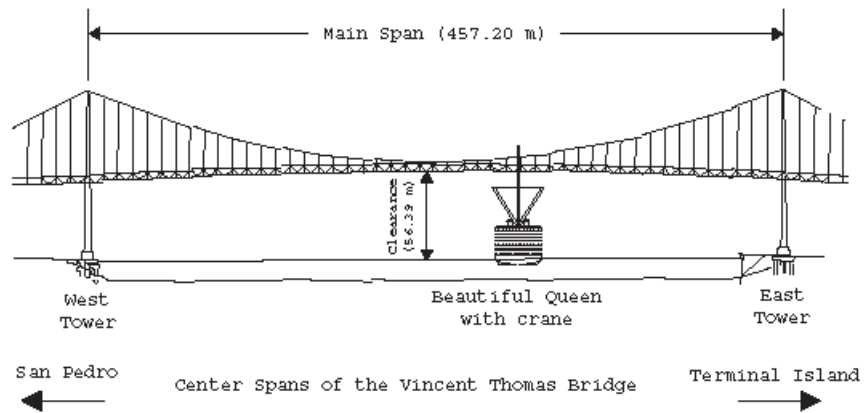


Figure 4.11: The ship-bridge collision by the onboard crane of the cargo ship [26].

Since a web-based continuous bridge monitoring system was installed on the bridge in 2005, the dynamic responses of the bridge were measured in the ship-bridge collision accident. The bridge responses were measured at the sampling rate of 100 Hz using the 26 force-balanced accelerometers installed on the bridge deck, piers and anchorage as shown in Figure 4.12. The accelerometers were connected to a data acquisition system with the 24-bit analog-digital converter via sensor wires. A detailed description of the data acquisition system and the web-based bridge monitoring system can be also found in Yun et al. [26].

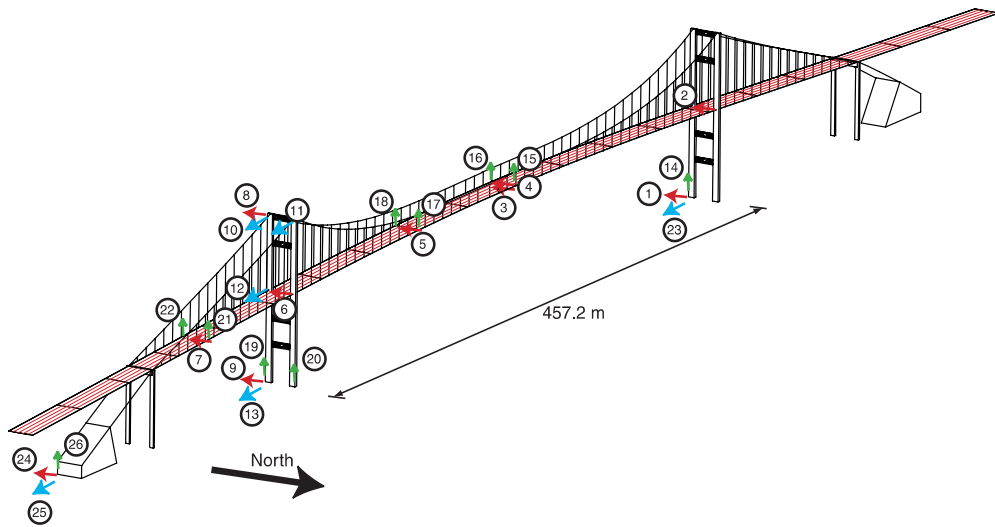


Figure 4.12: The sensor locations and directions on the bridge [26].

The acceleration data collected in the normal traffic condition, during the collision, and in the no-traffic condition were preprocessed to obtain the filtered acceleration, velocity and displacement data that are necessary for the modal decomposition analysis. For each excitation types, first the acceleration data were divided into 15-minute time histories. Then, the DC and linear trend were removed from the time histories. A 5% cosine-tapered window was applied before the high pass filter of 0.1 Hz with filter order of 2 and the low pass filter of 30 Hz with order of 4 were applied. Numerical integration was used to obtain the velocity. The same pre-process was applied before and after the numerical integration for the displacement. Channel 4 was excluded in the analysis due to the sensor malfunctioning. The above preprocessing procedures are shown in Figure 4.13. Sample bridge responses during the ship-bridge collision after the preprocessing are shown in Figure 4.14.

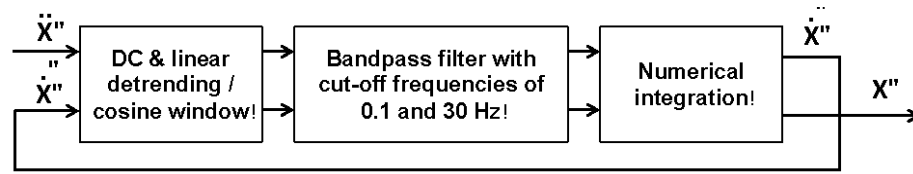
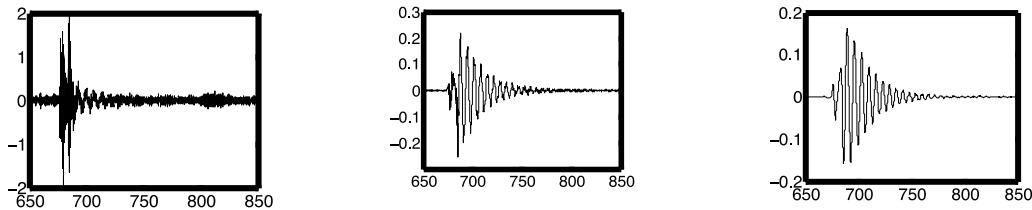


Figure 4.13: The preprocessing procedures to obtain the acceleration, velocity and displacement data of the bridge responses.



(a) Acceleration

(b) Velocity

(c) Displacement

Figure 4.14: Bridge responses during the ship-bridge collision after the preprocessing.

#### 4.6.2 Analysis Results of the Experimental Data

The bridge response data for the traffic, no-traffic and collision excitation cases were analyzed using NExT-ERA, PCA and ICA. Only twelve sensor channels on the bridge deck were used in these analyses. Channel 4 was excluded due to sensor malfunctioning. For NExT-ERA, all channels were used as reference channels but not simultaneously. The system order was set to be 100. The modes were condensed by choosing the ones with the CMI value higher than 70%. All fifteen modes were identified for each mode decomposition method. Among the fifteen modes, the first five modes were considered in the study. The modal frequencies and damping ratios identified with NExT-ERA are

summarized in Tables 4.4 and 4.5. The identified mode shapes, modal frequencies and damping ratios agreed with the modal parameters in previous studies ([26]; [27]; [28]).

Table 4.4: Identified modal frequencies (Hz) using NExT-ERA.

Mode	Traffic			No traffic			Collision		
	ACC	VEL	DSP	ACC	VEL	DSP	ACC	VEL	DSP
1	-	0.170	0.166	-	0.174	0.181	0.149	0.151	0.143
2	0.233	0.233	0.232	-	0.226	0.246	0.231	0.233	0.228
3	-	0.539	0.537	-	0.552	0.540	0.534	0.534	0.535
4	1.393	1.401	-	1.400	1.397	1.397	1.382	1.391	1.404
5	1.867	1.876	-	1.901	1.887	1.896	-	1.864	1.870

Table 4.5: Identified damping ratio (%) using NExT-ERA.

Mode	Traffic			No traffic			Collision		
	ACC	VEL	DSP	ACC	VEL	DSP	ACC	VEL	DSP
1	-	3.846	2.250	-	0.240	2.445	8.587	3.526	1.828
2	2.321	2.461	2.599	-	5.509	2.398	2.640	6.897	3.692
3	-	1.417	0.651	-	0.916	0.564	1.414	1.095	1.403
4	1.480	0.591	-	0.437	1.156	1.324	1.589	1.050	1.448
5	1.817	1.667	-	1.401	1.296	1.175	-	1.763	1.842

The mode shapes and modal coordinates were decomposed using NExT-ERA, PCA and ICA methods for the different response types and for the different excitation types. The sample mode shapes are shown in Figure 4.15, and the FFT of the sample modal coordinates are shown in Figure 4.16.

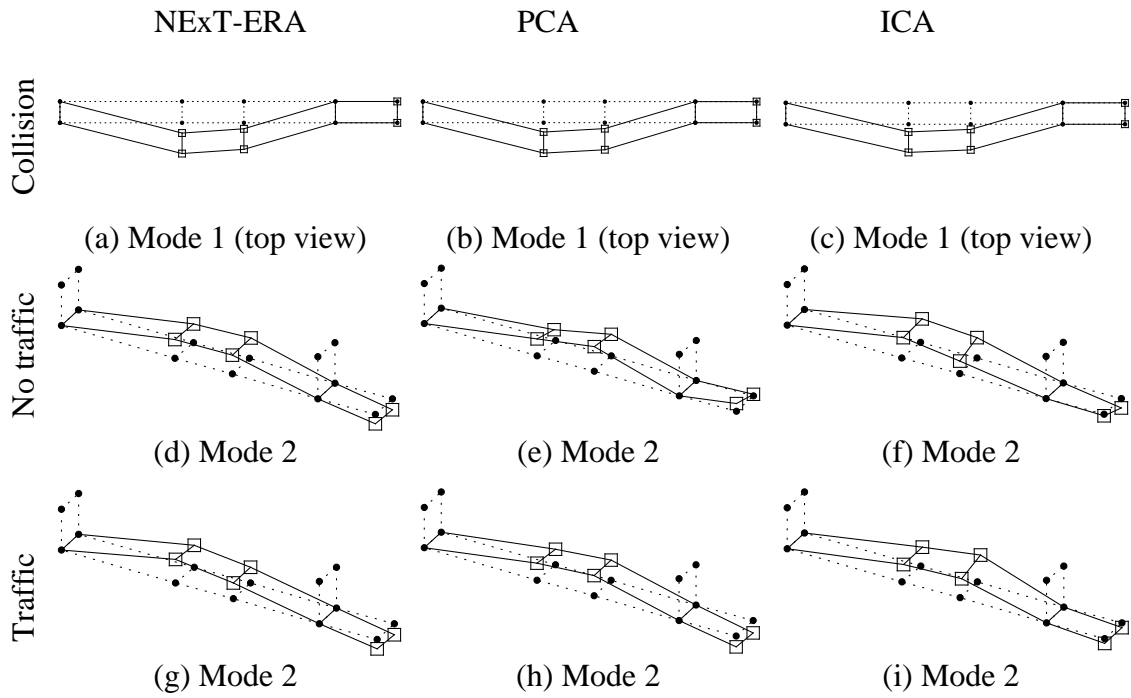


Figure 4.15: Mode shapes identified using NExT-ERA, PCA and ICA methods for the velocity data. The natural frequencies identified by NExT-ERA are 0.170 Hz for mode 1, 0.233 Hz for mode 2, and 0.539 for mode 3.

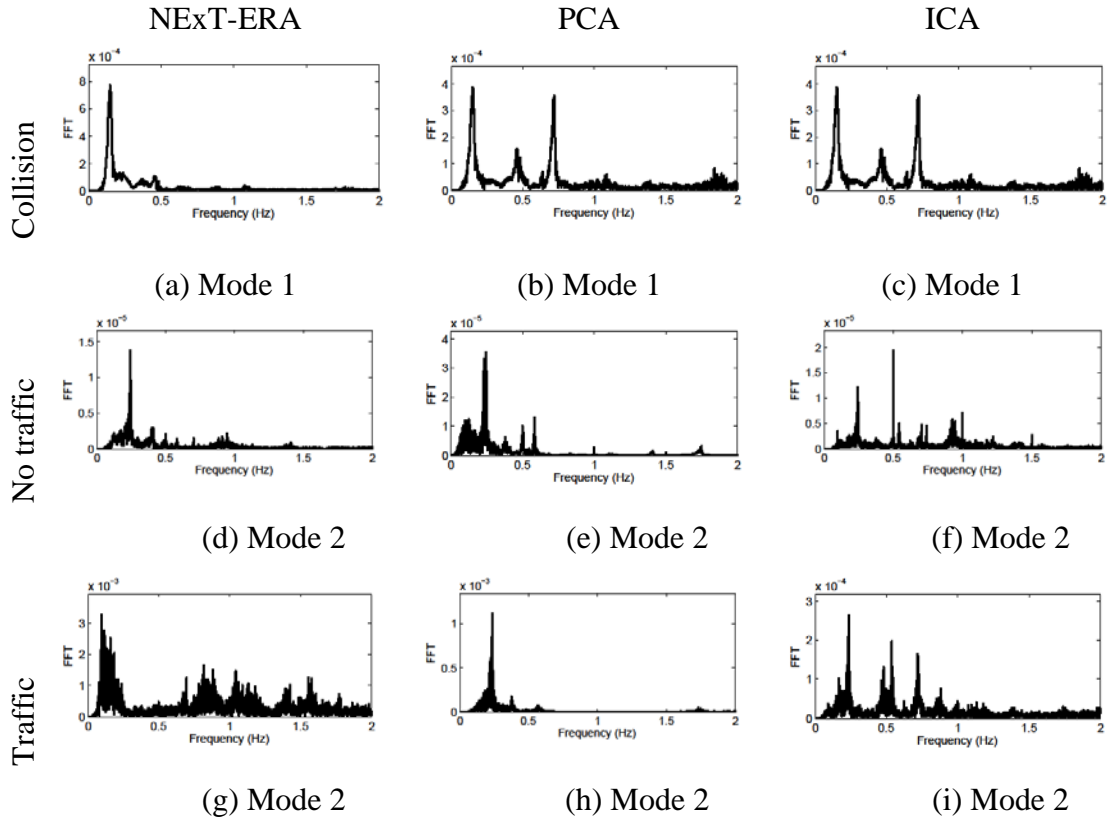


Figure 4.16: Modal coordinates identified using NExT-ERA, PCA and ICA methods for the velocity data. The natural frequencies identified by NExT-ERA are 0.170 Hz for mode 1, 0.233 Hz for mode 2, and 0.539 for mode 3.

#### 4.6.3 Discussion on the Experiment Analysis Results

As shown in Figure 4.7, the simulation study demonstrated that the mode decomposition results by NExT-ERA were closest to the true modes. The NExT-ERA results shown in Tables 4.4 and 4.5 also agree to the modal parameters in previous studies. Thus, the performance of the mode decomposition by PCA and ICA was compared with the performance by NExT-ERA. The comparison was made based on the mode shapes and modal coordinates similar to Equations 4.9 and 4.10 as



$$\text{MAC} = \frac{|\hat{\Psi}^{\text{PCA/ICA}*} \hat{\Psi}^{\text{ERA}}|^2}{(\hat{\Psi}^{\text{PCA/ICA}*} \hat{\Psi}^{\text{ERA}})(\hat{\Psi}^{\text{ERA}*} \hat{\Psi}^{\text{ERA}})} \quad (4.21)$$

where \* represents transpose and conjugate;  $\hat{\Psi}^{\text{PCA/ICA}}$  is the mode shape vectors identified using PCA and ICA; and  $\hat{\Psi}^{\text{ERA}}$  is the mode shape vectors identified with NExT-ERA; and  $0 \% \leq \text{MAC} \leq 100 \%$ . COR was also computed as

$$\text{COR} = \frac{(\sum_{k=1}^n \hat{p}_k^{\text{PCA/ICA}} \hat{p}_k^{\text{ERA}})^2}{(\sum_{k=1}^n \hat{p}_k^{\text{PCA/ICA}} \hat{p}_k^{\text{PCA/ICA}})(\sum_{k=1}^n \hat{p}_k^{\text{ERA}} \hat{p}_k^{\text{ERA}})} \quad (4.22)$$

where  $\hat{p}_k^{\text{PCA/ICA}}$  is the modal coordinate vectors identified using PCA or ICA;  $n = 12$  for the acceleration sensors on the bridge deck; and  $0 \% \leq \text{COR} \leq 100 \%$ .

The calculated MAC and COR for the first five modes are shown in Figure 4.17. Since MAC and COR are equal to one when  $\hat{\Psi}^{\text{PCA/ICA}} = \hat{\Psi}^{\text{ERA}}$  and  $\hat{p}_k^{\text{PCA/ICA}} = \hat{p}_k^{\text{ERA}}$ , the discrepancy between  $\hat{\Psi}^{\text{PCA/ICA}}$  and  $\hat{\Psi}^{\text{ERA}}$  is smaller when the data point is closer to the upper right corner,  $(\text{MAC}, \text{COR}) = (100 \%, 100 \%)$ . The data points in Figure 4.14a are classified based on their excitation types, and the results are shown in Figures 4.17b to 4.17d for the traffic, no traffic and collision. The averaged distances of the PCA and ICA methods in Figure 4.17 are calculated, and the results are shown with their ranking in Table 4.6.

As shown in Figure 4.17a, the PCA results for the displacement data, DSP-PCA ( $\diamond$ ), were closest to the NExT-ERA results for all excitation types. DSP-PCA was also closest to the NExT-ERA for the traffic, no-traffic and collision excitation cases as shown in Figures 4.14b to 4.14d. The PCA results for the velocity data, VEL-PCA ( $\times$ ), and the ICA results for the velocity data, VEL-ICA (\*), were also close to the NExT-ERA results

for all excitation types. Similar to the simulation results in Figure 4.7, the PCA and ICA results for the acceleration data, ACC-PCA (○) and ACC-ICA (□), had large discrepancy with the NExT-ERA results.

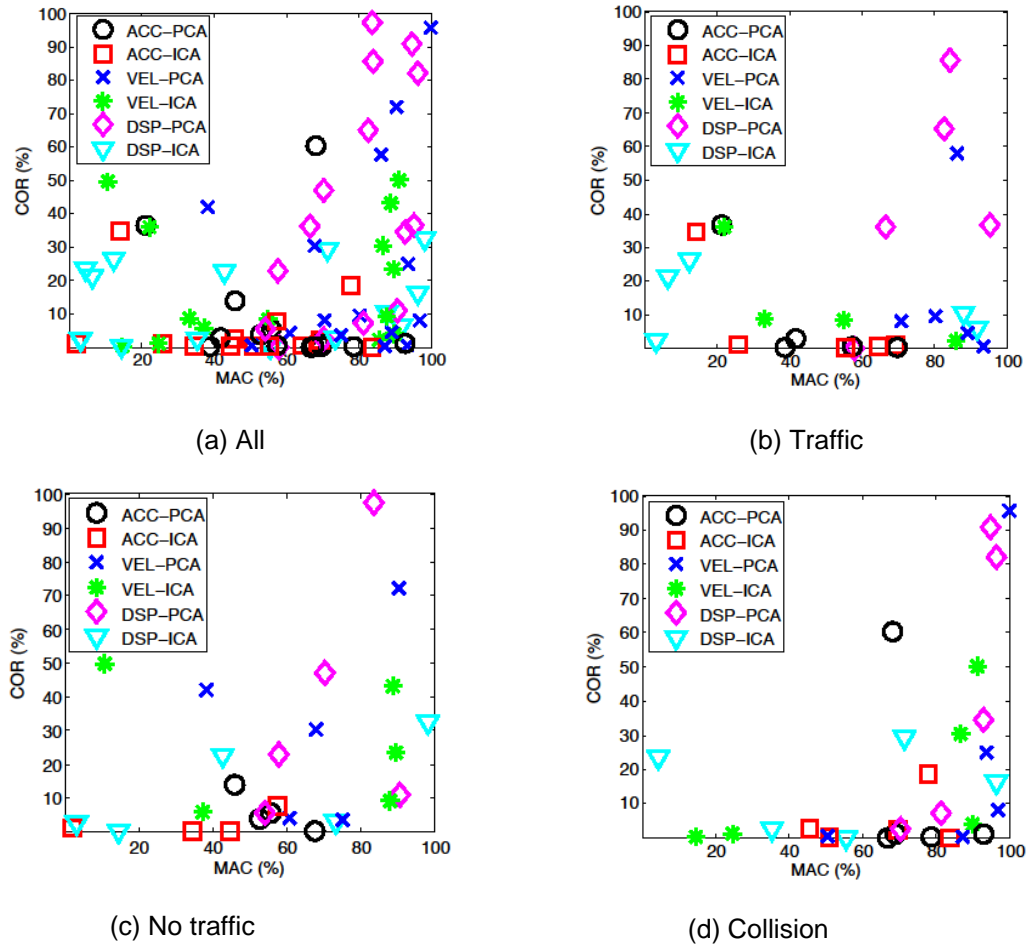


Figure 4.17: Comparison of MAC and COR between PCA and NExT-ERA, and between ICA and NExT-ERA for different response types.

Table 4.6: The averaged distances of the PCA and ICA methods and their ranking in Figure 4.14 for the first five modes.

All			Traffic			No traffic			Collision		
Rnk	Method	Dist.	Rnk	Method	Dist.	Rnk	Method	Dist.	Rnk	Method	Dist.
1	DSP-PCA	62.2	1	DSP-PCA	65.7	1	DSP-PCA	58.2	1	DSP-PCA	63.6
2	VEL-PCA	80.1	2	VEL-PCA	85.8	2	VEL-ICA	72.5	2	VEL-ICA	75.5
3	VEL-ICA	80.6	3	DSP-ICA	87.7	3	VEL-PCA	76.6	3	VEL-PCA	77.3
4	DSP-ICA	88.7	4	VEL-ICA	100.5	4	DSP-ICA	89.9	4	DSP-ICA	88.1
5	ACC-PCA	97.8	5	ACC-ICA	105.7	5	ACC-PCA	94.9	5	ACC-PCA	98.8
6	ACC-ICA	106.0	6	ACC-PCA	108.7	6	ACC-ICA	105.0	6	ACC-ICA	108.8

#### **4.7 Conclusions**

The PCA and ICA modes may be considered as an alternative to the modes identified with the modal analysis, such as NExT-ERA. However, the PCA and ICA modes have no theoretical foundation of the PCA and ICA modes since the modeling of these methods are data-driven, not based on physical assumptions. Therefore, a parametric study was conducted using the simulation and experimental data to relate the NExT-ERA, PCA and ICA modes for response types, excitation types, system damping, and sensor spatial resolution. Major findings from the parametric study include

- For the simulation results, the mode shapes and modal coordinates of NExT-ERA were closest to the true mode shapes and modal coordinates. The accuracy of the identified mode shapes was less sensitive to the sensor spatial resolution

than that of the modal coordinates. For the experimental results, the modal parameters identified with NExT-ERA agreed with those in previous studies.

- For the simulation results, a higher accuracy was found in the order of NExT-ERA > PCA > ICA, compared to the true mode shapes and modal coordinates. For the experimental results, the PCA results were closer to NExT-ERA than the ICA results.
- For PCA and ICA, the mode decomposition results are more accurate with the response types in the order of displacement > velocity > acceleration. The result is because the acceleration data is less correlated between channels than the displacement and velocity when the system is subjected to random or ambient excitation. The low correlation decreases the identification accuracy in the mode decomposition process.
- The ICA identification results had errors for the damped system. For Gaussian and uniform random excitations, the ICA results also had errors. The system damping increases the Gaussianity of the response data, which decreases the accuracy of the ICA identification [24]. The simulation results showed that the ICA identification had no error when the system is undamped, subjected to impulse excitation.
- For all methods, the lower modes are more accurate than the higher ones.

#### **4.8 Acknowledgements**

This study was supported in parts by grants from the U.S. National Science

Foundation (NSF), the Air Force Office of Scientific Research (AFOSR), and the National Aeronautics and Space Administration (NASA). The assistance of A. Shakal of the California Geology Service and L.-H. Sheng of the California Department of Transportation (Caltrans) is appreciated.

#### **4.9 References**

- [1] Mariani, R., & Dessi, D. (2012). Analysis of the global bending modes of a floating structure using the proper orthogonal decomposition. *Journal of Fluids and Structures*, 28, 115–134. doi:10.1016/j.jfluidstructs.2011.11.009
  
- [2] Feeny, B., & Kappagantu, R. (1998). On the physical interpretation of proper orthogonal modes in vibrations. *Journal of Sound and Vibration*. Retrieved from <http://www.sciencedirect.com/science/article/pii/S0022460X97913869>
  
- [3] Feeny, B. F., & Liang, Y. (2003). Interpreting proper orthogonal modes of randomly excited vibration systems. *Journal of Sound and Vibration*, 265(5), 953–966. doi:10.1016/S0022-460X(02)01265-8
  
- [4] Kerschen, G., Golinval, J., Vakakis, A. F., & Bergman, L. a. (2005). The Method of Proper Orthogonal Decomposition for Dynamical Characterization and Order Reduction of Mechanical Systems: An Overview. *Nonlinear Dynamics*, 41(1-3), 147–169. doi:10.1007/s11071-005-2803-2

- [5] Zhou, W., & Chelidze, D. (2007). Blind source separation based vibration mode identification. *Mechanical Systems and Signal Processing*, 21(8), 3072–3087. doi:10.1016/j.ymsp.2007.05.007
- [6] Smith, I. F., & Saitta, S. (2008). Improving Knowledge of Structural System Behavior through Multiple Models. *Journal of Structural Engineering*, 134(4), 553–561. doi:10.1061/(ASCE)0733-9445(2008)134:4(553)
- [7] Posenato, D., Lanata, F., Inaudi, D., & Smith, I. F. C. (2008). Model-free data interpretation for continuous monitoring of complex structures. *Advanced Engineering Informatics*, 22(1), 135–144. doi:10.1016/j.aei.2007.02.002
- [8] McNeill, S., & Zimmerman, D. (2010). Relating independent components to free-vibration modal responses. *Shock and Vibration*, 17, 161–170. doi:10.3233/SAV-2010-0504
- [9] Antoni, J., & Chauhan, S. (2013). A study and extension of second-order blind source separation to operational modal analysis. *Journal of Sound and Vibration*, 332(4), 1079–1106. doi:10.1016/j.jsv.2012.09.016
- [10] Roan, M. J., Erling, J. G., & Sibul, L. H. (2002). a New, Non-Linear, Adaptive, Blind Source Separation Approach To Gear Tooth Failure Detection and Analysis. *Mechanical Systems and Signal Processing*, 16(5), 719–740. doi:10.1006/mssp.2002.1504

- [11] Kerschen, G., Poncelet, F., & Golinval, J.-C. (2007). Physical interpretation of independent component analysis in structural dynamics. *Mechanical Systems and Signal Processing*, 21(4), 1561–1575. doi:10.1016/j.ymsp.2006.07.009
- [12] Poncelet, F., Kerschen, G., & Golinval, J. (2006). Experimental modal analysis using blind source separation techniques. *International Conference on ...*. Retrieved from <http://orbi.ulg.ac.be/handle/2268/18770>
- [13] Poncelet, F., Kerschen, G., Golinval, J.-C., & Verhelst, D. (2007). Output-only modal analysis using blind source separation techniques. *Mechanical Systems and Signal Processing*, 21(6), 2335–2358. doi:10.1016/j.ymsp.2006.12.005
- [14] Yang, Y., & Nagarajaiah, S. (2012). Time-frequency blind source separation using independent component analysis for output-only modal identification of highly damped structures. *Journal of Structural Engineering*, (October), 1780–1793. doi:10.1061/(ASCE)ST.1943-541X.0000621.
- [15] Yang, Y., & Nagarajaiah, S. (2013). Output-only modal identification with limited sensors using sparse component analysis. *Journal of Sound and Vibration*, 332(19), 4741–4765. doi:10.1016/j.jsv.2013.04.004
- [16] Yu, K., Yang, K., & Bai, Y. (2014). Estimation of modal parameters using the sparse component analysis based underdetermined blind source separation. *Mechanical Systems and Signal Processing*, 45(2), 302–316. doi:10.1016/j.ymsp.2013.11.018

- [17] Oh, C. K., Sohn, H., & Bae, I.-H. (2009). Statistical novelty detection within the Yeongjong suspension bridge under environmental and operational variations. *Smart Materials and Structures*, 18(12), 125022. doi:10.1088/0964-1726/18/12/125022
- [18] Kallinikidou, E., & Yun, H. (2013). Application of Orthogonal Decomposition Approaches to Long-Term Monitoring of Infrastructure Systems. *Journal of ...*, (June), 678–690. doi:10.1061/(ASCE)EM.1943-7889.0000331.
- [19] Yun, H.-B., Park, S.-H., Mehdawi, N., Mokhtari, S. Chopra, M., Reddi, L. N., and Park, K.-T. (in press). Monitoring for close proximity tunneling effects on an existing tunnel using principal component analysis technique with limited sensor data. *Tunnelling and Underground Space Technology*.
- [20] Juang, J. N., & Pappa, R. S. (1985). An eigensystem realization algorithm for modal parameter identification and model reduction. *Journal of Guidance Control and Dynamics*, 8(5), 620–627. Retrieved from <http://doi.aiaa.org/10.2514/3.20031>
- [21] James, G. H., Carne, T. G., & Lauffer, J. P. (1993). *The Natural Excitation Technique (NExT) for Modal Parameter Extraction From Operating Wind Turbines. System* (pp. 1–46). Sandia National Laboratories,. Retrieved from <http://vibration.shef.ac.uk/doc/1212.pdf>
- [22] Pappa, R. S., James, G. H., & Zimmerman, D. C. (1998). Autonomous modal identification of the space shuttle tail rudder. *Journal of Spacecraft and Rockets*, 35(2), 163–169. doi:doi.aiaa.org/10.2514/2.3324



- [23] Nayeri, R. D., Tasbihgoo, F., Wahbeh, M., Caffrey, J. P., Masri, S. F., Conte, J. P., & Elgamal, A. (2009). Study of time-domain techniques for modal parameter identification of a long suspension bridge with dense sensor arrays. *Journal of Engineering Mechanics*, 135(7), 669. doi:10.1061/(ASCE)0733-9399(2009)135:7(669)
- [24] Pappa, R. S., Elliott, K. B., & Schenk, A. (1992). A consistent-mode indicator for the eigensystem realization algorithm. *Journal of Guidance Control and Dynamics*, 16(5), 852–858. Retrieved from <http://hdl.handle.net/2060/19920015464>
- [25] Hyvärinen, a, & Oja, E. (2000). Independent component analysis: algorithms and applications. *Neural Networks : The Official Journal of the International Neural Network Society*, 13(4-5), 411–30. Retrieved from <http://www.ncbi.nlm.nih.gov/pubmed/10946390>
- [26] Yun, H., Nayeri, R., Tasbihgoo, F., Wahbeh, M., Caffrey, J., Wolfe, R., ... Sheng, L.-H. (2008). Monitoring the collision of a cargo ship with the Vincent Thomas Bridge. *Structural Control and Health Monitoring*, 15(2), 183–206. doi:10.1002/stc.213
- [27] Smyth AW, Pei J-S, M. S. (2003). System identification of the Vincent Thomas Suspension Bridge using earthquake records. *Earthquake Engineering and Structural Dynamics*, 32, 339–367.

- [28] Lus, H, Betti R, L. R. (1999). Identification of linear structural systems using earthquake-induced vibration data. *Earthquake Engineering and Structural Dynamics*, 28, 1449–1467.

## CHAPTER 5: CONCLUSIONS

The objectives of this study was to characterize the dynamic behavior of SFS structures and suspension bridge , Investigate foundation effect and structural damage on linear and non-linear identification results of building models, and compare the mode decomposition results of suspension bridge response using modal analysis and blind source separation methods. To do so a series of analysis was done.

Three identical frame models with fixed, pile and box foundations were tested on shake table with gradual increasing seismic amplitude. The structural damage was visually inspected during and after the test. Two types of methods were employed to characterize the dynamic behavior of the structures. The modal analysis methods of DSSI, SSI and NExT-ERA were used to identify the structures using the acceleration responses. The following results were observed from the modal analysis study:

- Modal analysis methods identified linearized version of the structure behavior.
- The discrepancy between the actual behavior and the linearized behavior of the structure increased with the structural damage. It was quantified in terms of the energy ratio, time lag and correlation coefficients.
- From the restoring forces phase diagrams it was shown that the identified linear stiffness is close to the linear stiffness of the measured phase diagram. The discrepancy increases at high displacement due to non-linearity effects. The identified linear stiffness also decreased with the increase of damage.
- The methods identified global change of behavior from damage. Natural frequencies decreased, and damping ratios increased.

- The foundations affected the seismic energies that is delivered to the super-structure which affected the severity of damage for different foundation types. The structure with fixed foundation had the highest damage and the one of box foundation the least damage. This effect was obvious in the change of the modal parameters.

Being non-linear local method, the multi-degree of freedom restoring force was used catch the non-linear behavior. From the analysis, it was found that:

- The method was able to characterize the non-linear behavior of the structure.
- The identification was localized. Each restoring force was identified independently.
- Energy dissipation was used to quantify and localize the structural damage. It showed that fixed foundation model had the highest severely damage and box foundation model had the least affected. It showed also lower stories had the highest energy dissipation. These observations completely agree with visual inspection, which make it a powerful method to localize and quantify changes in the structure.

The dynamic behavior of the Vincent Thomas Bridge was characterized through the mode decomposition using NExT-ERA, PCA and ICA. The acceleration, velocity and displacement responses were used. By comparing PCA and ICA with NExT-ERA the following conclusions were observed:

- PCA identified highest accuracy mode shapes and modal coordinates using displacement and lowest using acceleration. The reason behind this is the effect of spatial resolution and the correlation of the response data. Simulation studies have been done to prove these two effects.

- ICA identified lower accuracy mode shapes and modal amplitudes than PCA. System damping and type of excitation are main factors that affect the accuracy of ICA. To show that, simulation studies for different excitation types and damping ratios were conducted. ICA was most accurate in the case of impulse excitation with undamped system.